New Telescope Design with Silicon Photomultipliers for Fluorescence Light Detection of Extensive Air Showers

Tim Niggemann

Masterarbeit in Physik

vorgelegt der

Fakultät für Mathematik, Informatik und Naturwissenschaften der
Rheinisch-Westfälischen Technischen Hochschule Aachen

im Januar 2012

angefertigt am

III. Physikalischen Institut A

Erstgutachter und Betreuer

Prof. Dr. Thomas Hebbeker
III. Physikalisches Institut A
RWTH Aachen University

Zweitgutachter

Prof. Dr. Martin Erdmann
III. Physikalisches Institut A
RWTH Aachen University

Contents

List of Figures

Chapter 1.

Outline

Today's astroparticle physics aims to precisely measure the flux of ultra high energy cosmic rays (UHECRs), which are energetic particles coming from outer space, constantly hitting the atmosphere of the Earth. Since the flux in the highest energy regime above $E > 10^{19}\,\mathrm{eV}$ is below 1 particle per square-kilometer and year, it requires the measuring instruments to have a big exposure.

The Pierre Auger Observatory is a large array consisting of over 1660 water Cherenkov stations instrumenting an area of approximately $3000\,\mathrm{km}^2$. Furthermore, the array is overlooked by five fluorescence detector buildings. This hybrid detection principle permits measurements of both the longitudinal as well as the lateral profile of an extensive air shower. Such showers are induced by a cosmic ray particle, for example a proton or iron nucleus. As the primary particle hits a molecule in the atmosphere of the Earth, the hadronic interaction causes the production of many secondary particles which in turn create more secondaries. This particle avalanche has three main components: a hadronic, a muonic and most important an electromagnetic. The electrons and positrons of the shower front are mainly responsible for the excitation of Nitrogen molecules of the air. As the molecules de-excite, a weak ultraviolet light signature is measurable. This light, in the range of 280 nm to 420 nm, can be recorded by the fluorescence detector of the Pierre Auger Observatory.

The design of such a fluorescence telescope follows the Schmidt-camera layout. Its focal plane is instrumented with 440 photomultiplier tubes (PMTs). The sensitivity is large enough to measure fluorescence signals of showers with a primary particle energy greater than $10^{17}\,\mathrm{eV}$. A big advantage of such a calorimetric measurement is the proportionality of the measured light to the primary particle energy. This enables the fluorescence detector to calibrate the energy scale of the surface detector.

The project *FAMOUS* and this thesis aim to show that silicon photonmultipliers (SiPMs) can be used to measure fluorescence light. *FAMOUS* is an acronym for "First Auger MPPC camera for the Observation of UHECR air Showers". MPPC itself stands for "Multi-Pixel Photon Counter" and is a silicon photomultiplier. SiPMs are a promising new technology for single photon detection. An SiPM is constructed of many Geiger-mode avalanche photo-diodes each giving a digital signal when a photon has been detected. However, the signal carries no information on the number of incoming photons because of the Geiger operation-mode. Thus, proportionality is restored by having several hundreds of them arranged in a matrix. A typical pitch of such a cell is $100\,\mu\mathrm{m}$. SiPMs have several advantages over conventional photomultiplier tubes.

Figure 1.0.1.: The logo of *FAMOUS*. Famous is an acronym for "First Auger Multi pixel photon counter camera for the Observation of Ultra-high-energy cosmic ray Showers".

They do not require a high-voltage, are very small and promise to have a high photon detection efficiency (PDE) also in the ultra-violet regime. Nowadays, SiPMs achieve a PDE of approximately 35 % which is already at the level of modern PMTs.

The intermediate goal of *FAMOUS* is the production of a small fluorescence telescope prototype which has a focal plane instrumented with SiPMs. The increased sensitivity of upcoming generations of SiPMs will be a big step forward in comprehending the physics of extensive air showers. The smaller package of SiPMs lets increase the granularity of the telescope while having the same or better sensitivity to the very weak fluorescence signal of the shower. The increased resolution to the shape of extensive air showers permits to analyse of the type of the primary particle. Furthermore, SiPMs might offer a dynamic range wide enough to extend the measurable energy range below 10^{17} eV.

This thesis presents the optical design of the *FAMOUS* telescope and of its optical components. The simulation frameworks *CONEX*, *Auger Offline* and *Geant4* will be used to build up a complete detector simulation. With the help of this simulation, it is possible to improve the design of each component and the telescope by means of the optimal detector response. The estimated detector response will show that this prototype already has a promising performance.

Chapter 2.

Detection of Cosmic Rays

In the early 19th century it was believed that the ionisation of air, which caused a fully isolated electroscope to lose its charge, originated in the radiation of radioactive material in the Earth [1]. In 1912, Victor Hess used electrometers to measure the ionisation rate up to 5 km above ground and found a component within this radiation which becomes stronger with increasing altitudes. Two years later, Werner Kohlhörster could confirm this component to be extraterrestrial by measuring up to altitudes of 9 km.

Further investigations by Georg Pfotzer with a coincidence of three Geiger counters, revealed a maximum in this radiation at 15 km above ground. He drew the conclusion that the radiation must be secondary and created by interactions of particles with the atmosphere of the Earth. At the same time, working groups of Werner Kohlhörster and Pierre Auger measured significant spatial coincidence rates of two Geiger-Müller counters for big horizontal distances of several 10 m. Thus, these secondary particles had to be caused by the same event and move as an avalanche through the atmosphere. Because of the measured extent of the coincident signals, Pierre Auger assumed the primary particles must have energies above 1 PeV. This was the birth of modern, ground based extensive air shower experiments.

2.1. Cosmic Rays

Since then, the cosmic radiation has been measured over a vast energy range by various experiments utilising satellites, balloons or detectors on ground.

Cosmic rays can be measured over 30 orders of magnitude in energy [1]. Up to energies of 10^{15} eV, direct measurements have been performed and distinguished the individual constituents of the cosmic radiation. The relative abundances, normalised to Oxygen, for a primary particle energy of 10.6 GeV, are enlisted in table 2.1.1. They are akin to the composition of elements in our solar system.

2.1.1. Energy Spectrum

The all-particle energy spectrum follows a steep, power law

$$\frac{\mathrm{d}n}{\mathrm{d}E\,\mathrm{d}t\,\mathrm{d}\Omega\,\mathrm{d}A} \propto E^{-\gamma} \tag{2.1.1}$$

Element	Z	F	Element	Z	F
H	1	540	Al-Si	13-14	0.19
He	2	26	P-S	15-16	0.03
Li-B	3-5	0.40	Cl-Ar	17-18	0.01
C-O	6-8	2.20	K-Ca	19-20	0.02
F-Ne	9-10	0.30	Sc-Mn	21-25	0.05
Na-Mg	11-12	0.22	Fe-Ni	26-28	0.12

Table 2.1.1.: Relative abundances F of cosmic ray particles at $E = 10.6\,\mathrm{GeV}$ normalised to Oxygen [2, table 24.1].

with the energy E, the solid angle Ω and most importantly, the spectral index $\gamma \approx 2.7$ for $E \lesssim 4 \cdot 10^{15}\,\mathrm{eV}$. Both, data from direct measurements as well as indirect measurements, which record extensive air shower properties, are depicted in figure 2.1.1. The flux has been rescaled to $E^{-2.7}$ to reveal the peculiar features:

Knee At an energy of $E \approx 4{\cdot}10^{15}\,\mathrm{eV}$, the spectrum gets even steeper with a change in the spectral index from $\gamma = 2.7$ to $\gamma = 3.1$ [1]. Direct measurements of the cosmic rays revealed a large suppression in the flux of light elements of the cosmic radiation. The cut-off energy, at which the power law of the individual fluxes is broken off, is proportional to the nuclear charge Z and determined to $E_\mathrm{c}(Z) = Z \cdot E_\mathrm{c}^{(\mathrm{p})}$ with $E_\mathrm{c}^{(\mathrm{p})} = 4.5\,\mathrm{PeV}$ for protons. Currently, many possible explanations are discussed in the literature [1]. The two most popular correspond to an upper limit in the acceleration process of galactic supernovae and a leakage of cosmic rays from the galaxy due to a very weak galactic magnetic field ($B \approx 0.3\,\mathrm{nT}$) which is not able to bend these particles on a contained track.

2nd Knee Above $E \approx 4 \cdot 10^{17}\,\mathrm{eV}$, the spectrum gets slightly steeper. The end of the galactic component of the cosmic radiation has been assumed to be at $E \approx 30 \cdot E_\mathrm{c}^{(\mathrm{p})}$ since the abundance of ultra-heavy nuclei is very low in the GeV energy regime [1]. Nevertheless, the introduction of an ultra-heavy component might extend the galactic component up to $E \approx 92 \cdot E_\mathrm{c}^{(\mathrm{p})}$ [3]. This coincides with the occurrence of the second knee.

Ankle At $E \approx 4 \cdot 10^{18}\,\mathrm{eV}$ the spectrum flattens again to $\gamma = 2.6$ until it shows a strong depression at $E > 10^{20}\,\mathrm{eV}$ with at least 5σ significance [1]. Already in 1966, K. Greisen, G. Zatsepin and V. Kuzmin proposed a cut-off[1] at energies above $E = 6 \cdot 10^{19}\,\mathrm{eV}$ at which cosmic ray particles can interact with the photons of the cosmic microwave background [4]. Photons and protons combine to a Δ^+ resonance and finally decay into a pion and a proton or neutron. Nuclei get broken up due to photo-disintegration. In consequence, cosmic rays with energies above $10^{20}\,\mathrm{eV}$ must originate from within $100\,\mathrm{Mpc}^2$.

[1] Actually known als GZK-cut-off.
[2] The parsec is an astronomical unit of length whereas $1\,\mathrm{pc} = 3.26\,\mathrm{ly}$.

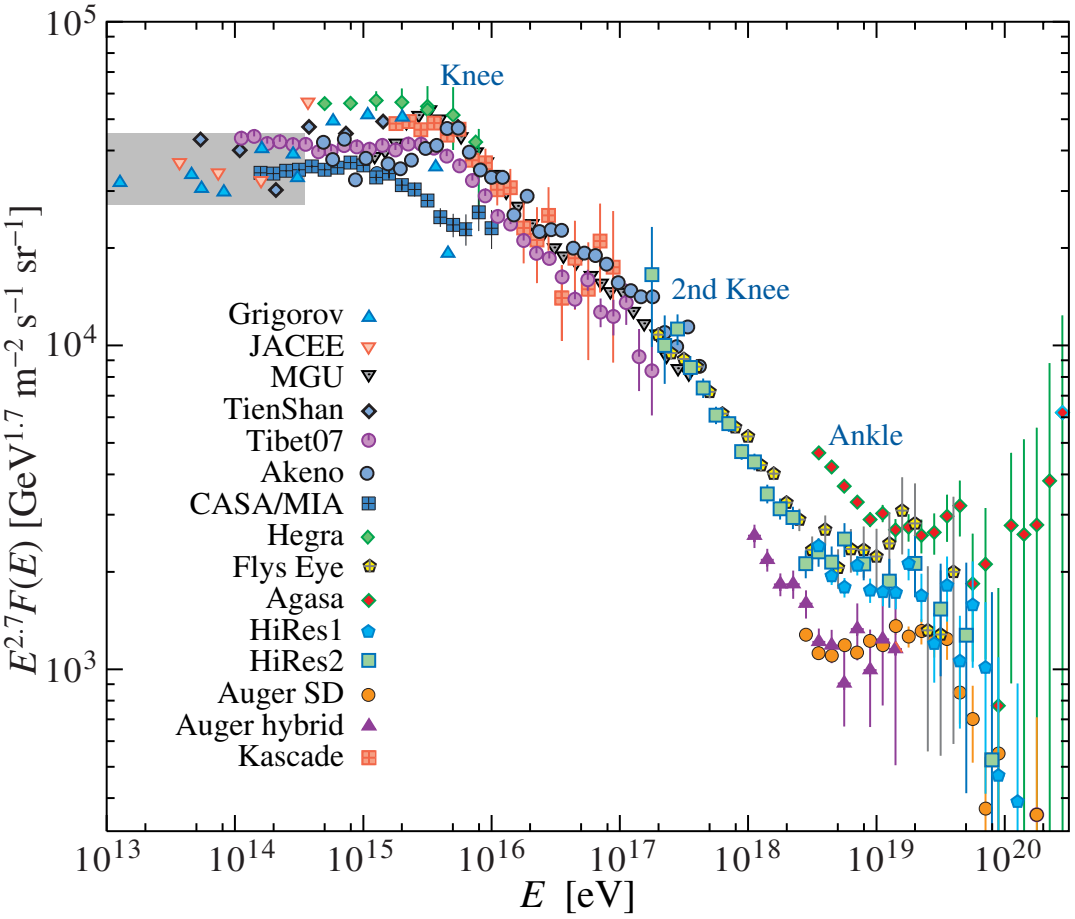

Figure 2.1.1.: Differential flux of cosmic rays from extensive air shower measurements as function of the energy of the primary particle. The data in the shaded area of the plot have been obtained by direct measurements. Taken from [2, Fig. 24.8].

2.1.2. Diffuse Shock Acceleration

The most demanding task of today's astroparticle physics is the ongoing search of possible accelerators which can be considered as the sources of the cosmic rays. In 1934, W. Baade and F. Zwicky calculated that a rate of approximately three supernovae per century and within our galaxy releases sufficient energy to sustain the flux of cosmic rays [6].

The remnants of supernovae propagate through space and shock fronts with turbulent magnetic fields are evolved. If a particle has enough energy to pass the shock front, it may be deflected by the surrounding magnetic field back into the shock region. It gains energy as it traverses and may be deflected back again [7]. Within each cycle of deflection, the energy growth is

$$\Delta E \propto \beta_s \tag{2.1.2}$$

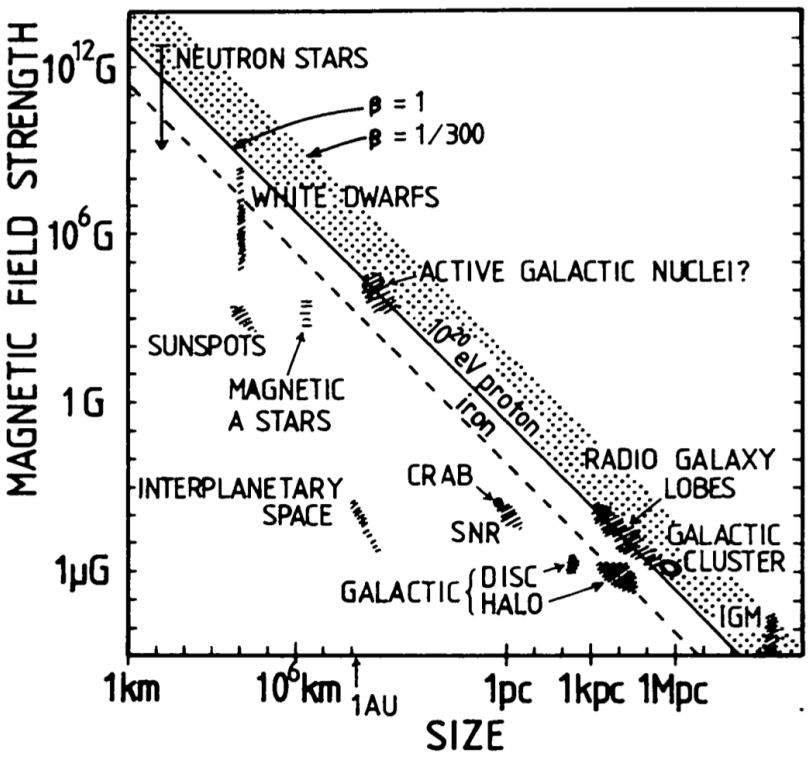

Figure 2.1.2.: Hillas-plot of astrophysical objects which could accelerate cosmic rays. The abscissa denotes the size of the source, the ordinate the strength of the magnetic field. The straight line represents 10^{20} eV protons, the dashed iron nuclei. Adapted from [5].

with the velocity of the shock front β_s. The maximum achievable energy is

$$E_\mathrm{max} \simeq Z\,\beta_\mathrm{s} \cdot 10^{19}\,\mathrm{eV} \left(\frac{R}{\mathrm{kpc}}\right) \left(\frac{B}{\mathrm{nT}}\right) \tag{2.1.3}$$

whereas Z is the particle charge, R the radius of the source region and B the magnetic field strength of the source [1]. This relation is plotted in figure 2.1.2. With this mechanism, some astrophysical objects come into consideration for the acceleration of cosmic rays to the highest observed energies. This mechanism is referred to as first-order Fermi acceleration since the energy gain is proportional to the shock front velocity β_s. E. Fermi also proposed a second-order process but it emerges to be too inefficient since it predicts acceleration time constants two orders of magnitude larger than the actual propagation time.

The first order Fermi acceleration is also successful because it generates a power law for the energy distribution with a spectral index of $\gamma = 2 + \epsilon$, $\epsilon < 1$. The aim of today's astroparticle physics is to find hints on the realised acceleration mechanisms in the composition and arrival directions of the ultra-high-energy cosmic rays.

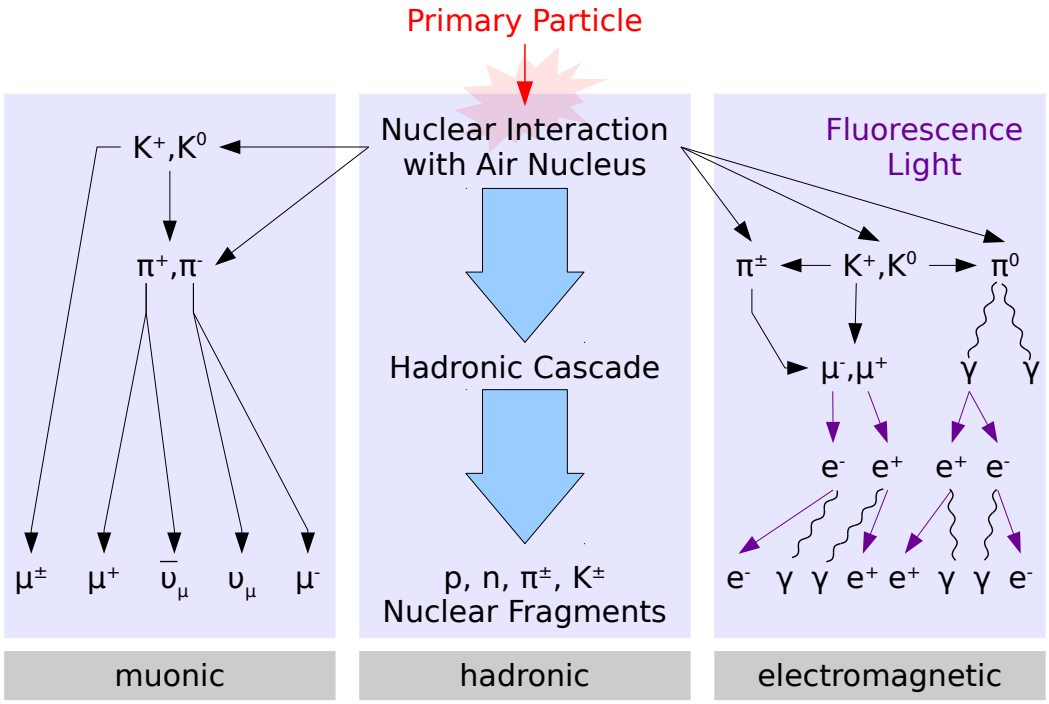

Figure 2.2.1.: Schematic of the components of an extensive air shower. After the first hadronic interaction, light mesons and hadrons form three different shower components: a muonic, hadronic and electro-magnetic.

2.2. Extensive Air Showers

As the cosmic ray particle penetrates the atmosphere of the Earth, it hits a nucleus of a molecule of the air. This first hadronic interaction creates numerous secondary charged and uncharged mesons ($\pi^{\pm}$, π^0, $K^{\pm}$, K^0, ...) and possibly other hadrons [1]. Approximately 50 % of the hadronic interactions are elastic [8]. Thus, a core of energetic hadrons evolves through the atmosphere whereupon the other half of the energy is used to create the secondary particles forming the muonic and the more dominant electro-magnetic component (see figure 2.2.1).

An important measure of extensive air shower physics is the slant depth X in units of $[X] = \mathrm{g\ cm^{-2}}$ which describes the amount of traversed matter. It can be expressed as a function of the altitude h:

$$X(h) = \int_h^\infty \rho(h')\mathrm{d}h' = \int_h^\infty \rho_0 e^{-h'/h_0}\mathrm{d}h' \approx 1000\mathrm{g\ cm^{-2}} e^{-h'/h_0} \tag{2.2.1}$$

with $h_0 \approx 7.25\,\mathrm{km}$ and the density $\rho_0 = 1.35\,\mathrm{kg\ m^{-3}}$. Inclined extensive air showers traverse more matter according to

$$X\,(h,\theta) = X\,(h)\,\frac{1}{\cos\theta} \tag{2.2.2}$$

where the zenith angle θ is the angle between the shower axis and the normal to the ground.

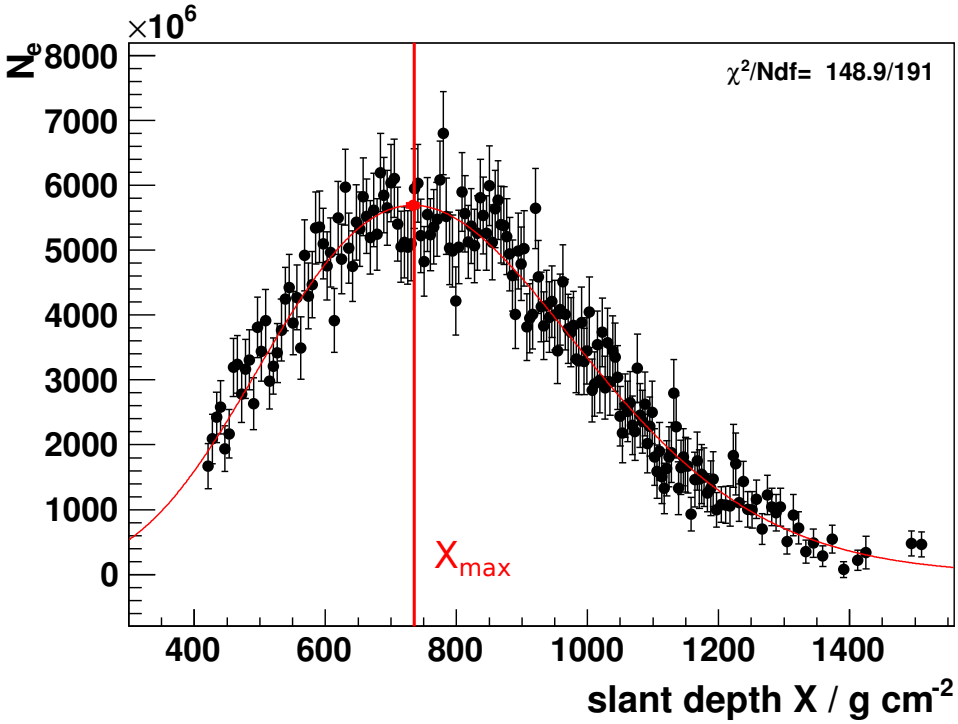

Figure 2.2.2.: Number of electrons and positrons N_e as function of the slant depth X. This event has been recorded by the fluorescence detector of the Pierre Auger Observatory at September 23, 2011 (event 12737439). The red line denotes the fitted Gaisser-Hillas-function.

The interactions of electrons, positrons and photons are dominated by bremsstrahlung and pair production. Furthermore, electrons and positrons are subject to ionisation and radiation losses

$$\frac{\mathrm{d}E}{\mathrm{d}X} = -\alpha\left(E\right) - \frac{E}{X_\mathrm{R}} \tag{2.2.3}$$

involving the Bethe-Bloch formula $\alpha\left(E\right)$ and the radiation loss described by the second term with the radiation length $X_\mathrm{R} \approx 37\,\mathrm{g\ cm^{-2}}$ in air [1]. As discussed later within this chapter, the deposited energy will be responsible for the creation of fluorescence light. The two components are equal for the critical energy E_c:

$$\alpha(E_\mathrm{c}) = \frac{E_\mathrm{c}}{X_\mathrm{R}} \quad . \tag{2.2.4}$$

A very simple but illustrative model is the Heitler model [1]. After traversing a mean interaction length of λ_int, in case of photons an electron-positron-pair respectively in case of electrons[3] a bremsstrahlung photon is created. The number of interactions for a slant depth of X is given by

$$n\left(X\right) = \frac{X}{\lambda_\mathrm{int}} \tag{2.2.5}$$

which corresponds to a number of particles of

$$N\left(X\right) = 2^{n(X)} = 2^{X/\lambda_\mathrm{int}} \quad . \tag{2.2.6}$$

[3] or positrons

The maximum number of particles is defined by the critical energy E_c

$$N_{\max} = \frac{E_0}{E_c} \tag{2.2.7}$$

with the initial energy E_0 of the primary particle. For energies below E_c, the ionisation process are more dominant and the air shower dies out. Thus, the depth of the shower maximum is

$$X_{max} = \lambda_{\text{int}} \log_2 \left(\frac{E_0}{E_c} \right) \quad . \tag{2.2.8}$$

A parametrisation of the longitudinal profile of the electro-magnetic shower component has been proposed by T. K. Gaisser and A. M. Hillas in 1977

$$N_e(x) = N_{\max} \left(\frac{X - X_1}{X_{\max} - X_1} \right)^{\frac{X_{\max} - X_1}{\lambda_{\text{int}}}} \exp \left(\frac{X_{\max} - X_1}{\lambda_{\text{int}}} \right) \tag{2.2.9}$$

with the depth of the first interaction X_1, the depth of the shower maximum $X_{\max}$, the maximum number of particles $N_{\max}$ and the mean interaction length λ_{int} for a proton or iron nucleus as primary particle in air of

$$\lambda_{\text{int,air}} \approx 80\,\text{g cm}^{-2}, \quad \lambda_{\text{int,Fe}} \approx 20\,\text{g cm}^{-2} \quad . \tag{2.2.10}$$

A fit of the Gaisser-Hillas function to a simple event recorded with the Pierre Auger Observatory is presented in figure 2.2.2. The simple Heitler model already demonstrates two important findings: the depth of the shower maximum increases logarithmically with the energy of the cosmic ray and the number of particles linearly.

2.3. Fluorescence Light Detection Technique

As the electrons of an extensive air shower pass through the atmosphere, each inelastic collision with a nitrogen molecule deposits energy according to the Bethe-Bloch formula [9]. A fraction of the collision energy gets absorbed by the nitrogen molecule which is exited from the ground state to upper levels.

A scheme of the transitions is presented in figure 2.3.1. In the ultraviolet wavelength regime, two systems contribute to the spectrum (compare figure 2.3.2): the $C^3\Pi_u \rightarrow B^3\Pi_g$ transition called $2P$ and the $B^2\sum_u^+ \rightarrow X^2\sum_g^+$ transition called $1N$. The figures 2.3.1 and 2.3.2 also denote the vibrational sub-levels $2P\,(\nu', \nu'')$ respectively $1N\,(\nu', \nu'')$. Additionally, the vibration levels are split into rotational levels which unfortunately are not yet resolved in measurements.

2.3.1. Fluorescence Yield

The number of emitted fluorescence photons N_γ^0 is proportional to the energy deposit $\mathrm{d}E_{\text{dep}}^{\text{tot}}$ per traversed matter $\mathrm{d}X$ [9]:

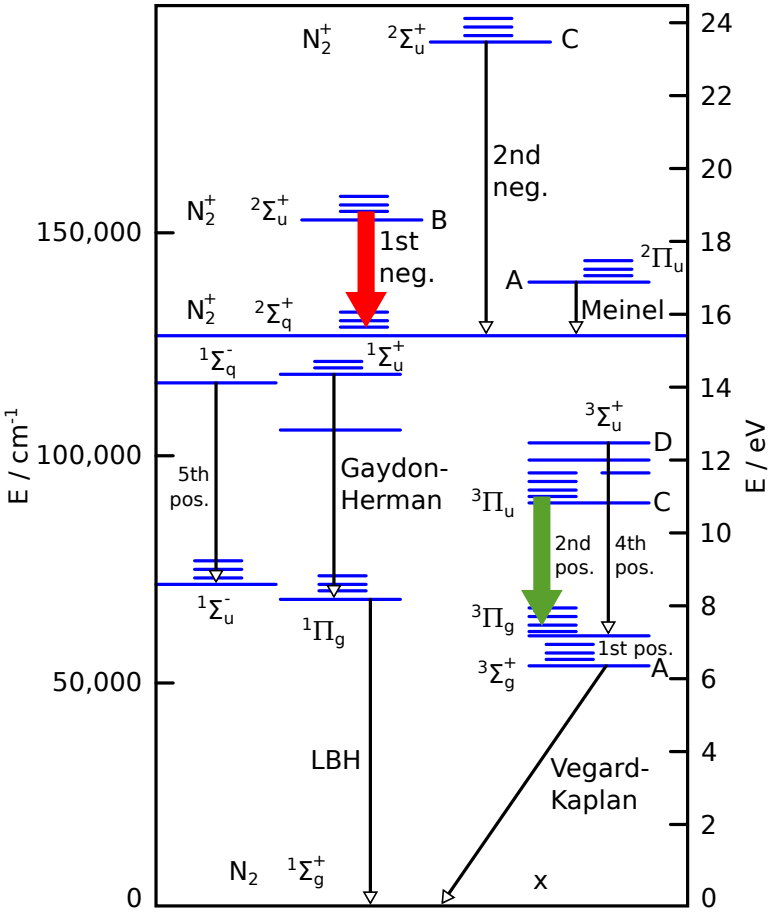

Figure 2.3.1.: Molecular levels of nitrogen (N_2 and N_2^+). The thick arrows mark the dominant transitions of the 2P ($C^3\Pi_u \rightarrow B^3\Pi_g$) and 1N ($B^2\sum_u^+ \rightarrow X^2\sum_g^+$) systems. Adapted from [9].

$$\frac{\mathrm{d}^2 N_\gamma^0}{\mathrm{d}X\mathrm{d}\lambda} = Y_\lambda(\lambda, P, T, u) \cdot \frac{\mathrm{d}E_{\mathrm{dep}}^{\mathrm{tot}}}{\mathrm{d}X} \quad . \tag{2.3.1}$$

The proportionality factor, in units of MeV^{-1}, is called fluorescence yield Y_λ. It depends on the wavelength λ, the atmospheric pressure P , the temperature T and the humidity u relying on the assumption that the fluorescence yield Y_λ is independent of the energy of the particle. Theoretical calculations, Monte Carlo methods as well as experimental data indicate the energy dependence is either negligible or not existent. Also often found in the literature is the fluorescence efficiency ϕ_λ defined as fraction of deposited energy transformed into fluorescence light. The ratio of ϕ_λ and Y_λ is given by the photon energy $E = h\nu$

$$Y_\lambda = \frac{\phi_\lambda}{h\nu} \quad . \tag{2.3.2}$$

Commonly, the transition of $2P(0,0)$ at $\lambda = 337\,\mathrm{nm}$ is chosen as reference point since it is most prominent in the spectrum. However, the experimental results on the absolute value of Y_λ seem contradictory because of the vast parameter space. The *AIRFLY*

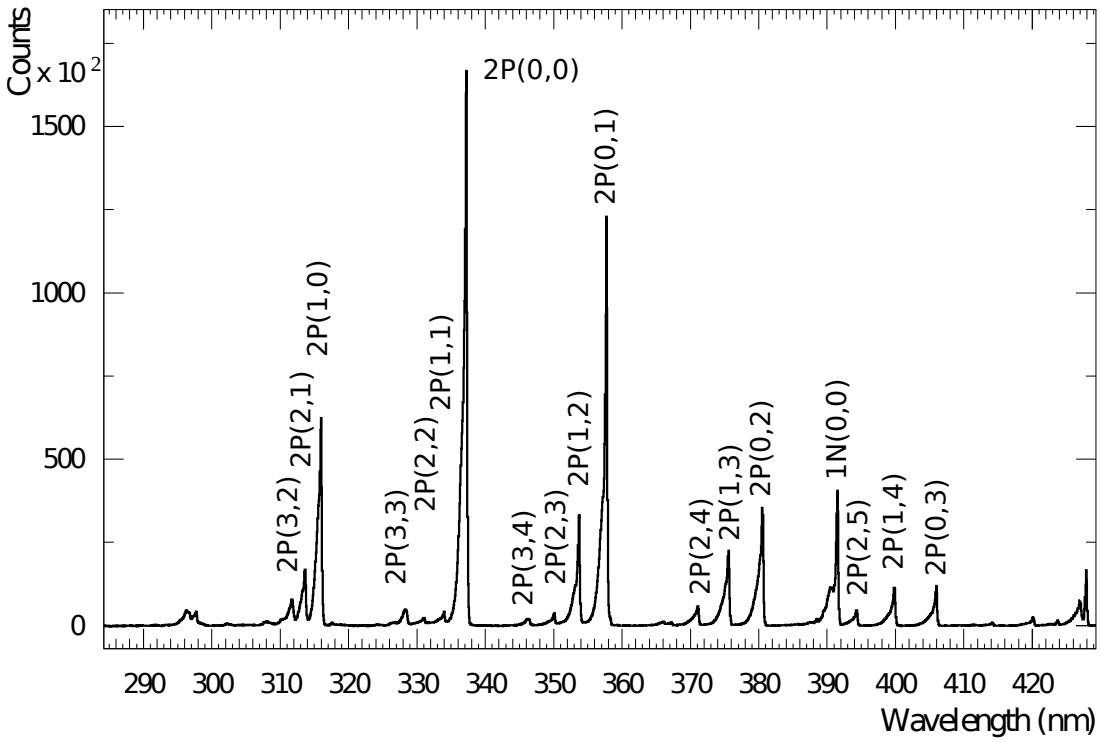

Figure 2.3.2.: Fluorescence light spectrum as function of the photon wavelength λ. The measurement has been performed by the *AIRFLY* experiment in dry air at 800 hPa and 293 K with a 3 MeV electron beam [10].

experiment measured in $P = 993\,\mathrm{hPa}$ and $T = 291\,\mathrm{K}$ dry air, which has been exited by $E = 350\,\mathrm{MeV}$ electrons, an absolute yield of

$$Y^{(\mathrm{abs})}_{337\,\mathrm{nm}} = 4.12\,\mathrm{MeV}^{-1} \quad . \tag{2.3.3}$$

In comparison, F. Kakimoto et al. [11] found for $E = 1.4\,\mathrm{MeV}$ electrons and a pressure of $P = 800\,\mathrm{hPa}$

$$\phi^{(\mathrm{abs})}_{337\,\mathrm{nm}} = 2.10 \cdot 10^{-5} \tag{2.3.4}$$

$$\Rightarrow Y^{(\mathrm{abs})}_{337\,\mathrm{nm}} = 5.71\,\mathrm{MeV}^{-1} \tag{2.3.5}$$

and M. Nagano et al. [12]

$$\phi^{(\mathrm{abs})}_{337\,\mathrm{nm}} = 2.34 \cdot 10^{-5} \tag{2.3.6}$$

$$\Rightarrow Y^{(\mathrm{abs})}_{337\,\mathrm{nm}} = 6.36\,\mathrm{MeV}^{-1} \quad . \tag{2.3.7}$$

A parametrisation of the fluorescence efficiency has been compiled by M. Nagano et al. [12] and expressed by means of photons per energy by F. Arqueros et al. [9] as

$$Y_\lambda = \frac{1}{(\mathrm{d}E/\mathrm{d}X)_{\mathrm{dep}}} \frac{\rho A_\lambda}{1 + \rho B_\lambda \sqrt{T}} \tag{2.3.8}$$

with the temperature T in Kelvin and the density of the gas ρ. The constants A_λ and B_λ have been measured by M. Nagano et al. for 10 different wavelengths between

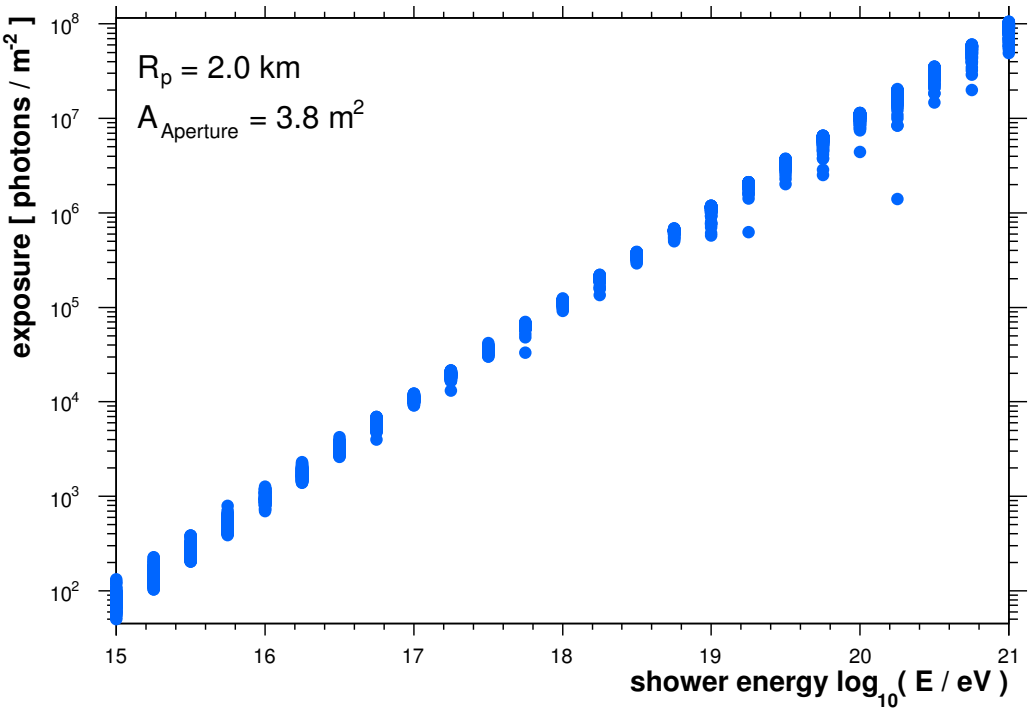

Figure 2.3.3.: Exposure to fluorescence light photons per square-meter on the aperture as function of the shower energy. The data have been obtained employing the *Offline* software package of the Pierre Auger Collaboration. The dots denote the light deposit of vertical extensive air showers with azimuth angles in a range of $\varphi = \pm 5\,^\circ$ with respect to the optical axis of the telescope. Furthermore, the simulated data are subject to shower-to-shower fluctuations.

300 nm and 400 nm [12]. The values for the reference wavelength $\lambda = 337\,\mathrm{nm}$ are

$$A_{337\,\mathrm{nm}} = (45.6 \pm 1.2)\,\mathrm{m^2 kg^{-1}} \tag{2.3.9}$$

$$B_{337\,\mathrm{nm}} = (2.56 \pm 0.10)\,\mathrm{m^3 kg^{-1} K^{-1/2}} \quad . \tag{2.3.10}$$

The results of the parametrisation are in good agreement with exact theoretical calculations at percent level [9].

In figure 2.3.3, the number of fluorescence photons, arriving a telescope with an aperture of $3.8\,\mathrm{m}^2$ in 2 km distance from vertical showers, is plotted as a function of the shower energy. For example, a $10^{18}\,\mathrm{eV}$ shower deposits approximately 10^5 photons m^{-2}. As expected from equations 2.2.7 and 2.3.1, the number of fluorescence photons increases linearly with the energy of the cosmic ray.

2.3.2. Event Reconstruction

A fluorescence light detector usually has a camera consisting of single pixels. As the shower passes through the field of view of the detector, the pixel i receives a signal at

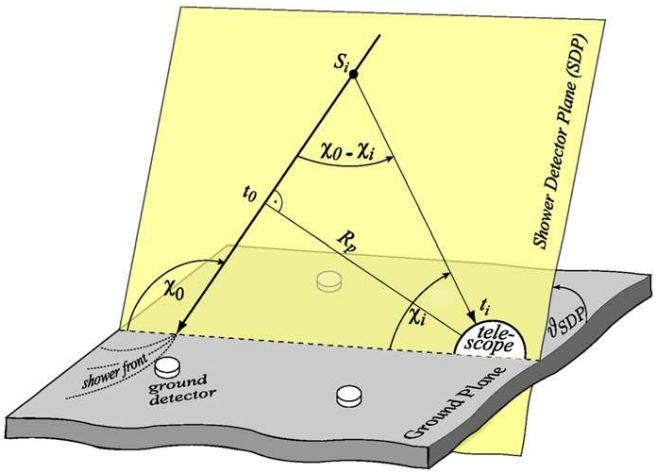

Figure 2.3.4.: Schematic of the shower-detector-plane used for the event reconstruction. At a time t_i the signal arrives at the camera pixel under an angle χ_i. The distance of the closest point of the shower axis to the telescope is defined as the shower-telescope-distance R_p and detected at t_0. Taken from [13].

the time t_i. As shown in figure 2.3.4, the shower axis and the pointing directions to the camera span the shower-detector-plane (SDP) [13]. The timing information t_i can be used to fit the shower axis

$$t(\chi) = t_0 + \frac{R_\mathrm{p}}{c} \tan\left[\left(\chi_0 + \chi\right)/2\right]$$

whereas c is the speed of light, χ the observation angle and χ_0 the angle between the shower-axis and the ground. The shower-telescope-distance R_p is defined as the distance to the closest point of the shower axis detected at t_0. An example obtained from a measurement of the Pierre Auger Observatory is presented in figure 2.3.5.

Once the geometry of the shower has been determined, the observation angle χ can be translated to the slant depth X and plotted against the number of electrons N_e. The number of electrons can be derived with the aid of the fluorescence yield Y_λ from the amount of collected light in a given pixel. Additionally, the attenuation and variable density of the atmosphere have to be considered which makes the calculation highly non-trivial. The fit of the Gaisser-Hillas-function (see equation 2.2.9) to the data reconstructs the shower maximum X_max and the energy E_0 of the primary particle.

This method is used for the analysis of the data recorded by the fluorescence detector of the Pierre Auger Observatory which will be introduced in the next section.

2.4. The Pierre Auger Observatory

The southern site of the Pierre Auger Observatory is a large area experiment covering over $3000\,\mathrm{km}^2$ of the Argentinian Pampa Amarilla, near Malargüe, province of Mendoza. A map of the area is shown in figure 2.4.1. After the invest of \$50 million construction budget, the observatory successfully measures extensive air showers since

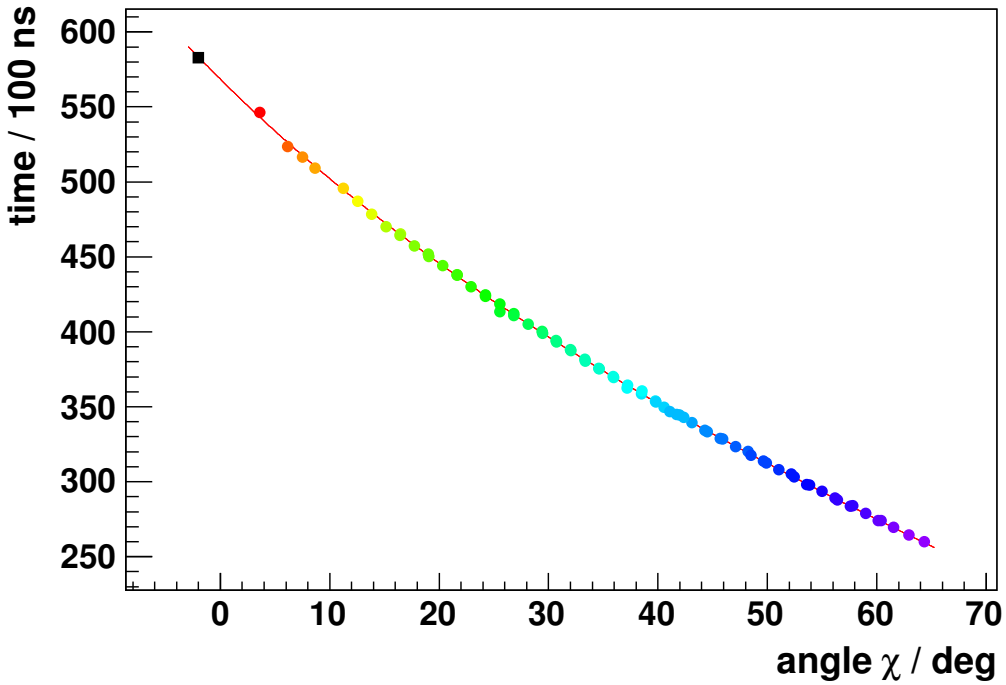

Figure 2.3.5.: Arrival time of the fluorescence light as a function of the observation angle χ for one event. The data are a measurement of the fluorescence detector of the Pierre Auger Observatory at September 23, 2011 (event 12737439). The square at $\chi = 0$ represents the surface detector timing information.

2004 in the highest energy regime exceeding 10^{18}eV. In early 2009 a low energy extension called *HEAT* ("High Elevation Auger Telescope") has been put into service which aims to extend the energy range down to 10^{17}eV. Furthermore, an important link to the results of the flux of cosmic rays of other ground based detectors, which measured in a lower energy regime, had been achieved [15].

2.4.1. The Hybrid Detection Principle

The key element of the success of the observatory is the hybrid detection principle (see figure 2.4.2). The surface detector records the secondary particles of the extensive air shower at ground level. In addition, the fluorescence detector measures the energy deposit by means of the fluorescence light detection technique as discussed in the previous section. Therefore, the complementary data make both, the precise measurement of the lateral and the longitudinal distribution of the extensive air shower possible.

2.4.2. The Surface Detector

The surface detector consists of over 1660 water Cherenkov stations arranged in a hexagonal grid with a spacing of 1.5 km [16]. The stations are manufactured of rotational molded high-density polyethylene. A liner of a highly reflective foil seals the

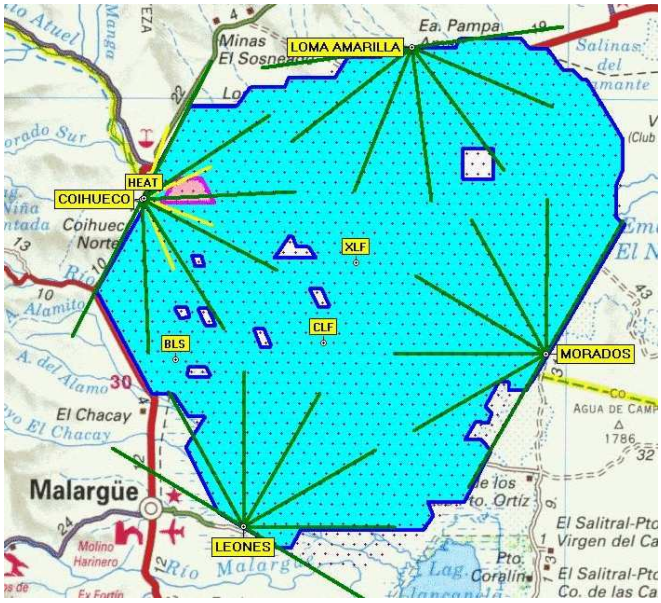

Figure 2.4.1.: Map of the southern site of the Pierre Auger Observatory. The blue area shows the surface detector with the fluorescence detector buildings marked in yellow at the borders. The blue dots are the positions of surface stations. The green lines visualize the viewing cones of the fluorescence telescopes [14].

over 12,000 l of water from chemical or biological contamination and external light. When an electron or muon of the shower front traverses the medium, Cherenkov light is emitted when its speed exceeds the speed of light in the medium. This light is measured with three photomultiplier tubes of 8" diameter situated at the top of the tank. Therefore, the surface detector measures the footprint of an extensive air shower at ground with a duty cycle of 100 %.

The second detector is the fluorescence detector.

2.4.3. The Fluorescence Detector

The fluorescence detector consists of 5 telescope buildings housing 27 telescopes in total [13]. Schematics of the telescope and a building are provided in figures 2.4.3 and 2.4.4. The optics follow the Schmidt camera design which will be described in detail in chapter 5. It has an aperture diameter of 2.2 m including a ring of tiles at the border mimicking the needed Schmidt-corrector plate. The incoming light additionally passes a filter made of M-UG6 filter glass which is only transparent to ultraviolet and partially to infrared light[4]. This filter is crucial for the reduction of the visible light portion in the telescope which is considered to be noise. Behind the aperture, a $3.8 \times 3.8\,\mathrm{m}^2$ large segmented mirror composed by 36 tiles collects the incoming light beam and reflects it onto a curved camera surface which sits between the aperture and the mirror in the

[4]The transmission as a function of the wavelength can be found in the appendix in figure A.0.6 on page 94.

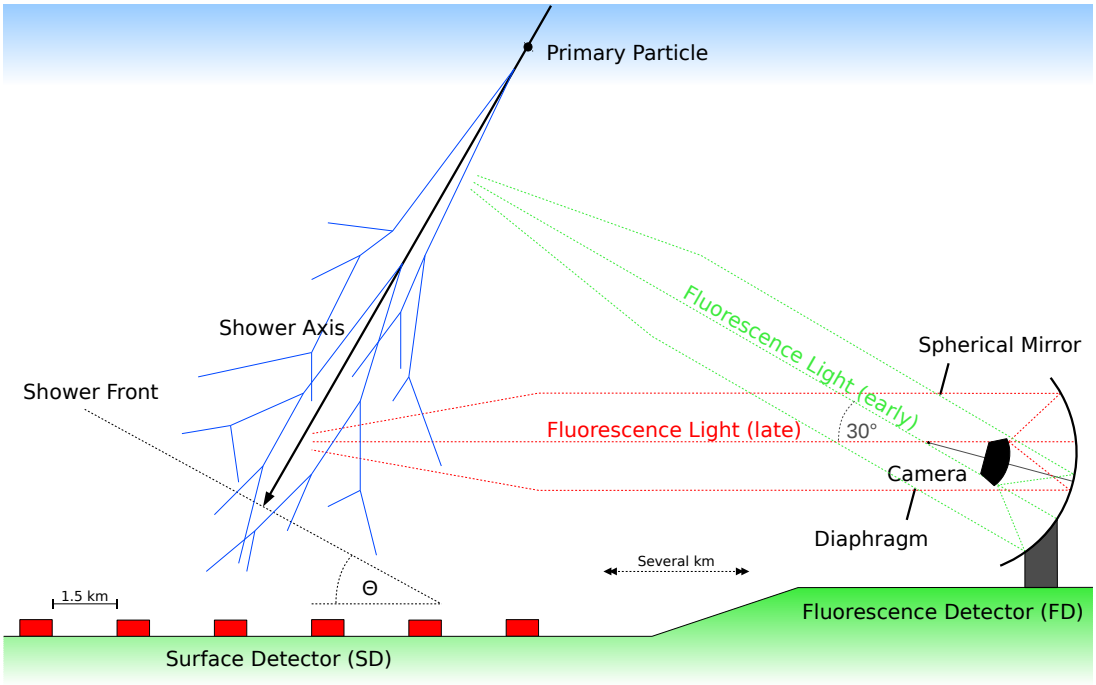

Figure 2.4.2.: Scheme of the hybrid detection principle established at the Pierre Auger Observatory. The longitudinal shower development of the extensive air shower is recorded by the fluorescence detector whereas the lateral profile is measured with the surface detector.

path of light. The radius of curvature is $R = 1.743\,\mathrm{m}$. A wide field of view of $30\,^\circ$ in azimuth and $28.1\,^\circ$ in elevation is achieved.

The camera is formed by a matrix of $22 \times 20 = 440$ photomultiplier tubes each with a hexagonal entrance window, which is 40 mm wide from side to side. The spacing between the single tubes is 2.8 mm. To minimize the dead space between the pixels, flat light guides, called "Mercedes stars", are placed in front of each photomultiplier tube. Therefore, the light collection efficiency of the focal plane could be increased from 70 % to 94 %. The Photonis XP3501 photomultiplier tube has a peak quantum efficiency of 30% at a wavelength of $\lambda = 330\,\mathrm{nm}$.

The overall transmission efficiency of the optical system has been determined by ray-tracing simulations to 55%. A big light loss is introduced by the obstruction of the mirror by the camera. Nevertheless, the fluorescence detector is capable of measuring the longitudinal shower development at full triggering efficiency for $10^{19}\,\mathrm{eV}$ showers over the entire surface array. In comparison to the surface detector, the fluorescence detector can only be operated in moonless nights. This results in a duty cycle of $10 - 15\,\%$.

The following chapter will emphasise the advantages and disadvantages of silicon photomultipliers in comparison to the conventional tubes used at the Pierre Auger Observatory.

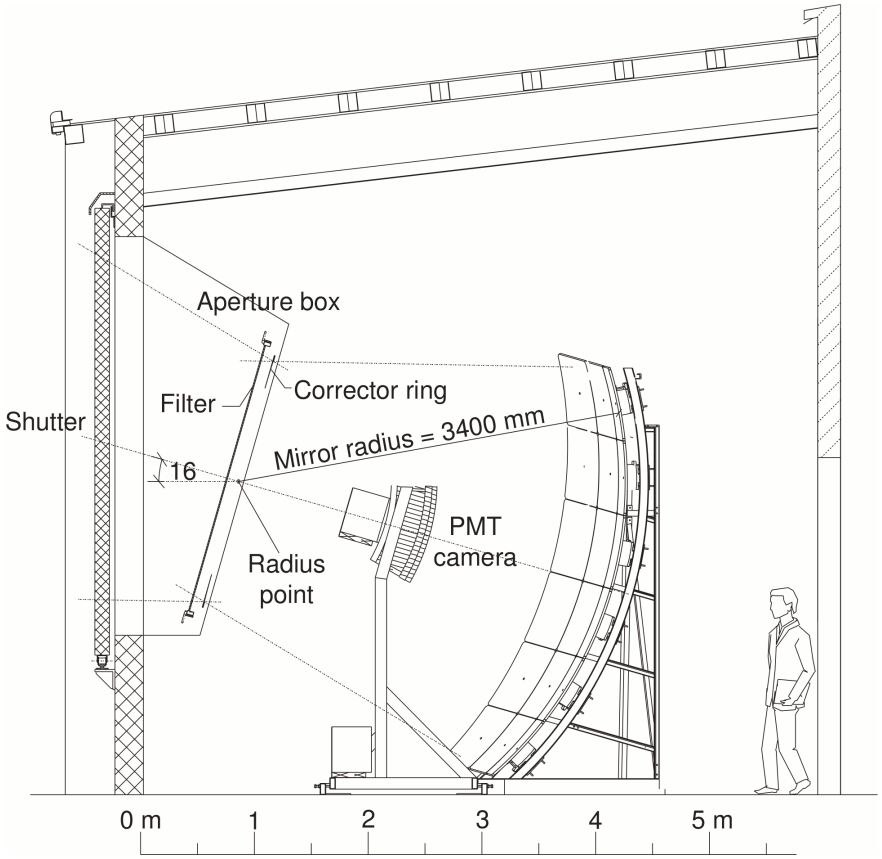

Figure 2.4.3.: Schematic of the optical system of the fluorescence detector. Fluorescence light enters the telescope through the aperture and gets reflected by the spherical mirror onto the curved camera surface. Taken from [13].

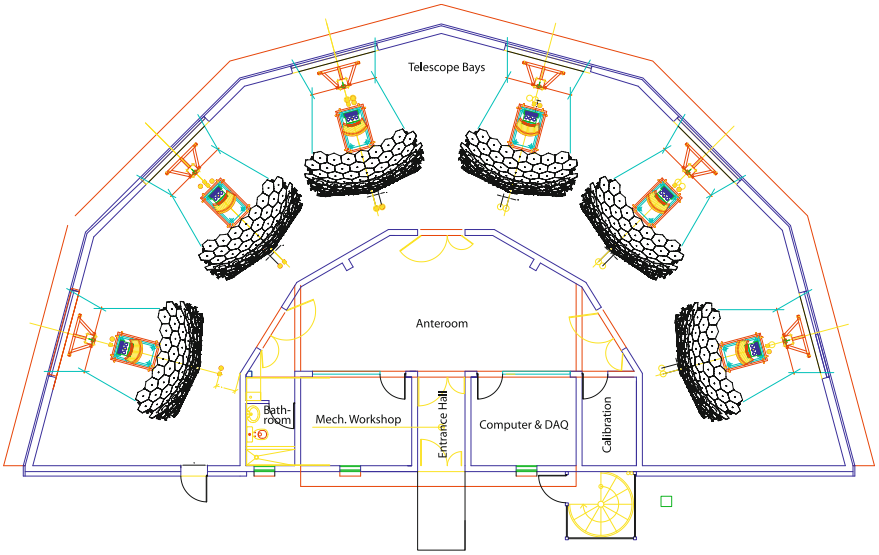

Figure 2.4.4.: Schematic of a telescope building housing six telescopes. Taken from [13].

Chapter 3.

Silicon Photomultiplier

Silicon photomultipliers (SiPMs) are a relatively young technology for the detection of single photons. They have several advantages over conventional photomultiplier tubes (PMTs). PMTs have a big entrance window of several square centimeters but are very elongated because they have to house several acceleration stages. Furthermore, the dynodes have to be powered by a high voltage of several 100 V. In contrast, the SiPM is very compact, has a sensitive area of some square millimeters and can be powered by a moderate voltage of typically $30\,\mathrm{V} - 150\,\mathrm{V}$. The intrinsic gain at the level of 10^6 depending on the operation parameters is comparable to the gain of a PMT. For an ideal SiPM the output signal is directly proportional to the number of detected photons.

However, there are some disadvantages regarding noise effects. The operation of the SiPM depends heavily on the environmental temperature. A high temperature can cause the SiPM to increase its already very high thermal noise output. Furthermore, there are some correlated noise phenomena to be considered.

The most important benchmark of a photon counting device is the photon detection efficiency (PDE). Today's SiPMs have nearly reached the efficiency levels of PMTs and further improvements are to be expected since new manufactures joined the business having good ideas how to overcome some of the noise effects. If noise can be suppressed, the dynamic range of SiPMs can be used more efficiently.

3.1. Geiger-Mode Avalanche Photodiode

The capability to output a signal which is directly proportional to the number of detected photons is created by the cellular substructure (see photograph in figure 3.1.1) of the sensitive area. Each cell is represented by a photodiode operated in Geiger-mode in series with a resistor. As presented in figure 3.1.2b, the cells get connected in parallel to a common load.

The schematic of an avalanche photodiode is shown in figure 3.1.2a. A wafer of about $300\,\mu$m thickness and low resistivity gets coated with an n-doped epitaxial layer. The p-n junction is then created by the diffusion of dopants with high concentrations into the epitaxial layer. A thin heavily n-doped and on top of that a thin heavily p-doped layer are created. The wafer gets connected to the cathode and each individual cell to

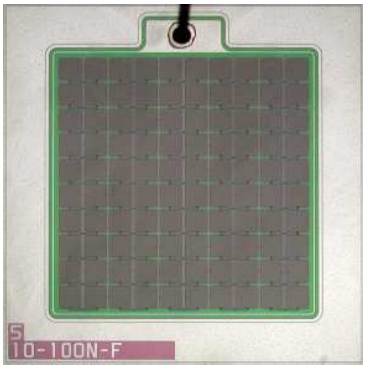

Figure 3.1.1.: Macro-photo of the sensitive area of an SiPM. The area is $1 \times 1\,\mathrm{mm}^2$ and features a matrix of 10×10 individual, square Geiger-mode avalanche photodiodes. The space in between the grey squares is not sensitive. Adapted from [17].

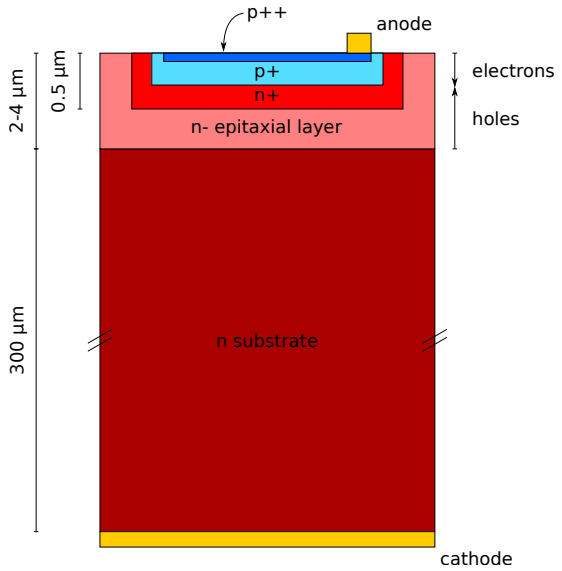

(a) Schematic of an avalanche photodiode. Not shown are the passivation layers and the quenching resistor which is connected to the anode [18].

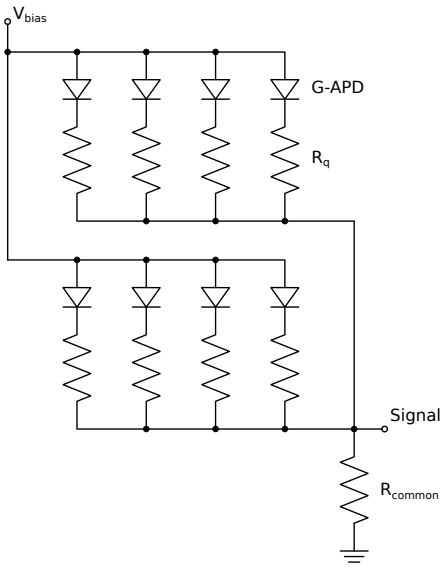

(b) Schematic of the circuit. A matrix of Geiger-mode avalanche photodiodes and their serial quenching resistors R_q are connected in parallel via a common load R_{common} to the bias voltage V_{bias}.

Figure 3.1.2.: Schematic of an SiPM

the anode. By applying a reverse voltage V_{bias}, a depletion zone forms at the junction. For operating in Geiger-mode, the voltage has to be high enough to nearly fully deplete the upper two layers. This voltage is referred to as breakdown voltage V_b. The excess over V_{b} is the over-voltage

$$V_{\mathrm{ov}} = V_{\mathrm{bias}} - V_{\mathrm{b}} \tag{3.1.1}$$

An incident photon might get absorbed in a fraction of a micrometer and creates an electron-hole pair. The charge carriers get accelerated in the depletion zone and due to the high electric field they gain enough energy to create further electron-hole pairs themselves. This creates a self-sustaining avalanche of charge carriers. The increasing

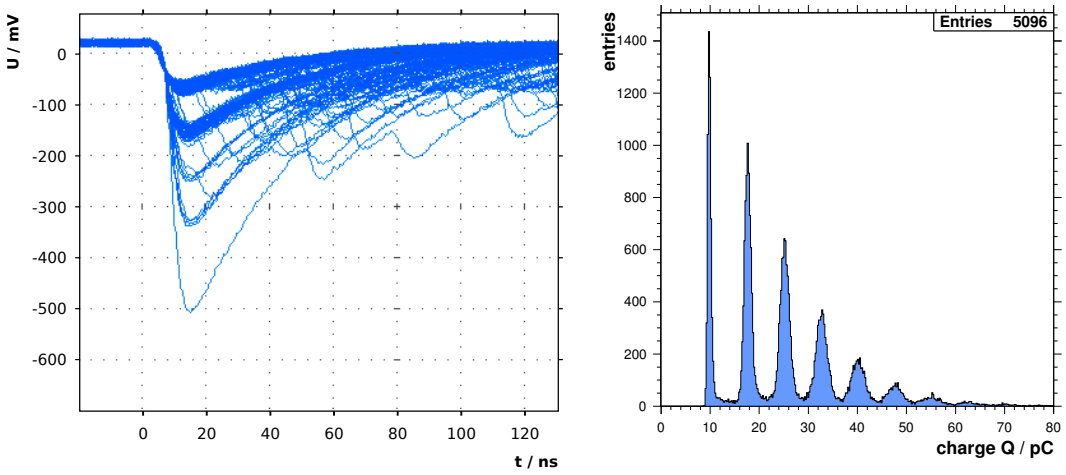

(a) Typical oscilloscope reading. Different numbers of coincidentally triggered cells result in the clearly distinguishable signal depths.

(b) Typical charge distribution as it can be recorded with a charge to digital converter (QDC) integrating the traces shown on the left. Each peak represents a certain number of cell breakdowns.

Figure 3.1.3.: Typical signal of an SiPM. The plots have been obtained from a measurement with a pulsed light source [19].

current flow raises the voltage across the quenching resistor which is connected in series to the Geiger-mode avalanche photodiode (G-APD). Therefore, the voltage across the photodiode and thus the electric field in the depletion zone decreases until it is no longer strong enough to support the self-sustaining avalanche. The measured signal is always equally high and denoted as one photon-equivalent. The number of photon-equivalents is equal to the number of fired G-APDs in the SiPM. Figure 3.1.3 gives an example of a typical output of an SiPM. Both the voltage trace and the integrated spectrum feature clearly distinguishable peaks corresponding to a certain number of simultaneous cell breakdowns. Once the avalanche is stopped, the G-APD has to rebuild the depletion zone before it can trigger again [18]. The resistivity R and the intrinsic capacitance C determine the time constant of the recharging process

$$t_{\mathrm{rec}} = R \cdot C \quad . \tag{3.1.2}$$

For a high dynamic range, the recovery time t_{rec} has to be as small as possible. A typical value for a Hamamatsu $1 \times 1\,\mathrm{mm}^2$ SiPM is $t_{\mathrm{rec}} \approx 30\,\mathrm{ns}$ [20]. Measurements of the recovery time indicate that it increases with the number of cells on the SiPM because of the common load, which limits the current flow, and with the cell pitch because of the higher intrinsic capacitance.

Typically, the SiPM gets coated with a resin which has a smaller refractive index $n_{\mathrm{resin}} \approx 1.5$ than the underlying silicon $n_{\mathrm{Si}} \approx 4.3$ for $\lambda \approx 400\,\mathrm{nm}$ [21]. This smoothens the optical transition and helps to increase the transmission of light to the sensitive areas of the SiPM.

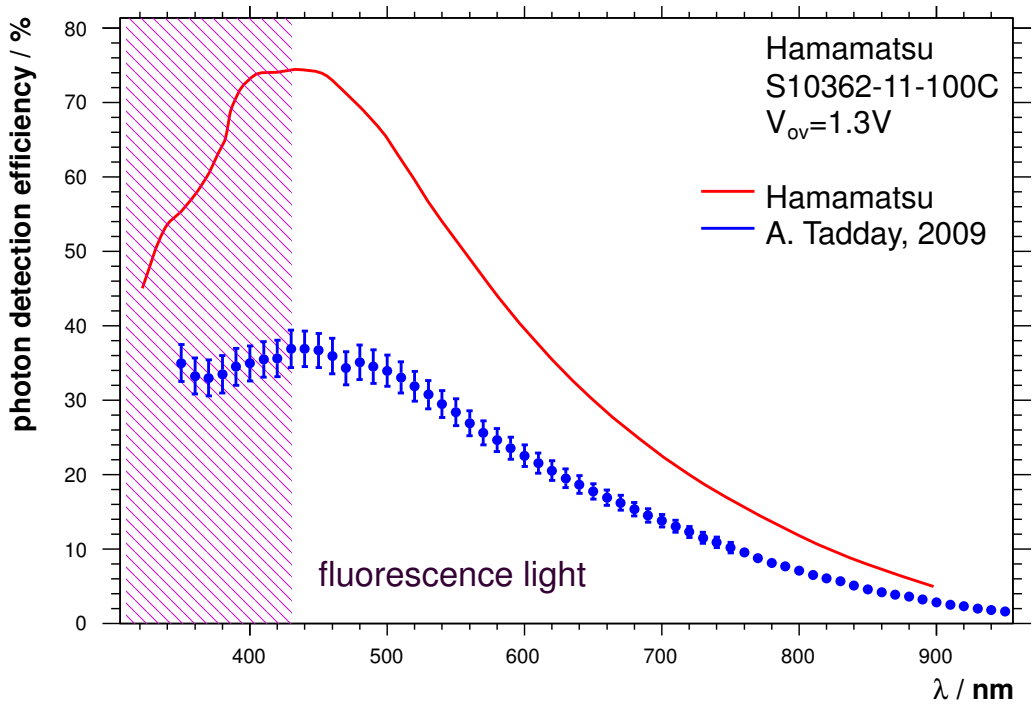

Figure 3.2.1.: Photon detection efficiency measurements of a Hamamatsu $1\times1\,\mathrm{mm}^2$ SiPM with $100\,\mu$m cell pitch in dependence on the wavelength. The efficiencies from Hamamatsu include the effects of correlated noise and are thus overestimated [22, 23].

3.2. Photon Detection Efficiency

The photon detection efficiency is given by

$$PDE(\lambda) = \epsilon_{\mathrm{geom}} \cdot \epsilon_{\mathrm{avalanche}} \cdot QE(\lambda) \quad , \tag{3.2.1}$$

with the geometrical fill factor ϵ_{geom}, the trigger probability $\epsilon_{\mathrm{avalanche}}$ and the quantum efficiency QE. The geometrical fill factor is the quotient of the active to the total area

$$\epsilon_{\mathrm{geom}} = \frac{A_{\mathrm{active}}}{A_{\mathrm{total}}} < 1 \quad . \tag{3.2.2}$$

This reduction is caused by the quenching resistor which lies on top of the substrate and the needed electrical separation of the single cells. The trigger probability $\epsilon_{\mathrm{avalanche}}$ is the probability for an electron-hole-pair to start the avalanche process. Due to the Geiger-mode, it is intrinsically close to 100 % in the depletion zone with the high electric field. The parameter of the highest interest and tuning scope is the quantum efficiency QE which is the probability for an incoming photon to create an electron-hole-pair. The PDE can be increased by adjusting the thickness of the upper depleted layers in such a way that the mean free path length of the incoming photons corresponds to the position of the depletion zone [18]. Thus, the sensitivity in the ultraviolet light regime with $\lambda < 400\,\mathrm{nm}$ could be improved by reducing the thickness of the first layer.

The results of a measurement of the PDE of a Hamamatsu SiPM are shown in figure 3.2.1 aside to the specifications of the manufacturer. The efficiencies are overestimated by the effects of correlated noise being discussed in the next section.

3.3. Noise Phenomena

The electrical breakdown in an individual cell can not only be caused by an absorbed photon but also by thermal excitation, self emitted photons (optical cross-talk) or by defects in the silicon lattice (after-pulses). The latter two are referred to as correlated noise.

It is crucial to understand all these effects in order to determine the optimal operation mode on the one hand, and on the other to be able to derive the original photon flux from the measurement.

3.3.1. Thermal Noise

The charged and ready-to-trigger SiPM cell can be accidentally activated by a thermally generated electron-hole pair which can gain enough energy in the high electric field of the depletion zone to start an avalanche process itself. The typical noise rate of an SiPM cell is

$$f_{\mathrm{th}} \approx 10\,\mathrm{kHz\ cell}^{-1} \quad . \tag{3.3.1}$$

The rate of thermally generated breakdowns can be measured by operating the SiPM in total darkness. It drops by a factor of 2 every 8 °C drop in temperature [18]. This becomes a problem for large area SiPMs with many 1000 cells. For example, Hamamatsu's 4×4 array of $3 \times 3\,\mathrm{mm}^2$ SiPMs with a cell pitch of $100\,\mu$m has 3600 cells. The thermal noise rate is then already in the MHz regime. Furthermore, all noise events have the chance to additionally cause correlated noise.

3.3.2. Optical Cross Talk

During the avalanche there is also the chance an electron recombines with its counterpart and a photon gets emitted. There are four possible mechanisms which can trigger a neighbouring cell (see figure 3.3.1). The cross-talk photon may be transmitted directly or via internal reflections into another avalanche region and can get absorbed. The third possibility is the creation of an electron-hole pair in the n-substrate beneath the avalanche region. This pair can drift into the avalanche region. Very unlikely is the transmission of the cross-talk photon through the coating layers. The neighbouring cell is not able to distinguish the cross-talk photon from a signal photon and therefore an avalanche may occur. The measured probability for a single cell to cause a cross-talk induced avalanche is

$$P_{\mathrm{cross}} = (18.2 \pm 0.1)\ \% \tag{3.3.2}$$

for a Hamamatsu $3 \times 3\,\mathrm{mm}^2$ SiPM with $100\,\mu$m cell pitch operated at an over-voltage $V_{\mathrm{ov}} = (1.31 \pm 0.01)$ V and at a temperature of $T = (1.0 \pm 0.5)$ °C [25].

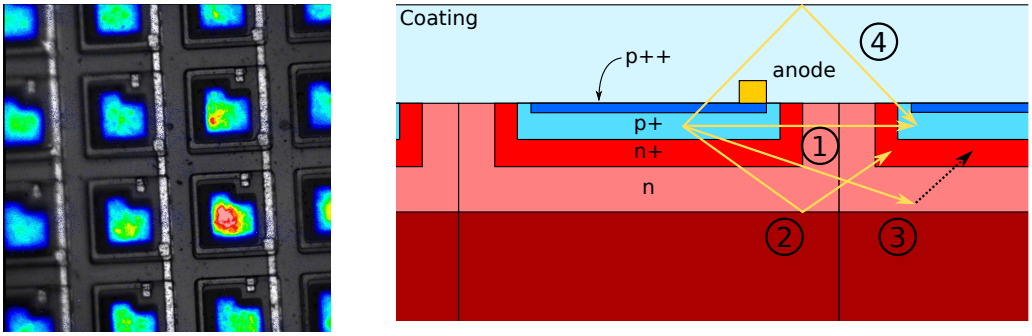

(a) Photo of an SiPM and an overlaying colour-coded intensity profile for a camera integration time of 300 s [24].

(b) Schematic of possible cross-talk photons. (1) Direct, (2) reflection at boundary ,(3) creation of electron-hole-pair and drift into avalanche region and (4) - very unlikely though - the transmission through the coating.

Figure 3.3.1.: Optical cross-talk

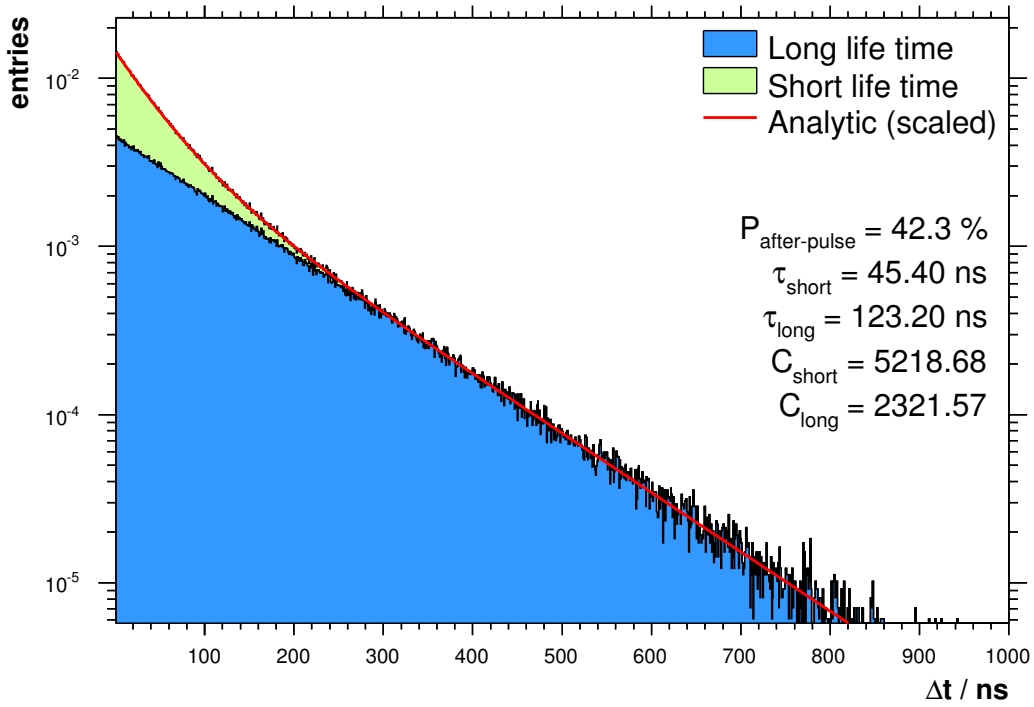

Figure 3.3.2.: Time lag of after-pulses to predecessor. The shown distributions of long (blue) and short (green) time constant after-pulses are obtained from a Monte-Carlo simulation based on a measurement by [25] of the Hamamatsu $1 \times 1\,\mathrm{mm}^2$ SiPM with $100\,\mu\mathrm{m}$ cell pitch operated at an over-voltage $V_{\mathrm{ov}} = (1.31 \pm 0.01)$ V and at a temperature of $T = (1.0 \pm 0.5)\,^{\circ}\mathrm{C}$. Thermal noise has been subtracted. The red curve denotes the exact formula.

3.3.3. After-Pulses

The avalanche created during a cell breakdown is basically a hot plasma of charge carriers. This enhances the possibility of electrons to fill traps caused by imperfections of

the silicon lattice. The delayed release of the electron can trigger the already recharged cell and an after-pulse is created. Measurements identified two components [18, 25]. The time lag Δt of a signal to the preceding avalanche follows a superposition of three exponential decays

$$P(\Delta t) = C_{\text{short}} e^{-\Delta t/\tau_{\text{short}}} + C_{\text{long}} e^{-\Delta t/\tau_{\text{long}}} + C_{\text{th}} e^{-f_{\text{th}}\Delta t} \quad . \tag{3.3.3}$$

The third component is the omnipresent thermal noise. Cross-talk can be easily omitted by rejecting coincident signals at $\Delta t \approx 0$ since it occurs instantaneously. Figure 3.3.2 shows the distribution of the time lag Δt after thermal noise subtraction for a Hamamatsu $3 \times 3\,\text{mm}^2$ with $100\,\mu$m cell pitch operated at an over-voltage $V_{\text{ov}} = (1.31 \pm 0.01)$ V and at a temperature of $T = (1.0 \pm 0.5)$ °C [25]. For this SiPM the two after-pulse time constants are determined to

$$\tau_{\text{short}} = (45.4 \pm 2.6) \text{ ns} \tag{3.3.4}$$

$$\tau_{\text{long}} = (123.2 \pm 14.0) \text{ ns} \quad . \tag{3.3.5}$$

The overall probability for the occurrence of after-pulses is

$$P_{\text{after-pulse}} = (42.3 \pm 2.0) \text{ \%} \quad . \tag{3.3.6}$$

The normalisation constants C can later be used to determine the ratio of short and long time constant after-pulses.

3.4. Simulation

All simulations in this work are done with the *Geant4* (Geometry and tracking) toolkit [26]. This framework simulates the passage of particles through matter while respecting a reasonable range of physics processes such as hadronic, electro-magnetic and, most important for this work, optical processes. It is commonly used in high energy physics and other fields of research to expose complex detector geometries to various physics models and studying their response. Written in the programming language *C++*, the object oriented design allows a fast adoption and easy manipulation of geometry.

In general, a simulation in *Geant4* is divided in several steps. There is a "run" which contains at least one "event". Each "event" is represented by at least one primary particle which gets shot onto the detector by the "particle gun". After tracking each primary and possibly their secondaries, an event is considered to be completed and the simulated detector is set to its initial state. Whenever a particle traverses a volume which has been made sensitive via associating a "sensitive detector", "hits" containing information on all physical quantities of interest are created and saved to a file.

The SiPM representation built for *Geant4* is a rectangular volume of an arbitrary material with a sensitive detector attached to it. In combination with an underlying phenomenological model, all effects observed in the laboratory are respected. This simple approach provides a good computing performance. An exact cellular model with different layers and coatings whose refractive indices reproduce the wavelength and incident angle dependent behaviour does not have to be incorporated. The developed

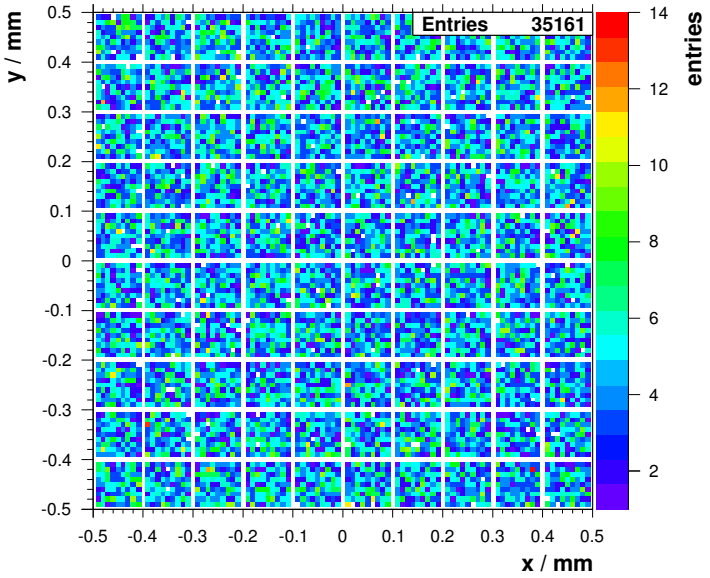

Figure 3.4.1.: SiPM surface hit position acceptance. Where the x- and y-axis denote the incident position of the photon on the simulated SiPM, the z-axis states the number of entries within $t = 1\,\mathrm{s}$. The binning was adjusted so the white spaces representing the cell spacings become visible.

phenomenological model describes all forms of noise discussed in the previous section and the recovery time of the individual cells. It is crucial to handle all these noise phenomena since they will constrain the dynamic range of the SiPM tremendously. The knowledge of the dynamic range is of great importance for any application.

3.4.1. Hit Filtering

The first mechanism of *Geant4* for the modelling of the response of a sensitive detector is the hit filtering. Such a filter is simply plugged into the sensitive detector instance and gets invoked each time a passing particle is to be detected. The Boolean answer of the filter after considering the physical properties of the particle lets the detector accept or reject the event.

At this stage of the simulation, only immediate effects can be considered. For the SiPM this is the photon detection efficiency. If a photon hits some dead space between the individual cells, it will get rejected. The dead space is introduced as a border surrounding each quadratic cell with equal width. Figure 3.4.1 histograms the position of incident photons on the surface of a $1 \times 1\,\mathrm{mm}^2$ SiPM. The white space between the single square areas which represent a single cell are thus not sensitive. The quantum efficiency is taken into account in two ways: the wavelength dependent component[1] $PDE_{\mathrm{wvl}}(\lambda)$ and the incident angle dependent component[2] $PDE_{\mathrm{angle}}(\theta)$. Approximating the trigger probability to $\epsilon_{\mathrm{avalanch}} \approx 100\,\%$ for ultra-violet light, the quantum efficiency is given

[1] Also referred to as "absolute PDE".
[2] Also referred to as "relative PDE".

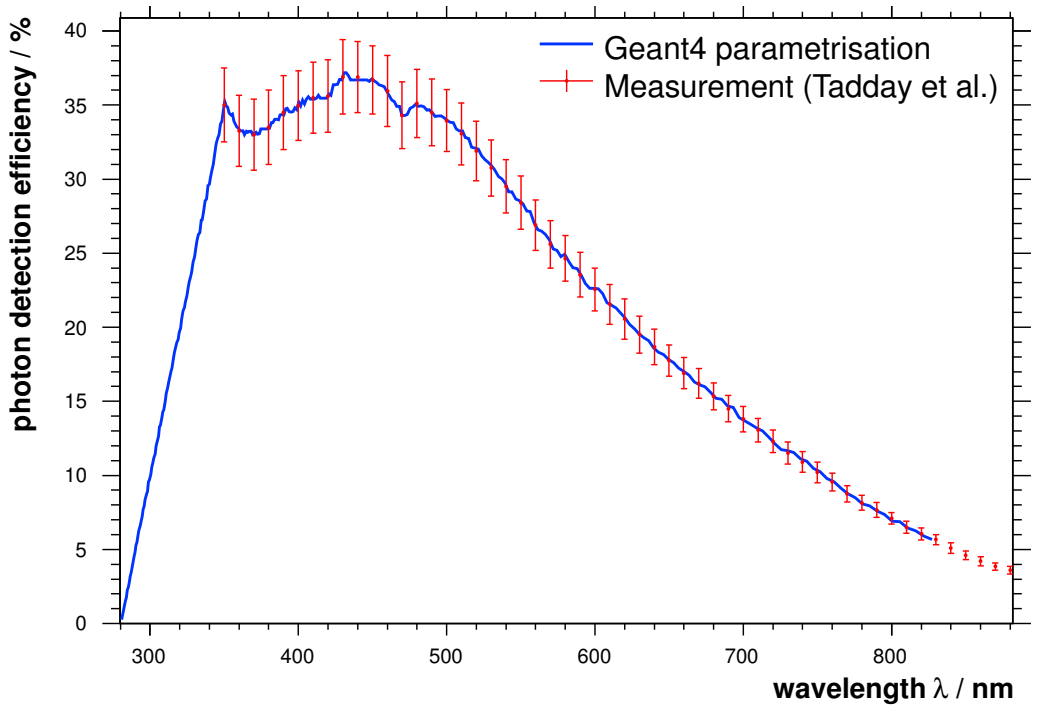

Figure 3.4.2.: Absolute photon detection efficiency $PDE_{\text{wvl}}(\lambda)$ with respect to wavelength. The red markers denote the measurement by Tadday et al. [22], the blue curve is the result of the *Geant4* parametrisation.

by

$$QE(\lambda,\theta) = \frac{PDE(\lambda,\theta)}{\epsilon_{\text{geom}}} = \frac{1}{\epsilon_{\text{geom}}} PDE_{\text{wvl}}(\lambda) \cdot PDE_{\text{angle}}(\theta) \quad . \tag{3.4.1}$$

Utilizing a random number generator of a uniform distribution, it can be diced, whether to accept or not accept the photon, with the condition

$$QE(\lambda,\theta) \leq rnd, \quad rnd \in [0,1] \quad . \tag{3.4.2}$$

Unfortunately, there are currently no measurements of the photon detection efficiency below $\lambda = 350\,\text{nm}$. Thus, a linear approximation has been chosen while assuming that the SiPM is essentially blind below $\lambda \leq 280\,\text{nm}$. The measurement by Tadday et al. [22] indicates an increasing PDE with smaller wavelengths which is not motivated by the Hamamatsu specifications. The result of the *Geant4* parametrisation, which reproduce the measurement in the laboratory, is shown in figure 3.4.2.

The behaviour of the relative photon detection efficiency as a function of the incident angle can be motivated by the multiple optical borders on top of the silicon substrate. Each layer either transmits or reflects the incoming photon according to the Fresnel equations [19]. As pictured in figure 3.4.3 this effect can also be nicely implemented into the hit filtering mechanism.

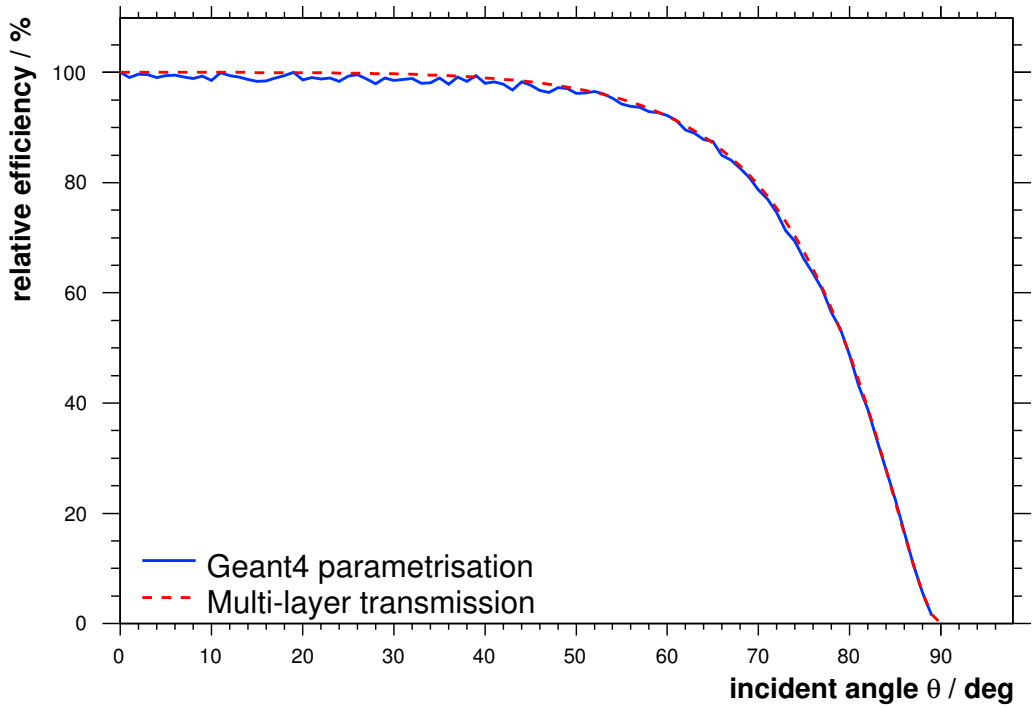

Figure 3.4.3.: Relative photon detection efficiency $PDE_{\text{angle}}(\theta)$ with respect to photon incident angle. The red dashed line is a theoretical prediction based on Fresnel equations for multiple layer transmission [19], the blue curve is the result of the *Geant4* parametrisation.

3.4.2. Digitization

The digitization mechanism of Geant4 is an extremely powerful one. It takes place after the "hits" of an "event" have been created. It is meant to transform all recorded raw physical quantities to a more realistic detector response. Since the user has full access to everything that has happened within the event, it is possible to consider effects which rely heavily on the timing of preceding hits. Digitization can also be used to simulate electronics, e.g. the response of an FADC (Flash amplitude to digital converter) which would provide a time-resolved voltage trace with a limited bandwidth.

For the simulation of the SiPM this mechanism is used to introduce thermal and correlated noise and the recovery time of the individual cells.

The first step is to determine the time range $\Delta t = t_{\max} - t_{\min}$ of the event. The number of thermal noise hits

$$N_{\text{thermal}} = f_{\text{th}} \left(t_{\max} - t_{\min} \right) \quad , \tag{3.4.3}$$

is uniformly distributed between $t_{\min}$ and $t_{\max}$. Since preceding thermal noise has an effect on the measurement, $t_{\min}$ is decreased by $t = 100/f_{\text{th}}$, so that each cell can have a mean of approximately 100 thermal noise induced hits before the actual simulation starts. Both, signal and thermal noise events are sorted into a priority queue which automatically sorts its elements in chronological order. This priority queue is traversed

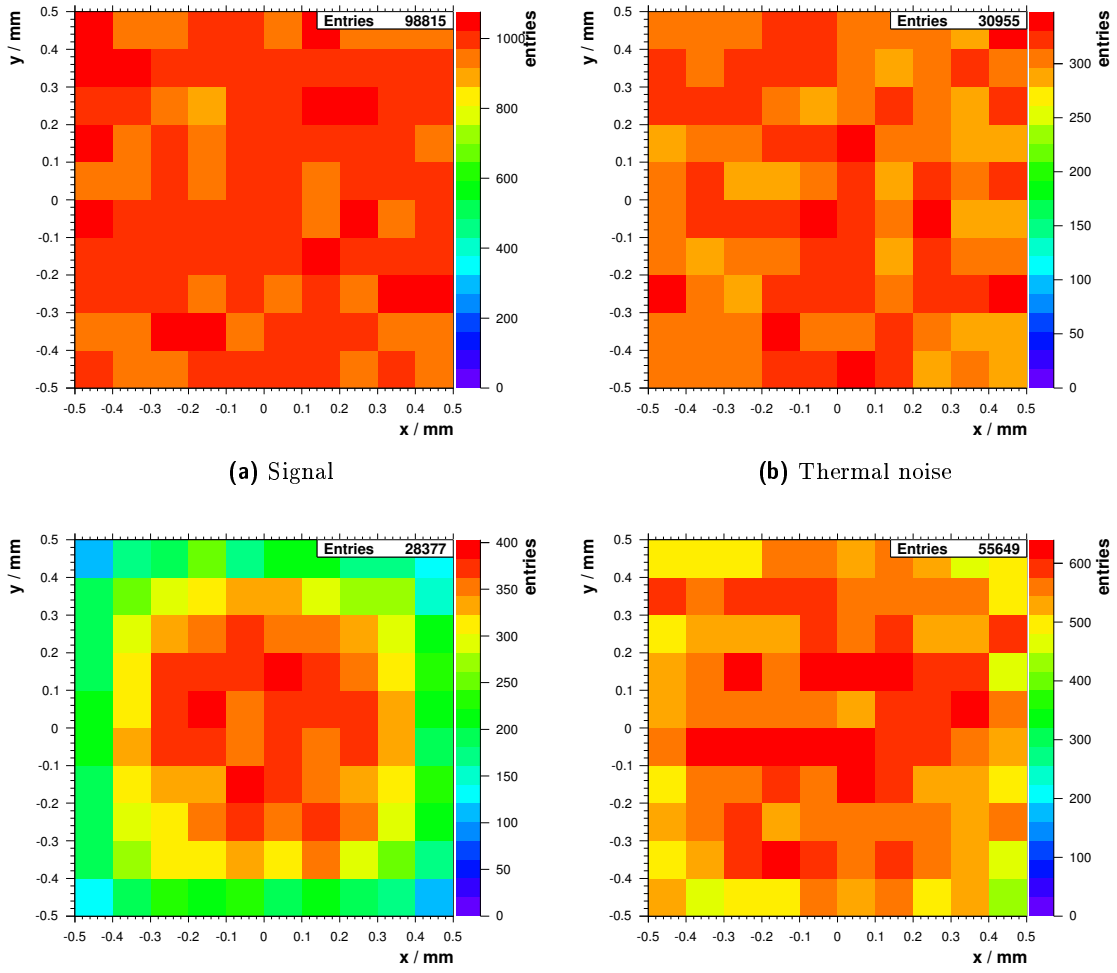

(a) Signal

(b) Thermal noise

(c) Cross-talk

(d) After-pulses

Figure 3.4.4.: Hit distribution on an SiPM surface simulated with Geant4. The flux is $\phi = 3.3\,\text{photons/ns}$ and the total count of signal photons $n_\gamma = 3 \cdot 10^5$ in $t = 990\,\mu\text{s}$. Each square bin represents an individual cell on the SiPM.

hit by hit. Every time a cell gets activated, it remembers the point in time t_{fire}. Successive hits on this cell have to meet

$$t > t_{\text{fire}} + t_{\text{rec}} \quad , \tag{3.4.4}$$

otherwise they will be dismissed. This rather hard criterion could be refined in future. If the cell triggering succeeds, the hit can produce correlated noise. For a given single-cell-cross-talk-probability P_{cross} it is diced

$$P_{\text{cross}} \leq rnd, \quad rnd \in [0, 1] \tag{3.4.5}$$

whether to create a cross-talk hit or not. The hit gets added to the priority queue with the same point in time as its parent. Since the emitted cross-talk photon travels through the material, its travel path length r is assumed to follow a Beer-Lambert-Law [27] preferring the next neighbour

$$P(r) = e^{-\alpha_{\text{cross}} r} \quad , \tag{3.4.6}$$

with $\alpha_{\text{cross}} \approx d_{\text{pitch}}$ whereas d_{pitch} denotes the cell pitch. The travel direction is determined by a uniformly diced polar angle. This approach ensures a reduced cross-talk probability for the edge cells as pictured in figure 3.4.4c. The successive traversing of the queue automatically introduces the possibility of multiple cross-talk photons to get released instantaneously.

After-pulses happen to be in the same cell they can have two different time constants τ_{short} and τ_{long}. The measurement of the time differences between a photon-equivalent and an after-pulse photon-equivalent reveals the fraction between those two. As shown in section 3.3.3 each part follows an exponential decay. The integrals of each part are:

$$I_{\text{th}} = \int_0^\infty C_{\text{th}} e^{-f_{\text{th}}\Delta t} \mathrm{d}\Delta t = \frac{C_{\text{th}}}{f_{\text{th}}} \tag{3.4.7}$$

$$I_{\text{short}} = \int_0^\infty C_{\text{short}} e^{-\Delta t/\tau_{\text{short}}} \mathrm{d}\Delta t = C_{\text{short}}\tau_{\text{short}} \tag{3.4.8}$$

$$I_{\text{long}} = \int_0^\infty C_{\text{long}} e^{-\Delta t/\tau_{\text{long}}} \mathrm{d}\Delta t = C_{\text{long}}\tau_{\text{long}} \quad . \tag{3.4.9}$$

The fraction of the short time constant pulses to all after-pulses is then given by

$$R_{\text{short}} = \frac{I_{\text{short}}}{I_{\text{long}} + I_{\text{short}}} = 0.45 \quad . \tag{3.4.10}$$

So if

$$R_{\text{short}} \leq rnd, \quad rnd \in [0,1] \tag{3.4.11}$$

a short time constant, otherwise a long time constant after-pulse according to the corresponding probability distribution

$$P(\Delta t) = e^{-t/\tau} \tag{3.4.12}$$

has to be fired. The overall probability for an after-pulse to happen can also be calculated from this measurement

$$P_{\text{after}} = \frac{I_{\text{short}} + I_{\text{long}}}{I_{\text{short}} + I_{\text{long}} + I_{\text{th}}} = (42.3 \pm 2.0)\ \% \tag{3.4.13}$$

(compare to [25]) and gets diced accordingly. The generated after-pulse hit gets inserted with the time $t = t_{\text{parent}} + \Delta t$ into the priority queue. Figure 3.4.4d shows the distribution of after-pulses for $\phi = 3.3\,\text{photons ns}^{-1}$ on a $1 \times 1\,\text{mm}^2$ SiPM. It is correlated to cross-talk in figure 3.4.4c since the occurrence is also reduced at the edges.

This simple model can be implemented with great computing performance because of the extensive usage of *C++* standard containers as for example *stl::priority_ queue* and a simple *comparator struct*. At this stage, the simulation fully reproduces the highly dynamic behaviour and thus the dynamic range of an SiPM.

3.4.3. Determination of the Dynamic Range

The dynamic range of a photon counting device is defined by the minimum and the maximum light flux (in units of photons per time) which the device is able to detect.

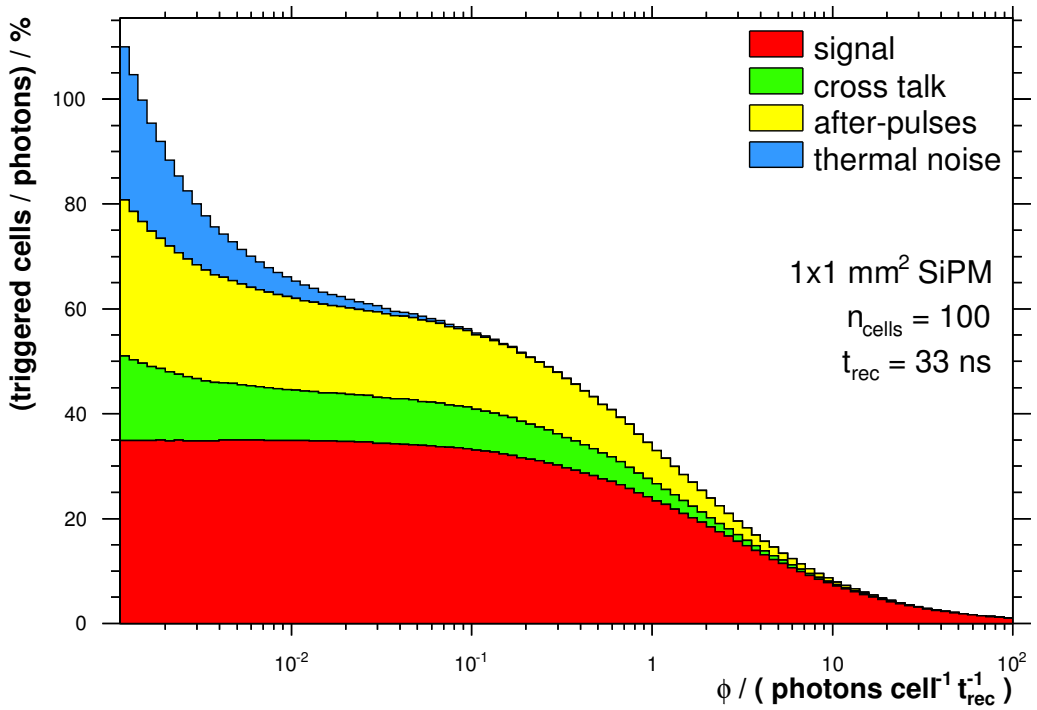

Figure 3.4.5.: Dynamic range of a $1 \times 1\,\mathrm{mm}^2$ SiPM. The x axis denotes the simulated flux which is given in terms of the number of photons per cell and recovery time. The efficiency on the y-axis is determined as the division of the amount of the triggered cells by the amount of tracked photons. Blue denotes thermal noise, yellow after-pulses, green cross-talk and red actual signal photons.

For low light fluxes, the response is dominated by noise which sets the lower bound. Within the dynamic range, the SiPM is expected to give a response proportional to the number of incoming photons. Near the upper bound of the dynamic range, the relation between the number of incoming - and detected photons is no longer linear. The dynamic range ends if a further increase of the photon flux does not increase the response as well. The SiPM is fully saturated.

The quotient of triggered cells and incoming photons of a *Geant4* simulation as a function of the light flux for the Hamamatsu $1 \times 1\,\mathrm{mm}^2$ SiPM is presented in figure 3.4.5. The light flux has been normalised to the number of cells and the recovery time.

Below 10^{-2} photons cell$^{-1}\,t_{\mathrm{rec}}^{-1}$, the response rises above 100 % which leads to an overestimation of the number of incoming photons. In comparison to the signal, the amount of noise is large because enough ready-to-trigger cells are available and therefore open to thermal noise and its correlated noise.

For a light flux of 1 photon cell$^{-1}\,t_{\mathrm{rec}}^{-1}$, the percentage of signal triggers is decreased by a third. This can be understood from the probability of a photon coming from an uniform light beam to hit a specific cell. Dicing 100 instantaneous photons onto 100 cells leads to an average hit count of each cell of approximately 1.5. Thus, only 2/3 of the photons could be detected if each cell is allowed to fire only once.

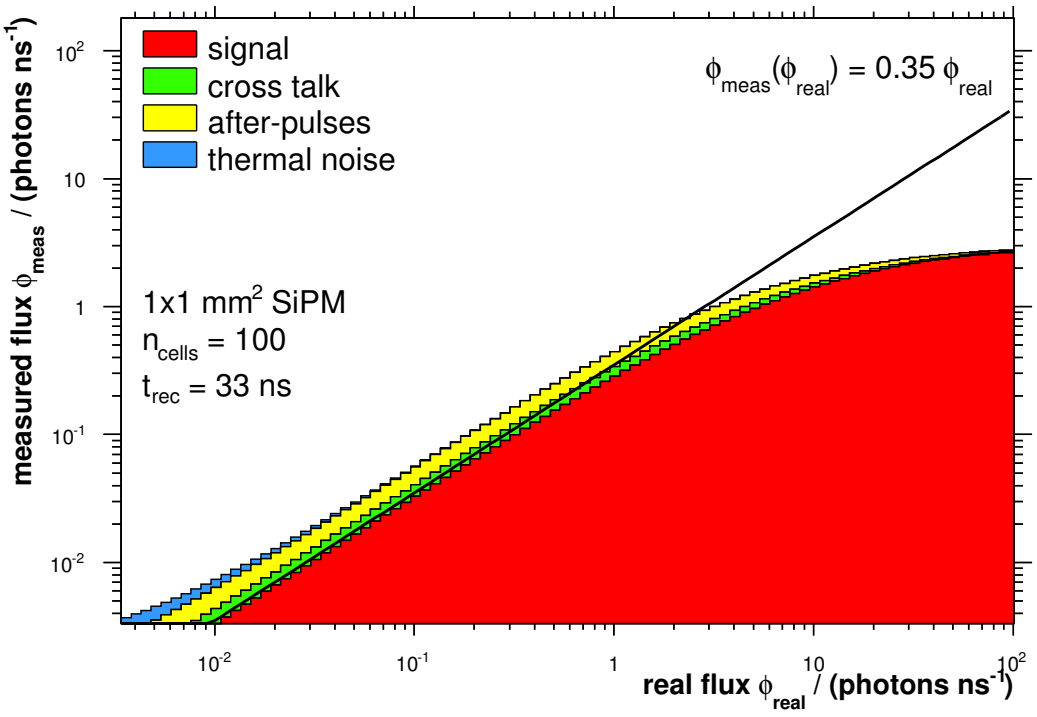

Figure 3.4.6.: Simulated "real" photon flux versus simulated "measured" photon flux for a $1 \times 1\,\mathrm{mm}^2$ SiPM. Blue denotes thermal noise, yellow after-pulses, green cross-talk and red actual signal photons. The slope of the black straight line is set to the photon detection efficiency.

In case of even higher photon fluxes with > 10 photons cell$^{-1}\, t_{\mathrm{rec}}^{-1}$, not only thermal noise gets heavily suppressed but also cross-talk and after-pulses. The measured flux is not significantly increased. The upper bound of the dynamic range of the SiPM is reached.

For a real application, it is crucial to translate the response of the SiPM given in terms of photon-equivalents to the real number of photons. The simulated calibration curve for the Hamamatsu $1 \times 1\,\mathrm{mm}^2$ SiPM is shown in figure 3.4.6. Again, saturation occurs above 1 photon cell$^{-1}\, t_{\mathrm{rec}}^{-1}$ and the linear relation between the real flux ϕ_{real} and the measured flux ϕ_{meas}, which is depicted as a black straight line, is no longer fulfilled.

Since SiPMs come in a small package with very small cells, it is essential to increase the effective sensitive area in order to improve the signal to noise level of a single camera pixel. This requires the use of light concentrators, namely Winston cones, as discussed in the next chapter.

Chapter 4.

Winston Cones

Formerly known as compound parabolic concentrators, Winston cones are motivated by the field of non-imaging optics and first appeared in 1966 as light concentrators for Cherenkov counters. It can be shown that a Winston cone reaches the theoretical maximum concentration [28]. Hence, the law of Liouville has an impact in phase space since the angular distribution of the concentrated beam gets broadened. Nevertheless, Winston cones promise to have several properties which are ideal for the application as light guides for SiPMs as they accept incoming photons up to a certain angle θ_{max} while having a constant and high transmission efficiency. Furthermore, the field of view of such a pixel formed by a Winston cone and an SiPM gets limited. This prevents scattered light from hitting the sensitive surface which would increase the noise signal in the sensor.

4.1. Construction

The construction principle of a Winston cone is very simple. After defining an entrance and an exit aperture, a beam of parallel light inclined by an angle $\theta_{\max}$ is directed onto the entrance. The individual rays are required to exit through a certain point at the exit aperture (see figure 4.1.1). This behaviour can be achieved by placing a reflecting parabola which is tilted by $\theta_{\max}$ with respect to its symmetry axis. Consequently, the symmetry axis is parallel to the light beam. The focal point of the parabola lies at the opposite side of the exit and coincides with the exit point used for the construction. Rays inclined greater than $\theta_{\max}$ get reflected to the opposite surface and leave the concentrator via the entrance.

The construction steps of the Winston cone already involve the maximum allowed entrance angle $\theta_{\max}$. The geometry can thus be fully described by the entrance - and exit aperture radii r_1 and r_2, $r_2 < r_1$

$$\sin\theta_{\max} = \frac{r_2}{r_1} = \frac{1}{c} \tag{4.1.1}$$

with the concentration c which is the theoretical maximum concentration [28]. The length of the Winston cone is given by

$$l = \frac{r_1 + r_2}{\tan\theta_{\max}} \quad . \tag{4.1.2}$$

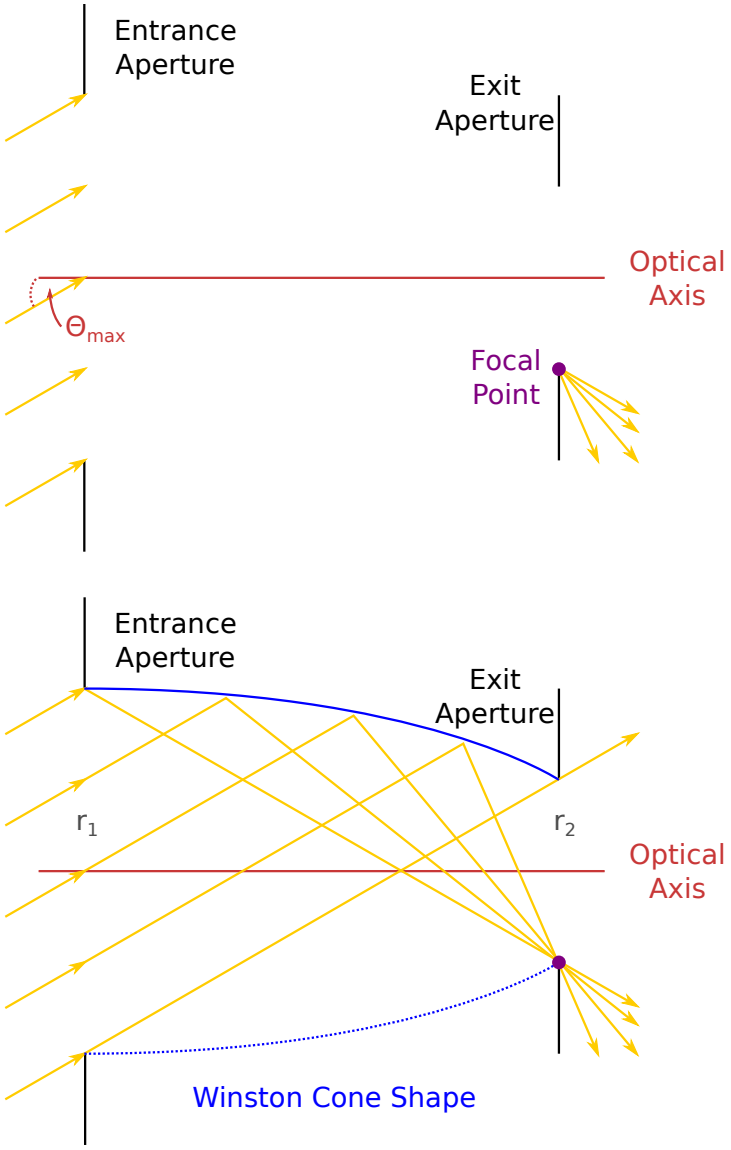

Figure 4.1.1.: Winston cone construction principle. After defining an entrance and an exit aperture, an inclined light beam is required to exit the concentrator through exactly one point in the exit plane. This behaviour can be achieved by using a parabola as reflector which is tilted by θ_{max} with respect to its symmetry axis.

With equations 4.1.1 and 4.1.2, the Winston cone is completely defined by only two of the three parameters r_1, r_2 and θ_{max}. The shape of a Winston cone can be described by

$$r(\theta) = \frac{1 + \sin\theta_{\text{max}}}{1 - \cos\left(\theta + \theta_{\text{max}}\right)} 2r_2 \tag{4.1.3}$$

with $\theta \in [\theta_{\text{max}}, \pi/2]$ (see figure 4.1.2) [28]. Transforming to Cartesian coordinates with

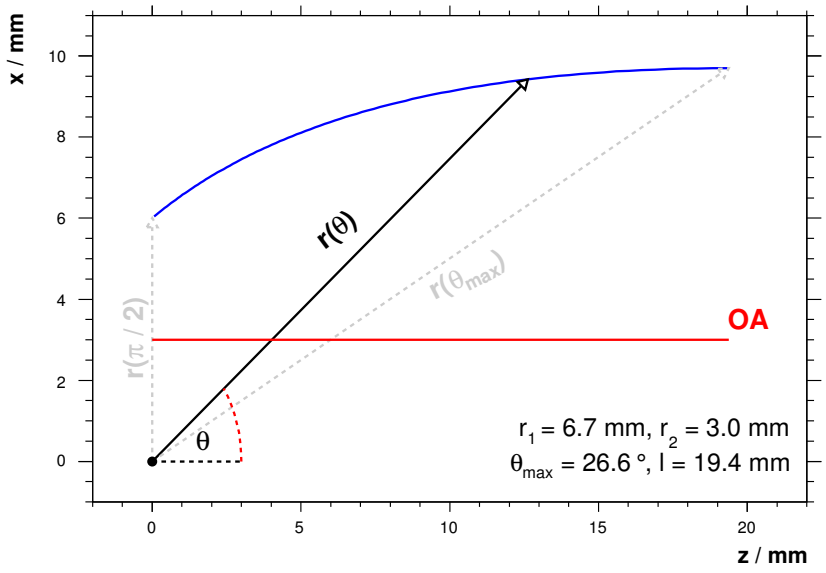

Figure 4.1.2.: Schematic of the definition of the Winston cone shape. The shape is denoted in blue whereas the black vector is given by $r(\theta) = 2r_2\,(1+\sin\theta_{\text{max}})\,/\,(1-\cos(\theta+\theta_{\text{max}}))$ in the range $\theta \in [\theta_{\text{max}}, \pi/2]$. The red line denotes the optical axis of the light concentrator.

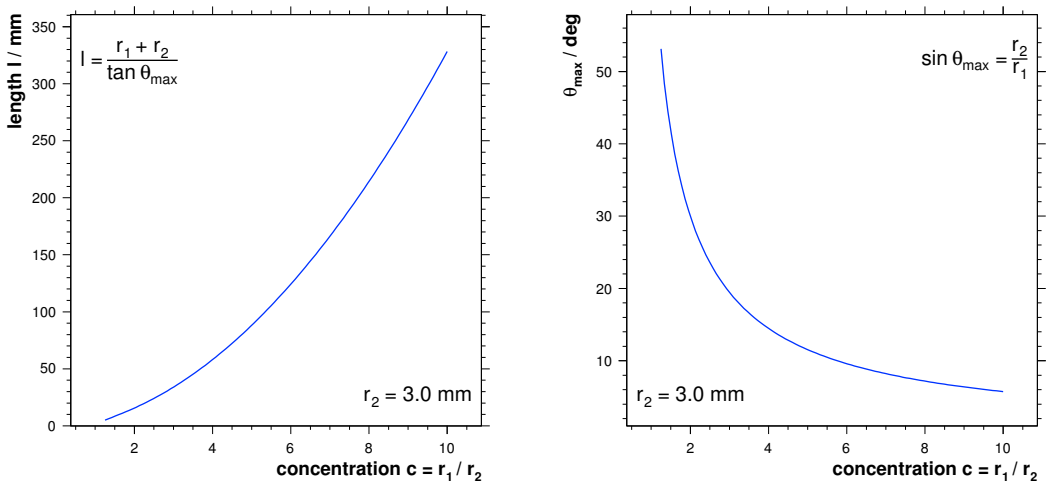

(a) Length l versus the concentration ratio c. θ_{max} is automatically defined by setting r_1 and r_2.

(b) θ_{max} versus the concentration ratio c.

Figure 4.1.3.: Free parameters of Winston cones.

the symmetry axis of the cone coinciding with the z-axis results in

$$x = r(\theta)\cdot\sin\theta - r_2 \tag{4.1.4}$$

$$y = r(\theta)\cdot\sin\theta - r_2 \tag{4.1.5}$$

$$z = r(\theta)\cdot\cos\theta \quad . \tag{4.1.6}$$

Figure 4.1.3 shows the relation of the length l and the maximum allowed incident angle

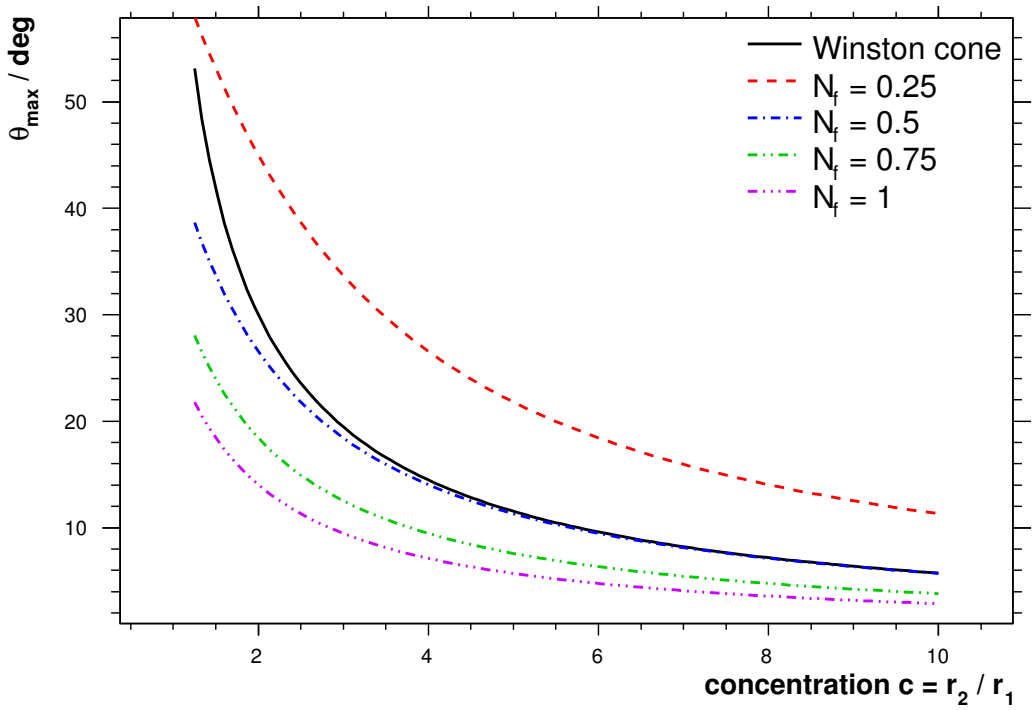

Figure 4.1.4.: Lens concentrators in comparison to a Winston cone. The various dashed lines denote the behaviour of a lens concentrator for a given focal ratio N_f.

θ_max for different concentration ratios c. A strong increase of the concentration ratio leads to a smaller θ_max and also to greater length. A good compromise with reasonable θ_max and length l has to be aimed for.

It can be proven that the same concentration can not be achieved by a conventional optical system e.g. consisting of a condenser lens. The quotient of the entrance aperture diameter D and the focal length f of this system with respect to the concentration c and θ_max can be derived to

$$\frac{D}{f} = 2\frac{r_1}{r_2}\tan\theta_\mathrm{max} \quad . \tag{4.1.7}$$

The inverse is denominated “focal ratio” or “f-number”

$$N_\mathrm{f} = \frac{f}{D} \quad . \tag{4.1.8}$$

As indicated in figure 4.1.4, an optical system has to have an unreasonable small focal ratio $N_\mathrm{f} < 0.5$ to be able to compete with a Winston cone. In addition, a refractive design has the disadvantage of placing much material in the light path which may implicate in the case of ultraviolet light a too small transmission efficiency.

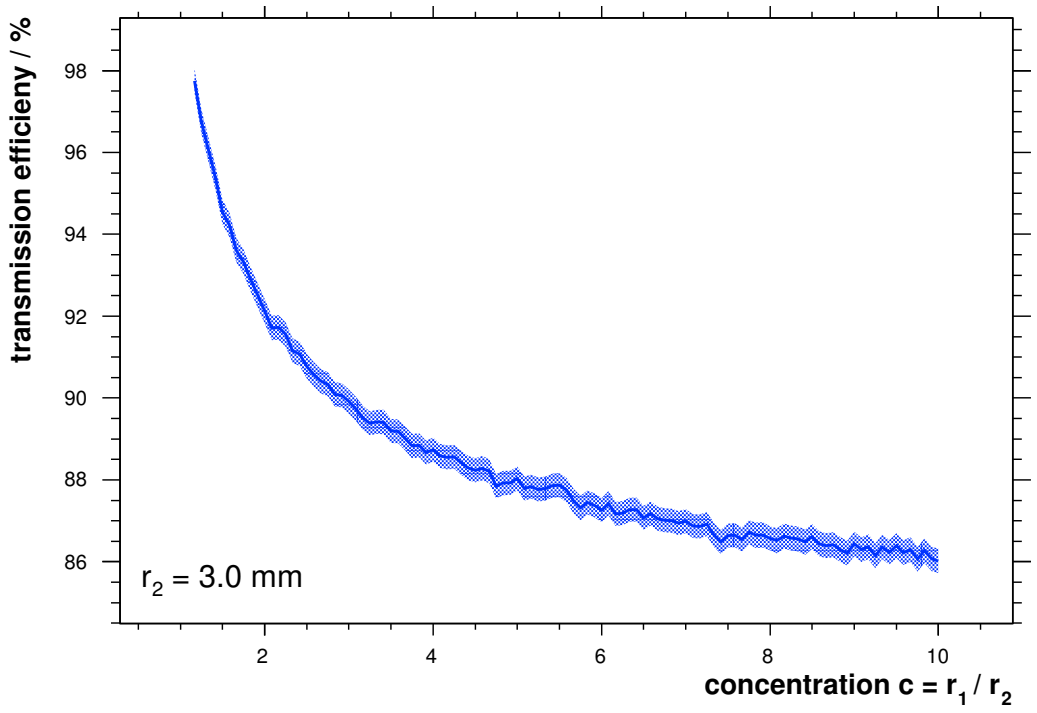

Figure 4.2.1.: Transmission efficiency versus concentration ratio for perpendicular incidence ($\theta_{\text{in}} = 0°$) of light. The curve has been obtained by a Geant4 simulation of a reflective Winston cone made of aluminium. The shaded area signifies the statistical uncertainty due to counting.

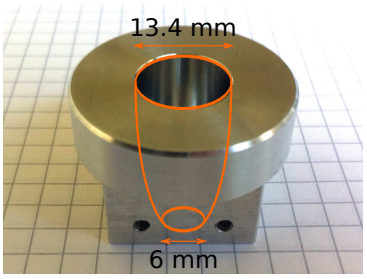

Figure 4.2.2.: Photo of a custom made Winston cone of aluminium constructed in the mechanical workshop of the Phys. Inst. IIIA, RWTH Aachen. The thickness of the border has been increased so it directly fits into the drawtube of a commercial Newton reflector.

4.2. Transmission Efficiency

The transmission efficiency is the strength of Winston cones because they only rely on reflection. For the determination of the transmission efficiency, the Geant4 simulation directs a beam of parallel light into the entrance of the cone. Listings B.1 and B.2, which can be found in the appendix of this thesis at page 95, shortly summarize the implementation of a Winston cone in Geant4 including a reflective surface. Since the sensitive area is defined at the exit of the cone, the efficiency is simply the number of

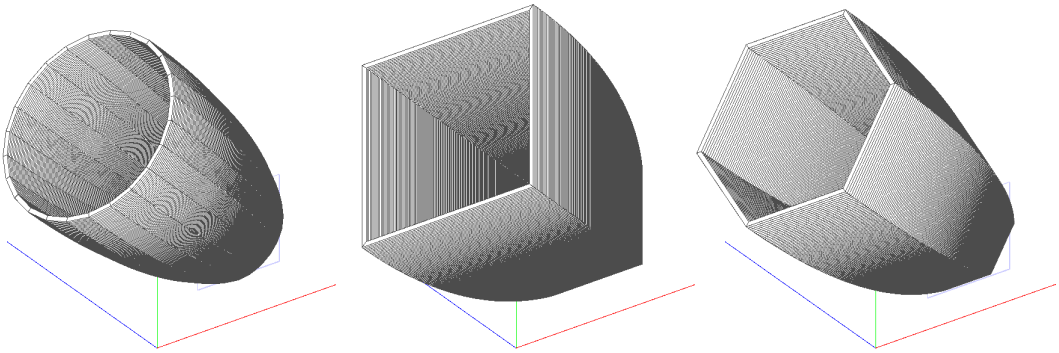

Figure 4.2.3.: Round, rectangular and hexagonal Winston cone shapes. The drawings have been obtained from the *Geant4* simulation.

detected photons divided by the amount of simulated ones.

The surface of the cone is simulated to be polished aluminium. Figure 4.2.1 shows the high transmission efficiency of the Winston cone. It is $T \approx 95\,\%$ for $c = 1.5$ and decreases with the concentration which can be explained by the bigger fraction of photons which has to be reflected at least once to get to the exit. For all further simulations the following parameters have been chosen

$$r_1 = 6.71\,\text{mm} \tag{4.2.1}$$
$$r_2 = 3.00\,\text{mm} \tag{4.2.2}$$
$$\theta_{\text{max}} = 26.6\,^\circ \tag{4.2.3}$$
$$l = 19.6\,\text{mm} \quad . \tag{4.2.4}$$

This geometry matches the desired size for the telescope design presented in section 5. For a first application a Winston cone has been produced (see figure 4.2.2) which directly fits into the drawtube of a commercial Newton reflector (Meade Bresser PN-203). This enabled first measurements with SiPMs exposed to the night-sky for determination of the expected background light flux [19].

4.2.1. Different Shapes

Beside the intuitive round shape of a light concentrator, a rectangular or a hexagonal profile (compare figure 4.2.3) may be realised as well in order to match the extends of the sensitive area or to prevent dead space when used in an array.

The simulated transmission efficiency of a round, rectangular and hexagonal shaped Winston cone can be found in figure 4.2.4. It can be seen that the transmission efficiency of all three shapes is $T \approx 90\,\%$ for small incident angles and quickly drops to zero near θ_{max}. In a nutshell, the closer the shape approximates a circle, the higher the transmission efficiency for incident angles $\leq \theta_{\text{max}}$ and the faster the drop to zero.

Unfortunately, it is a mechanically complex task to mill an elongated structure into aluminium which is not a solid of revolution. Thus, this work will focus on the circular Winston cone shape.

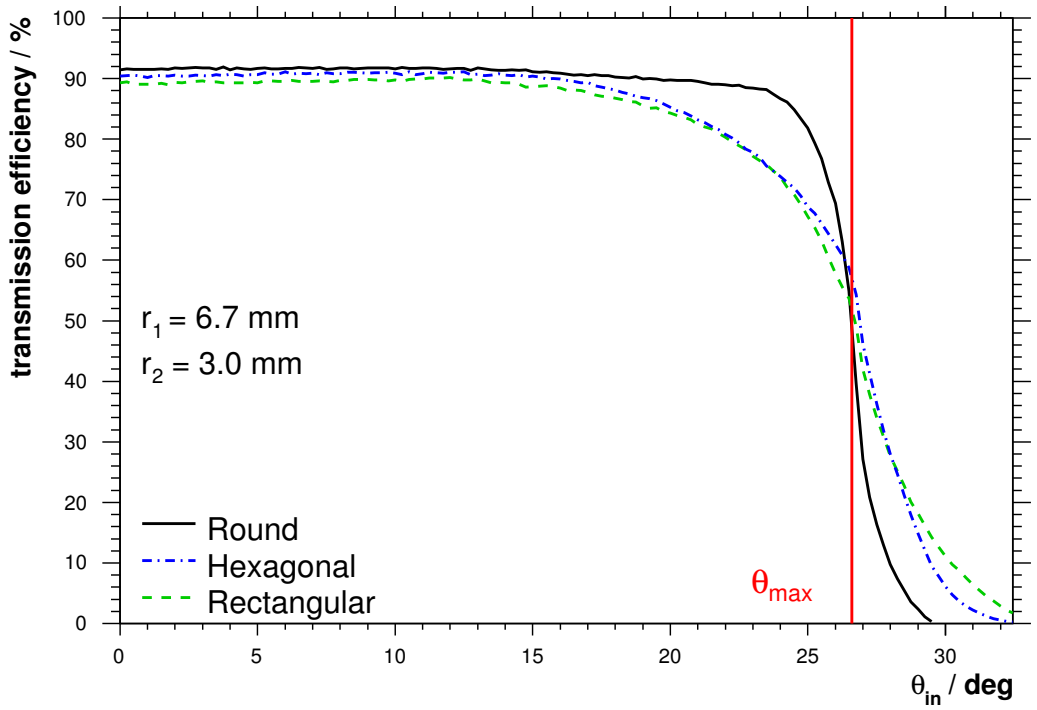

Figure 4.2.4.: Winston cone transmission efficiency for different shapes depending on the incident angle θ_{in}. The black line denotes the efficiency for the round, the dashed blue the hexagonal and the green the rectangular entrance.

4.2.2. Refractive Design

Replicating the Winston cone shape as a solid body, made of an ultraviolet transparent material such as acrylic or PMMA (polymethyl methacrylate), an optical border at the entrance of the concentrator is introduced. As light passes the solid cone, internal total reflection adopts the role of the aluminium. As Snell's law prescribes

$$\sin\theta'_{\text{max}} = \underbrace{\frac{n_{\text{acrylic}}}{n_{\text{air}}}}_{>1} \sin\theta_{\text{max}} \quad , \tag{4.2.5}$$

the optical border extends the maximum allowed incident angle. This allows to further increase the concentration without squeezing θ_{max}. Admittedly, bulk absorption of the material has to be dealt with. According to Beer's law [29] the probability to find a photon after a path length x in a medium with attenuation coefficient α, $[\alpha] = m^{-1}$ is

$$P(x) = e^{-\alpha \cdot x} \quad . \tag{4.2.6}$$

After a travelled path $x = \alpha^{-1}$ the survival probability drops to $1/e$. Having measured the transmission T through a material of the thickness d the attenuation coefficient is given by

$$\alpha = -\frac{\ln(T)}{d} \quad . \tag{4.2.7}$$

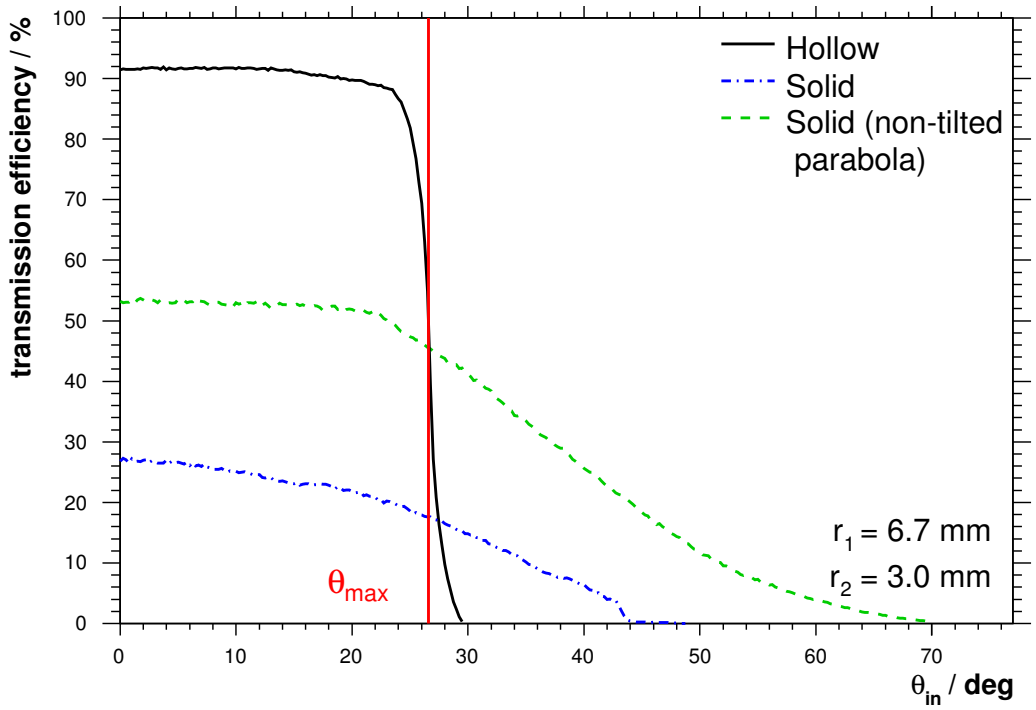

Figure 4.2.5.: Winston cone transmission efficiency for different solid types with respect to the incident angle θ_{in}. The hollow cone has been simulated to be made of polished aluminium, the solid ones of ultraviolet transparent PMMA. The black line shows the result for the hollow and the green and blue dashed for the solid design. For the green line the parabola defining the shape of the cone has not been tilted. Therefore, the symmetry axis of the parabola coincides with the optical axis of the Winston cone.

The intensity after traversing a path of x is then

$$I(x) = I_0 \exp\left(\frac{\ln(T)}{d} \cdot x\right) \quad . \tag{4.2.8}$$

For acrylic, the attenuation coefficient for a wavelength of $\lambda = 300\,\text{nm}$ is $\alpha \approx 0.031\,\text{mm}^{-1}$. The material thickness of $l = 19.6\,\text{mm}$ leads to a transmission of only $T = 54\%$. In order to decrease the length, a non-tilted parabola defining the borders of the solid concentrator can be employed. Therefore, the symmetry axis of the parabola coincides with the optical axis of the Winston cone. This procedure also increases the chance of total internal reflection at the borders for higher inclined photon beams. Thus, the length can be decreased to $l = 11.9\,\text{mm}$ and the transmission is $T = 69\,\%$.

The Geant4 simulation uses PMMA as refracting material. The result of the simulation as shown in figure 4.2.5, indicates that the refractive design succeeds in increasing the viewing angle but does not show any clear cut off anymore. Even though the moulding of angular shapes is easy, the solid cone is in fact far behind refracting design in matters of transmission efficiency and this makes it infeasible for the detection of very small light fluxes.

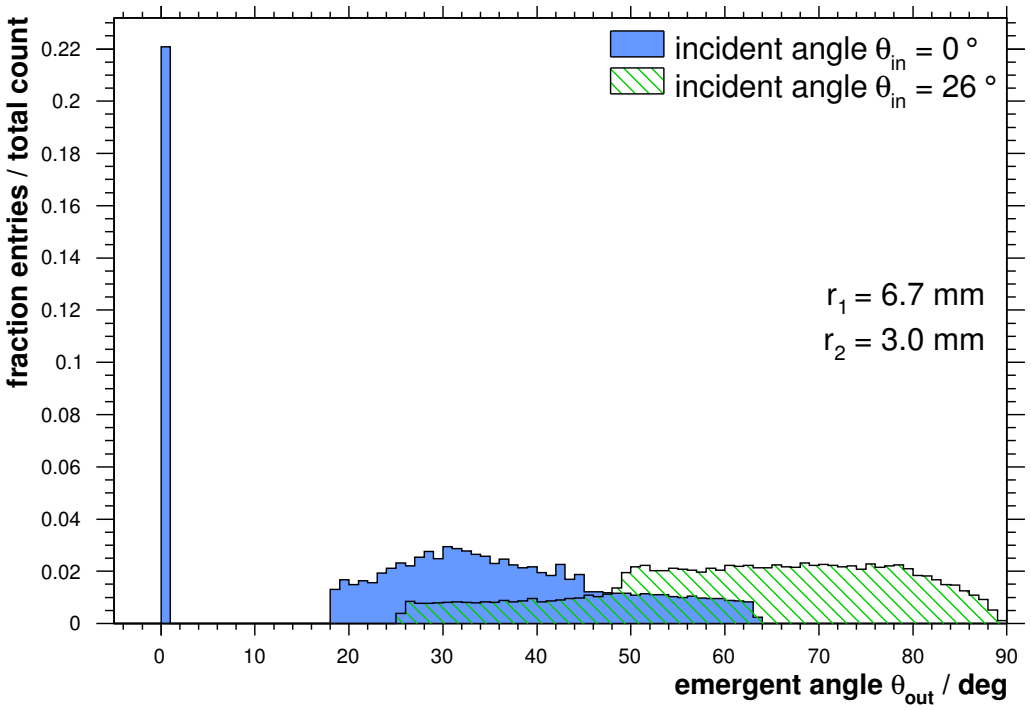

Figure 4.3.1.: Distribution of emergent angles of light leaving a Winston cone. The solid area denotes the distribution for a perpendicular incident light beam ($\theta_{in} = 0\,^\circ$), the dashed for an inclined light beam with $\theta_{\text{in}} = 26\,^\circ$.

4.3. Impact on SiPM Operation

For the operation of the Winston cone in combination with an SiPM, it is crucial to know the exact angular distribution of the photons leaving the Winston cone in terms of angle and position. Preferably, photons are distributed homogeneously over the surface of the SiPM and are not too inclined in order to be still detectable. But as figure 4.3.1 shows, photons leave the Winston cone over a wide range of angles as soon as they have been reflected. Furthermore, figure 4.3.2 shows ring like accumulations where the borders of the Winston cone exit meets the detector surface. The spatial distribution of the photons gets even worse for tilted beams. Hence, it is important to get information on the impact on the operation of the used detector.

For the simulation, a Hamamatsu 4×4 array of $3 \times 3\,\text{mm}^2$ SiPMs has been chosen as sensitive detector in combination with the $r_1 = 6.71\,\text{mm}$ and $r_2 = 3.00\,\text{mm}$ Winston cone. The SiPM has $n_{\text{cell}} = 3600$ cells, whereupon only

$$n'_{\text{cell}} = \frac{\pi r_2^2}{(2 \cdot r_2)^2} n_{\text{cell}} \approx 2828 \tag{4.3.1}$$

cells are not masked by the circular exit. Considering the recovery time t_{rec} and all noise effects of the SiPM, the reduction of the hit count for a moderate flux of $\phi = 1\,\text{photon ns}^{-1}$ becomes apparent as it can be seen in figure 4.3.3. For this example, the overall efficiency for parallel incoming light is $\epsilon \approx 22\,\%$. This implies a reduction of the

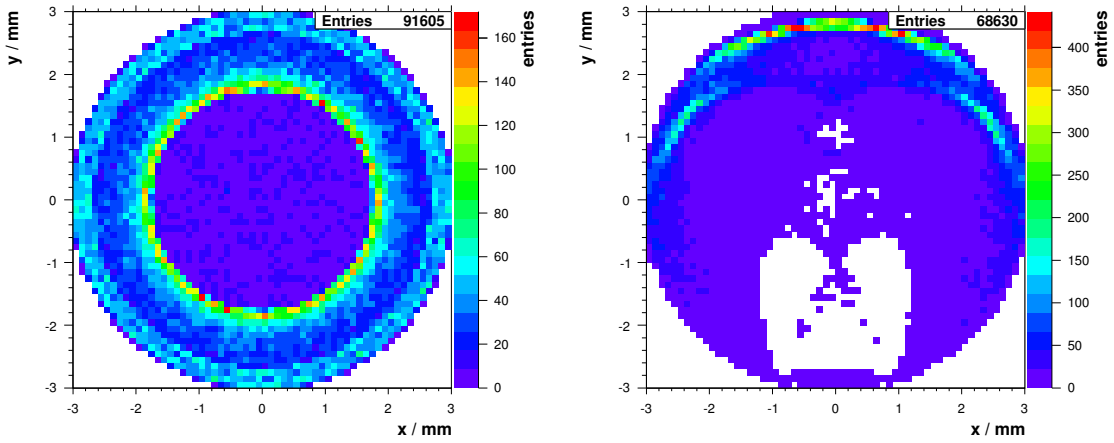

(a) Incident angle $\theta_{\text{in}} = 0\,^\circ$ **(b)** Incident angle $\theta_{\text{in}} = 26\,^\circ$

Figure 4.3.2.: Distribution of photon exit positions on an SiPM surface situated behind a Winston cone. The total number of simulated photons is $n_\gamma = 1 \cdot 10^5$. Each bin represents an individual cell. The dynamics of the SiPM have been neglected for this plots.

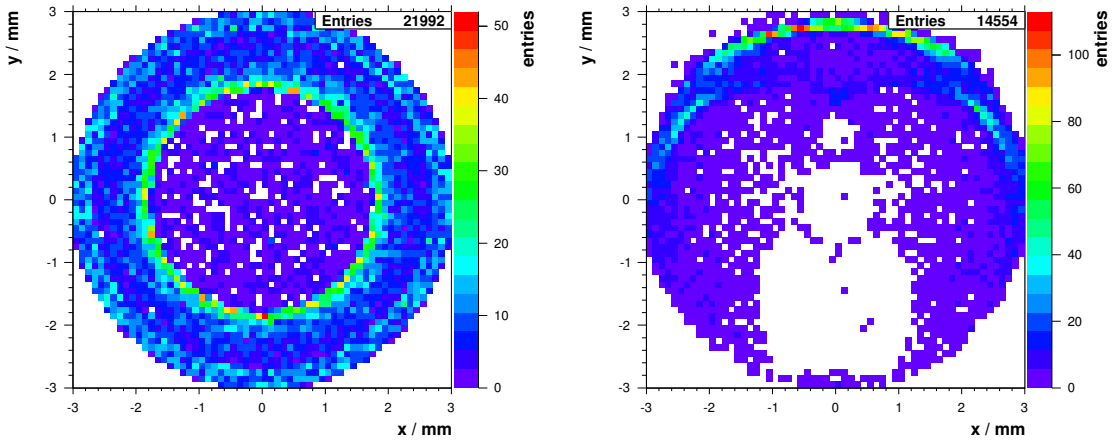

(a) Incident angle $\theta_{\text{in}} = 0\,^\circ$ **(b)** Incident angle $\theta_{\text{in}} = 26\,^\circ$

Figure 4.3.3.: Distribution of photon exit positions on an SiPM surface situated behind a Winston cone including the SiPM effects as presented in chapter 3. Each bin represents an individual cell. The histograms count signal hits for a simulated light flux on the Winston cone of $\phi = 1\,\text{ns}^{-1}$ and total number of photons $n_\gamma = 1 \cdot 10^5$.

$PDE(\lambda = 350\,\text{nm}) \approx 35\%$ in combination with the transmission efficiency $T \approx 90\,\%$ by approximately 30%. Examining each measurable component of the response separately as shown in figure 4.3.4, it can be seen that noise affects the whole SiPM and is not exclusive to the exposed area.

The effective reduction of the dynamic range of the SiPM becomes clearer if one varies the incident angles and light fluxes $\phi \in \left[10^{-3}, 10^{2}\right]$ photons ns^{-1}. The signal effi-

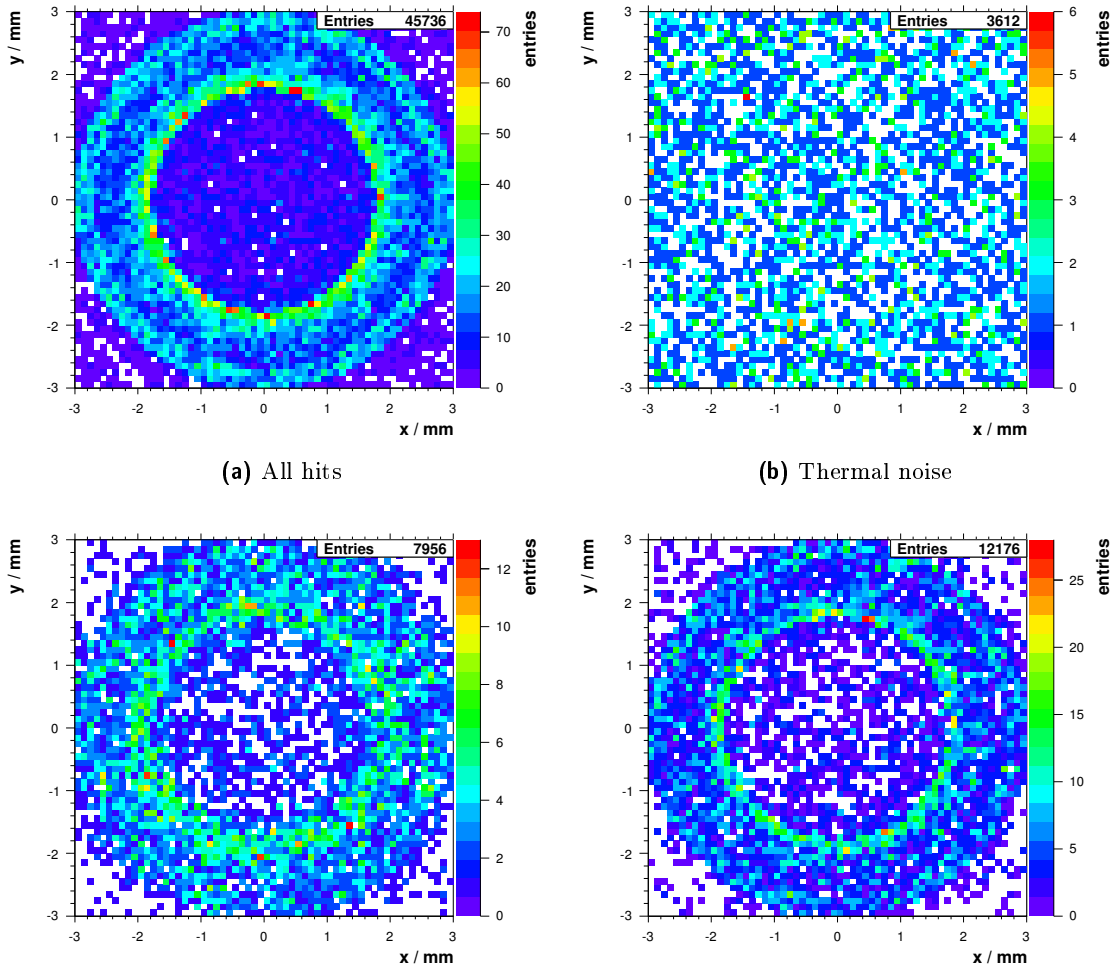

(a) All hits

(b) Thermal noise

(c) Cross-talk

(d) After-pulses

Figure 4.3.4.: Hits distribution on SiPM surface. Each bin represents an individual cell. The histograms count (a) all, (b) thermal noise, (c) cross-talk and (d) after-pulse hits of the simulation. The photon flux for this non-inclined photon beam onto the Winston cone is $\phi = 1\,\mathrm{ns}^{-1}$ in a time interval of $t \in (0, 100)\ \mu\mathrm{s}$.

ciency of each point in this parameter space is plotted in figure 4.3.5. These plots are normalised to the highest entry in the histogram. Since the data also contain the transmission efficiency of the Winston cone, the signal efficiency gets re-weighted by the inverse of the transmission efficiency to reveal deviations due to the response pattern of the SiPM. A decrease in efficiency for inclined light $\theta_{\mathrm{in}} > 20\,^\circ$ up to $20\,\%$ becomes apparent.

The impact of the Winston cone transmission properties on the SiPM operation is quite large. Only approximately 22% of the incoming light is detectable by such a pixel. This reduction has to be considered when the efforts of building up a camera formed by these pixels and the embedding into a complete telescope design are discussed in the next chapter.

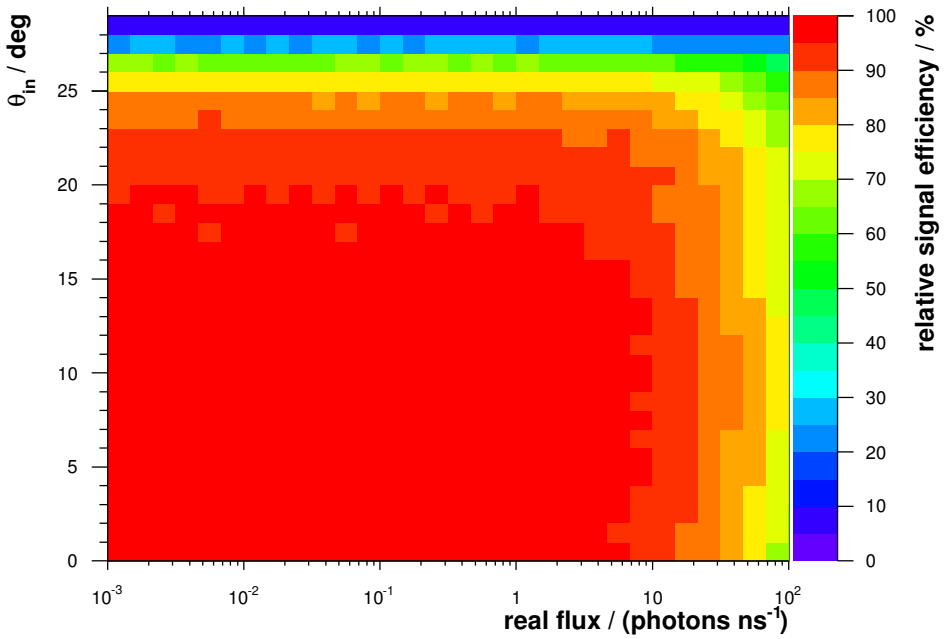

(a) Signal efficiency showing both Winston cone and SiPM limitations.

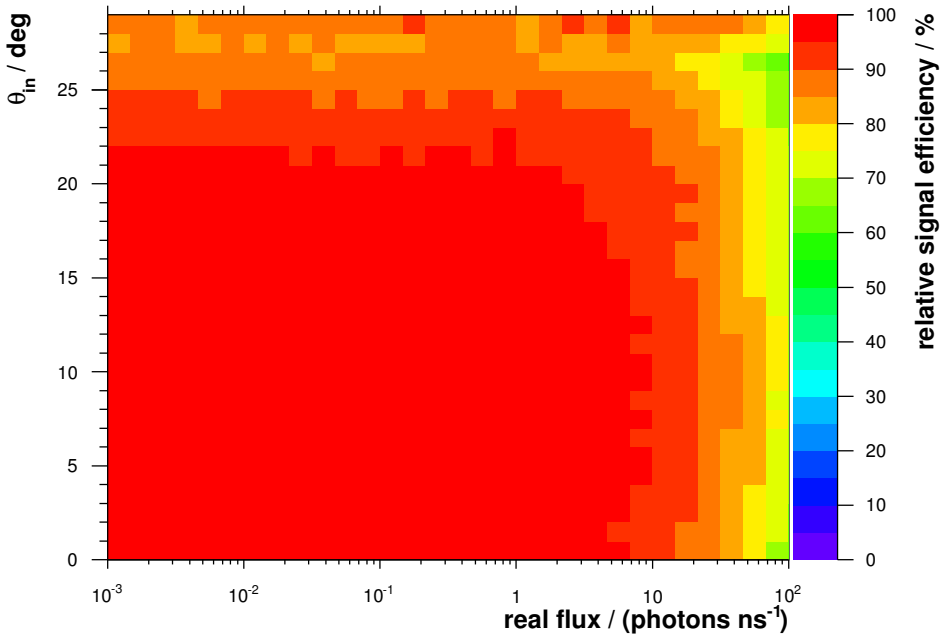

(b) Signal efficiency whereas the transmission efficiency of the Winston cone was unfolded from the data. The effects of the SiPM operation are revealed.

Figure 4.3.5.: Signal efficiency (fraction of simulated to detected photons) of a Winston cone in combination with an SiPM. The x-axis denotes different simulated light fluxes entering the Winston cone, the y-axis the incident angle θ_{in} of the beam and the color-coded z-axis the signal efficiency normalised to the highest entry in the histogram.

Chapter 5.

Telescope Design

The choice on the optical design for the fluorescence light telescope *FAMOUS* is very essential. It defines the field of view, the resolution power and the signal sensitivity. Furthermore, it should overcome a maximum of known optical aberrations so the produced image is as sharp and homogeneous as necessary. The design process takes reflecting as well as refracting designs into consideration.

5.1. Design Parameters

The first step is the definition of functional requirements which will set hard restrictions on the optical system. As discussed in the previous chapters, the camera of the telescope will hold pixels which are formed by the combination of a Winston cone light concentrator and an SiPM. All important quantities for the following considerations are enlisted in table 5.1.1 and are illustrated in figure 5.1.1. The number of pixels is the only quantity which will be fixed from the beginning to $n_{\mathrm{px}} = 64$ since *FAMOUS* is meant to be a prototype fluorescence telescope.

The number of pixels in one dimension $\sqrt{n_{\mathrm{px}}}$ and the upper radius r_1 of the light concentrator fixes the radius of the focal plane to

$$r_{\mathrm{fp}} = \sqrt{n_{\mathrm{px}}} \cdot r_1 \tag{5.1.1}$$

In combination with the total field of view α_{fov} of the telescope, the focal length can be defined as

$$f = \frac{r_{\mathrm{fp}}}{\tan\left(\alpha_{\mathrm{fov}}/2\right)} \quad . \tag{5.1.2}$$

Telescopes are often classified by their focal number $N_{\mathrm{f}} = f/D$[1]. A focal number $N_{\mathrm{f}} < 1$ will result in a focal length smaller than the aperture diameter. Thus, the optics are required to have a great focusing power. For an incidence of $\theta_{\mathrm{in}} = 0\,^{\circ}$, the focused light beam will have an incident angle of

$$\tan\beta = \frac{D/2}{f} = \frac{1}{2 \cdot N_{\mathrm{f}}} \tag{5.1.3}$$

on the focal plane. This must not exceed the maximum allowed incident angle of the Winston cone

$$\tan\beta \leq \tan\theta_{\mathrm{max}} \quad . \tag{5.1.4}$$

[1] Also called focal ratio.

Number of pixels	n_{px}	$8 \times 8 = 64$, hexagonal packaging
Aperture	D	
Focal ratio	N_{f}	
Winston cone radii	r_1, r_2	
Number of SiPM cells	n_{cell}	
Pixel field of view	α_{px}	1.5 °, same as the Auger FD telescopes
Total field of view	α_{fov}	

Table 5.1.1.: Telescope design parameters

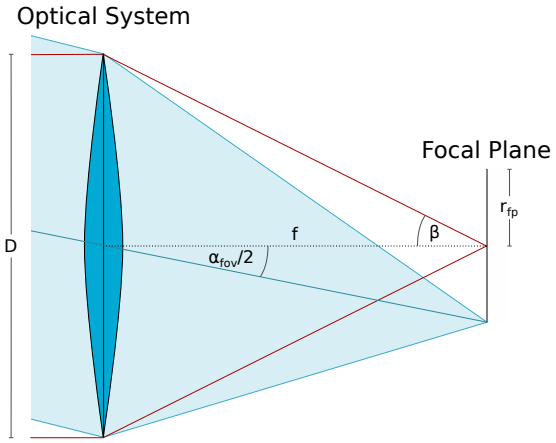

Figure 5.1.1.: Schematic of a generic optical system

Putting these equations together, the aperture diameter D of the telescope can be expressed by means of all other parameters

$$D = \frac{2 \cdot r_{\mathrm{fp}} \tan\beta}{\tan(\alpha_{\mathrm{fov}}/2)} \tag{5.1.5}$$

$$\leq 2 \cdot \sqrt{n_{\mathrm{px}}} \cdot r_1 \frac{\tan\theta_{\max}}{\tan(\alpha_{\mathrm{fov}}/2)} \quad . \tag{5.1.6}$$

This relation between the parameters will later be used to test several telescope versions for their estimated response.

5.1.1. Intensity of Fluorescence Light

A refined approach to describe the deposit of the fluorescence light of extensive air showers is the usage of radiometric quantities. The area of the telescope aperture A and the extents of the source region of the fluorescence light are very small in comparison to their distance R_{p} of at least one kilometer. This legalises the usage of the "10 times law" [29] and the size of the signal region can be neglected (see figure 5.1.2). Speaking in terms of radiometry the shower is the sender and the telescope the receiver.

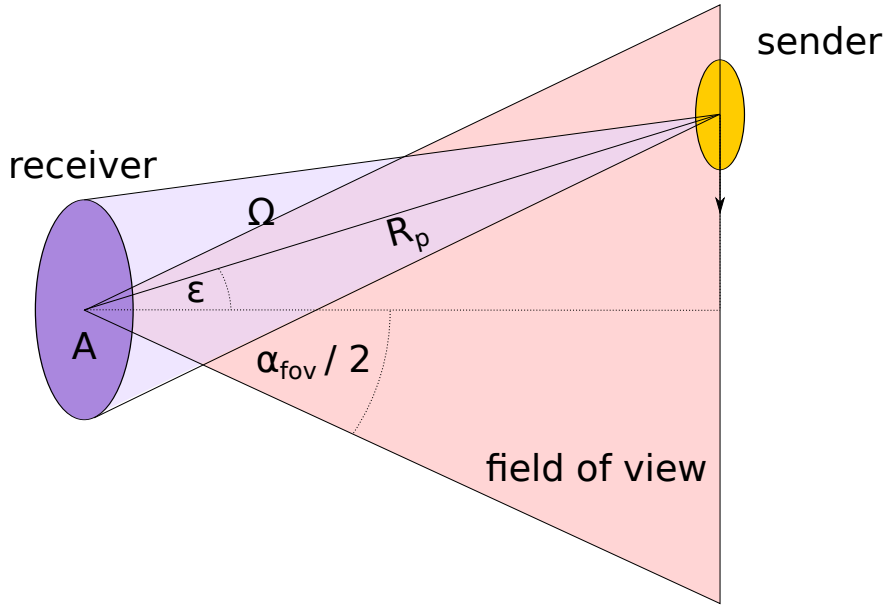

Figure 5.1.2.: Illustration of the "10-times law". The extend of the sender is negligible in comparison to its distance to the receiver.

The light emitting region of an extensive air shower passes analogue to the avalanche of the secondary particles through the atmosphere of the Earth. It radiates fluorescence photons isotropically into all directions. The intensity I_0 of the source region is the number of photons emitted per second and solid angle in units of

$$[I_0] = \mathrm{s}^{-1}\,\mathrm{sr}^{-1} \quad . \tag{5.1.7}$$

Due to the large shower distance R_p, the intensity of the fluorescence light source has to be corrected for Rayleigh attenuation [33]. The attenuation coefficient for the mean fluorescence light wavelength $\lambda = 350\,\mathrm{nm}$ is

$$\alpha = 7.45 \cdot 10^{-2}\,\mathrm{km}^{-1} \quad . \tag{5.1.8}$$

Similarly to the Beer-Lambert law, the intensity of the attenuated light after a travelled path R_p can be calculated by

$$I(R_\mathrm{p}) = I_0 e^{-\alpha R_\mathrm{p}} \quad . \tag{5.1.9}$$

Depending on the position of the receiver relative to the source region, the telescope can only collect a part of the emitted light which is defined by the solid angle

$$\Omega = \frac{A_\perp}{R_\mathrm{p}^2} = \frac{A\cos\epsilon}{R_\mathrm{p}^2} \tag{5.1.10}$$

with the area A of the aperture of the telescope, the angle ϵ between the surface normal of the aperture and the direction to the source region and the distance R_p [29]. Therefore, the received flux ϕ of the fluorescence light (number of photons per time) is

$$\phi = I \cdot \Omega = I_0 \frac{A\cos\epsilon}{R_\mathrm{p}^2} e^{-\alpha R_\mathrm{p}} \quad , \tag{5.1.11}$$

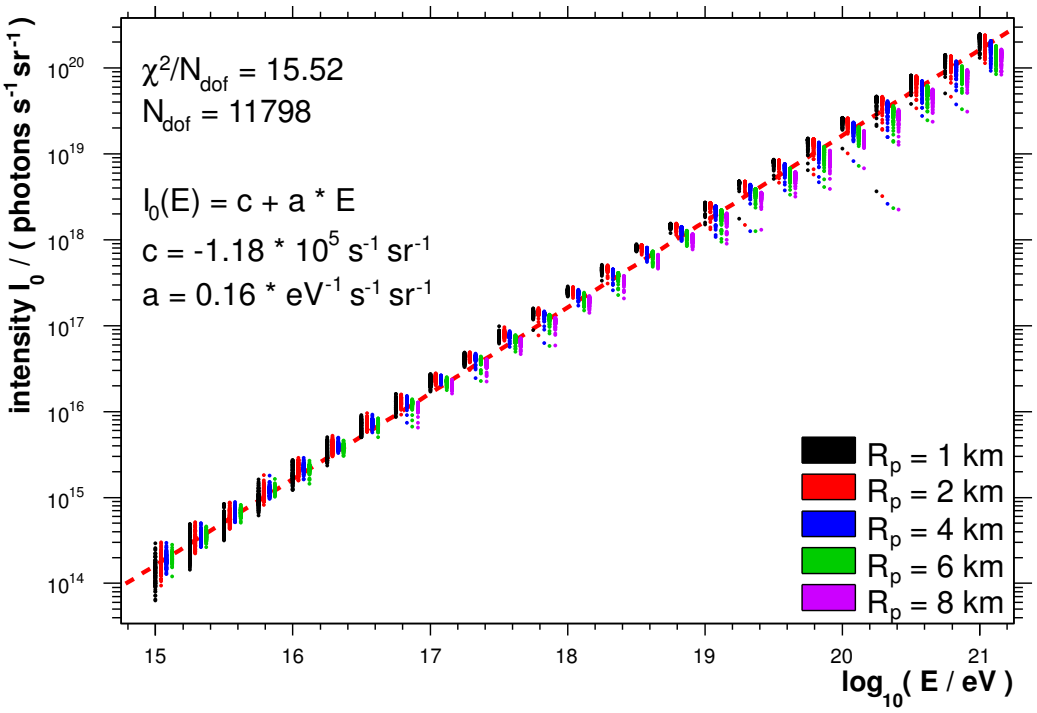

Figure 5.1.3.: Simulated intensity I_0 of the fluorescence light source region of extensive air showers versus shower energy for different distances R_p from the detector to the shower axis. The graphs have bins of $log_{10}(E/\mathrm{eV}) = 0.25$, whereas to increase readability, the individual graphs for the different distances to the telescope are shifted to the right. The data are a result of a *CONEX [30]* shower and *Auger Offline [31]* fluorescence light simulation with *EPOS [32]* as hadronic interaction model. The dashed line denotes a fit of the function stated in the upper left corner.

which is given in units of $[\phi] = \mathrm{s}^{-1}$. The minimum and the maximum of the viewing angle ϵ are defined by the field of view of the detector (see figure 5.1.2). The domain is

$$\epsilon \in [-\alpha_{\mathrm{fov}}/2, \alpha_{\mathrm{fov}}/2] \quad . \tag{5.1.12}$$

With the integral

$$\int_{-\alpha_{\mathrm{fov}}/2}^{\alpha_{\mathrm{fov}}/2} \cos\epsilon \, \mathrm{d}\epsilon = 2\sin\left(\alpha_{\mathrm{fov}}/2\right) \tag{5.1.13}$$

equation 5.1.11 can be written as

$$\phi = I_0 \frac{2A\sin\left(\alpha_{\mathrm{fov}}/2\right)}{R_{\mathrm{p}}^2} e^{-\alpha R_{\mathrm{p}}} \quad . \tag{5.1.14}$$

The *Auger Offline* software package of the Pierre Auger Collaboration [31] has been used to simulate the fluorescence light deposit of extensive air showers in a fluorescence telescope of the Pierre Auger Observatory. By the usage of equation 5.1.14, the results of the simulation on the number of photons arriving at the aperture have been transformed into the intensity I_0 as a function of the energy E of the primary particle and

N_f	D	α_px	SiPM size	E_noise	E_nsb	$E_\mathrm{saturation}$
1.00	255 mm	1.50 °	$3 \times 3\,\mathrm{mm}^2$	$6.0 \cdot 10^{18}$ eV	$4.2 \cdot 10^{19}$ eV	$2.7 \cdot 10^{22}$ eV
1.00	511 mm	1.50 °	$6 \times 6\,\mathrm{mm}^2$	$1.4 \cdot 10^{18}$ eV	$9.9 \cdot 10^{18}$ eV	$6.4 \cdot 10^{21}$ eV
0.75	549 mm	1.50 °	$6 \times 6\,\mathrm{mm}^2$	$1.0 \cdot 10^{18}$ eV	$8.5 \cdot 10^{18}$ eV	$4.7 \cdot 10^{21}$ eV
1.00	512 mm	0.75 °	$3 \times 3\,\mathrm{mm}^2$	$3.2 \cdot 10^{17}$ eV	$2.2 \cdot 10^{18}$ eV	$1.5 \cdot 10^{22}$ eV
1.00	1024 mm	0.75 °	$6 \times 6\,\mathrm{mm}^2$	$7.5 \cdot 10^{16}$ eV	$5.3 \cdot 10^{17}$ eV	$3.4 \cdot 10^{20}$ eV

Table 5.1.2.: Example cases for selected focal ratios, field of views and SiPM sizes. The cell pitch of the SiPM is $d_{pitch} = 100\,\mu$m.

the shower distance R_p. A fit of a simple straight line

$$I_0 = c + a \cdot E \tag{5.1.15}$$

to the simulated data is presented in figure 5.1.3. The intensities in the same energy bin but for various distances agree within 20 % which is sufficient for the following considerations.

5.1.2. Estimation of Detection Limits

The silicon photomultiplier sets the lower and upper boundaries to the detectable fluxes. The typical thermal noise rate $f_{th} = 10\,\mathrm{kHz\,cell}^{-1}$ multiplied by the number of cells gives a flux of

$$\phi_\mathrm{noise}^{(\mathrm{px})} \approx n_\mathrm{cell} \cdot f_\mathrm{th} = n_\mathrm{px} \left(\frac{2r_2}{d_\mathrm{pitch}}\right)^2 f_\mathrm{th} \quad . \tag{5.1.16}$$

Another noise source is the night-sky brightness with a upper limit on the radiance of

$$L_\mathrm{nsb} \lesssim 1.9 \cdot 10^{12}\,\mathrm{m}^{-2}\,\mathrm{s}^{-1}\,\mathrm{sr}^{-1} \tag{5.1.17}$$

in the ultraviolet regime $\lambda \in [300, 400]$ nm as it has been measured near Aachen in Eynatten, Belgium[2] [19]. The telescope spans a field of view cone with a solid angle of

$$\Omega_\mathrm{fov} = 2\pi\,(1 - \cos\,(\alpha_\mathrm{fov}/2)) \quad . \tag{5.1.18}$$

In conjunction with the aperture area $A = \pi(D/2)^2$, this results in a light flux per camera pixel of

$$\phi_\mathrm{nsb}^{(\mathrm{px})} = 2\pi\,(1 - \cos\,(\alpha_\mathrm{fov}/2))\,\frac{L_\mathrm{nsb}(D/2)^2}{n_\mathrm{px}} \quad . \tag{5.1.19}$$

The circular Winston cone obscures the outer areas of the SiPM. The amount of exposed cells is reduced to

$$n'_\mathrm{cell} = n_\mathrm{cell} \cdot \frac{\pi r_2^2}{(2r_2)^2} = n_\mathrm{cell}\frac{\pi}{4} \quad . \tag{5.1.20}$$

[2] June 1st, 2011, 01:14 h for a duration of 120 s.

As discussed in chapter 3, saturation effects become important when the light flux exceeds the amount of exposed cells n'_{cell} per recovery time t_{rec}:

$$\phi^{(\mathrm{px})}_{\mathrm{saturation}} = \frac{n'_{\mathrm{cell}}}{t_{\mathrm{rec}}} \quad . \tag{5.1.21}$$

A vertical shower might illuminate a mean number of pixels of $n^{(\mathrm{response})}_{\mathrm{px}} \approx 10$ in a straight line[3]. Consequently, the equivalent shower intensity is given by

$$I_{\mathrm{shower}} = n^{(\mathrm{response})}_{\mathrm{px}} \frac{\phi^{(\mathrm{px})}}{\Omega(d)} \quad . \tag{5.1.22}$$

Applying the fit result in figure 5.1.3

$$c = -1.18 \cdot 10^{-5}\,\mathrm{s}^{-1}\,\mathrm{sr}^{-1} \tag{5.1.23}$$
$$a = 0.16\,\mathrm{eV}^{-1}\,\mathrm{s}^{-1}\,\mathrm{sr}^{-1} \tag{5.1.24}$$

the light fluxes $\phi^{(\mathrm{px})}$ can be translated to a shower energy equivalent

$$E = \frac{I_0 - c}{a} \quad . \tag{5.1.25}$$

Table 5.1.2 shows results of some example cases for a set of selected focal ratios N_{f}, field of views α_{fov} and SiPM sizes. The diameter D of the aperture has the greatest influence on the detector response. The more light the telescope can collect, the more signal over noise the camera can output. An increase in photon count rates can be more efficiently detected by an SiPM possessing more cells. The focal ratio shows a minor influence on the parameters of the optical system because of their strong relation to each other. While decreasing the field of view of a pixel α_{px}, the high night-sky photon flux contributes less and therefore the lower energy bound can be decreased. Simultaneously, this pushes the aperture diameter D. For the prototype it has been decided to favour the design with the following specifications

$$N_{\mathrm{f}} = 1,\ \alpha_{\mathrm{px}} = 1.5\,^{\circ},\ 6 \times 6\,\mathrm{mm}^2\ \mathrm{SiPM},\ d_{\mathrm{pitch}} = 100\,\mu\mathrm{m},\ f = D = 511\,\mathrm{mm} \tag{5.1.26}$$

as stated in line 2 of table 5.1.2. The following section will evaluate common telescope designs with one or more active mirrors and tries to match those with the predetermined specifications.

5.2. Reflecting Telescopes

Reflecting telescopes utilize one ore more mirrors for the optical magnification of distant objects. It has to be distinguished between active and passive mirrors. The latter is only planar and often used to direct the light beam out of the telescope to an eye-piece.

[3] Figure 5.3.2 visualizes the hexagonal arrangement of the single pixels.

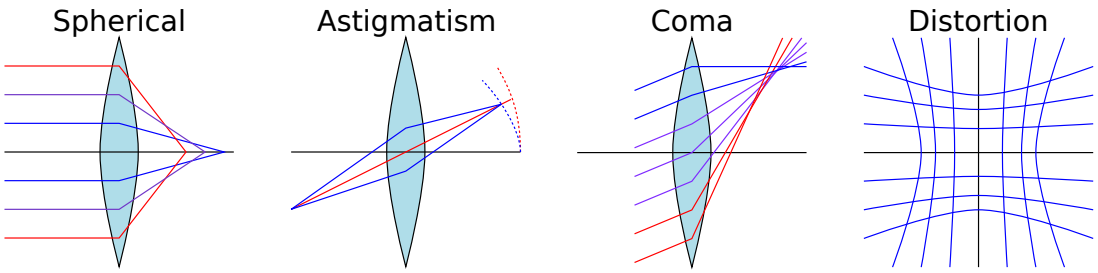

Figure 5.2.1.: Schematic of most prominent optical aberrations. Distortion, coma and spherical aberration occur for broad, astigmatism also for narrow beams.

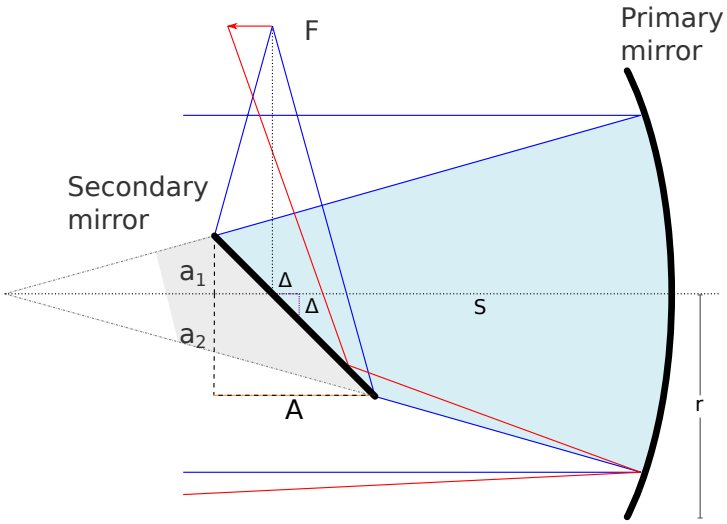

Figure 5.2.2.: Optical design of a Newton reflector. The incoming light beam is reflected back by the primary mirror in a cone like pattern. The cone is deflected by the intersecting, secondary planar mirror by $90\,^\circ$ and thus out of the path of rays.

The active mirrors in the system are responsible for the imaging and also introduce various aberrations.

The four most prominent aberrations in telescope systems are spherical aberration, astigmatism, coma and distortion, which are sketched in figure 5.2.1 [29]. In case of spherical aberration, the focal point of abaxial rays is closer to the lens. The astigmatism occurs for inclined beams where two perpendicular planes within the beam, the meridional and the tangential, are refracted to two different foci. The combination of spherical aberration and astigmatism creates the coma. Finally, whenever different object heights are not proportionally reproduced in the image plane, a distortion becomes apparent.

5.2.1. Newton Reflector

The Newton reflector houses a parabolic mirror. Incoming, parallel light is focused to the focal point of the parabola. The resulting light cone is intersected by a planar

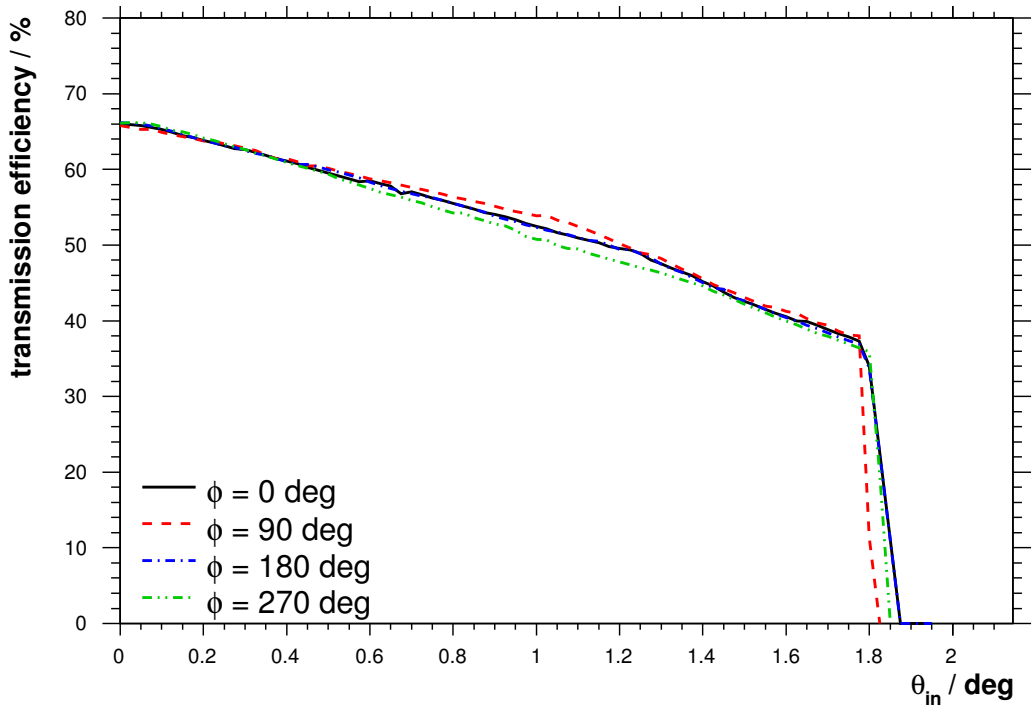

Figure 5.2.3.: Field of view of the commercial Meade Bresser-PN203 Newton reflector. The transmission efficiency is plotted versus the incident angle of the parallel light beam. The different lines denote the different polar angles ϕ of the incoming beam. The data have been obtained from a *Geant4* simulation.

mirror of elliptic shape which lies between the original focal point and the parabolic mirror. Thus, the cone is deflected by 90° out of the incoming ray path and to the observer. A schematic is shown in figure 5.2.2. Since it is a conic section, the secondary mirror is not exactly centered on the optical axis but shifted by the distance

$$\Delta = \frac{A}{2} + a_1 \tag{5.2.1}$$

whereas the extents of the obstruction of the primary mirror are given by

$$A = a_1 + a_2 \tag{5.2.2}$$

$$a_1 = \frac{(f-s)r}{f+r} \quad , \quad a_2 = \frac{(f-s)r}{f-r} \tag{5.2.3}$$

with the radius r of the parabolic mirror and the focal length f [34]. The position s of the secondary mirror is defined by

$$s = \frac{f \cdot A}{r}\left(\frac{1}{f+r} + \frac{1}{f-r}\right)^{-1} \quad . \tag{5.2.4}$$

The big and small half axes a and b of the ellipse defining the shape are

$$a = \frac{A}{\sqrt{2}} \tag{5.2.5}$$

$$b = \sqrt{[(f-s+\Delta)\tan(45\,°)]^2 - \Delta^2} \quad . \tag{5.2.6}$$

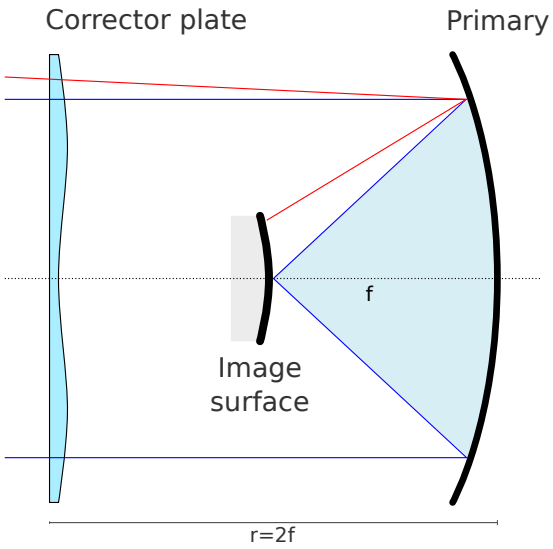

Figure 5.2.4.: Schmidt camera optics. The incoming light beam is deformed by the corrector plate in such a manner that optical aberrations introduced by the primary mirror are automatically compensated. The primary mirror deflects the light onto a curved image surface.

Possible aberrations of a Newton reflector are spherical and off-axis coma. Astigmatism is less dominant [34].

A trade-off of this design is the obstruction by the secondary mirror. A reduction of the focal number $N_\mathrm{f} = f/D = f/(2r)$ shifts the focal point towards the primary mirror. At the same time, the secondary mirror also has to be situated closer to the primary and larger to collect the whole reflected light cone (see equations 5.2.3 - 5.2.6). This results in a bigger obstruction and less light grasp. Commercial telescopes usually have $N_\mathrm{f} \geq 4$ whereas greater values of N_f are preferred for better angular resolution. The Newton reflector is not meant to be a wide angle telescope.

First test measurements using just one camera pixel, consisting of a Winston cone and an SiPM, have been made involving the commercial Newton reflector "Meade Bresser-PN203" with a focal number of $N_\mathrm{f} = 4$ and $D = 2r = 203\,\mathrm{mm}$ [19]. A *Geant4* simulation reproducing the exact parameters of the reflector reveals that the transmission efficiency to the focuser tube (see figure 5.2.3) shows a decrease with increasing field angles until it drops to zero at $\theta_\mathrm{in} \approx 1.8\,^\circ$. The *Geant4* results have been used to determine the upper limit on the night-sky brightness near Aachen (see section 5.1.2) and therefore the major part of the expected noise level for measurements of extensive air showers. The limited field of view and the big focal ratio discard the Newton reflector for the design of *FAMOUS*.

5.2.2. Schmidt Camera

The Schmidt camera is a wide field of view telescope and is the archetype of the telescopes of the current fluorescence detector of the Pierre Auger Observatory [13]. A schematic can be found in figure 5.2.4. It has one active, parabolic mirror which is used

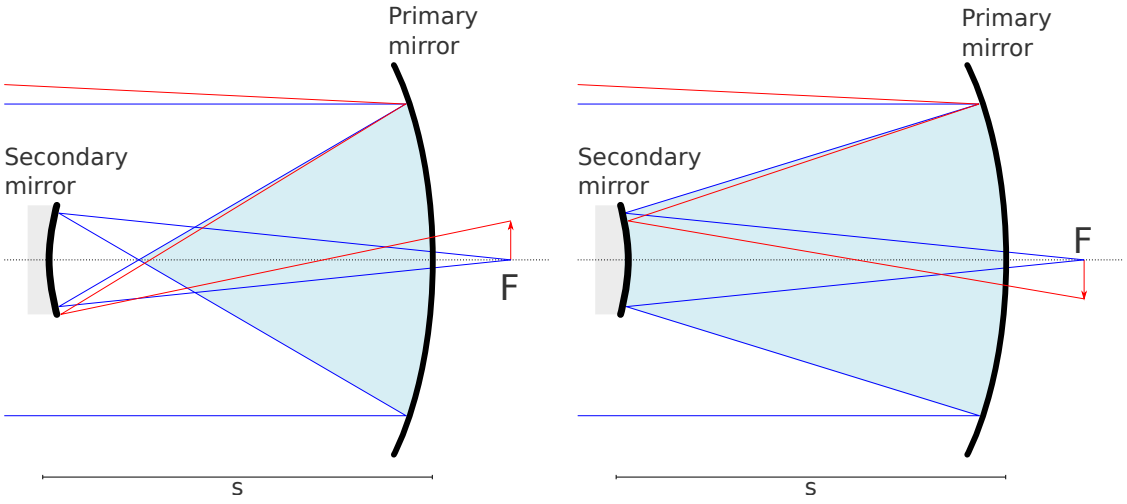

(a) Gregorian **(b)** Cassegrain

Figure 5.2.5.: Cassegrain- and Gregorian-telescope optics. The only difference is the concavity of the secondary mirror which causes f_2 to be either negative or positive. The primary mirror reflects the incoming light beam to a secondary, parabolic mirror. The reflected light cone can pass the primary mirror through a hole and can be detected outside the light path.

to focus the incoming light onto a camera which is positioned at the focal point of the parabola [34]. Since the plane of the focus changes with the field angle of the incoming light beam, the image surface has to be curved. In combination with a corrector lens, this system is nearly completely free of the four primary aberrations.

Event though a Schmidt camera can be made with $N_\mathrm{f} \lesssim 1$ and has a big angular acceptance, the image surface is in the light path. Thus, the design has also to be rejected for the telescope prototype. However, the great imaging properties qualify it for a successor of *FAMOUS*.

5.2.3. Cassegrain and Gregorian Telescopes

In order to keep the focal surface out of the light path, a second active mirror has to be introduced. Two common telescope optics using an active secondary mirror are the Cassegrain and the Gregorian. Figure 5.2.5 shows a schematic of both designs. The focal length for a two mirror telescope is given by

$$f = \frac{f_1 f_2}{f_1 - f_2 - s} \quad , \tag{5.2.7}$$

with s and f_1 negative whereby $f_2 < 0$ for Cassegrain and $f_2 > 0$ for Gregorian arrangement. The parameter s is the distance between the two mirrors. The total focal length f is positive for the Cassegrain and negative for the Gregorian telescope. This construction mainly suffers from coma [34].

Equation 5.2.7 shows that it is not possible to have a reasonable system with a focal ratio $N_\mathrm{f} < 1$. This disqualifies two-mirror-telescope-designs. Three or even more mirrors provide also no practical solutions. Not only every new optical element introduces

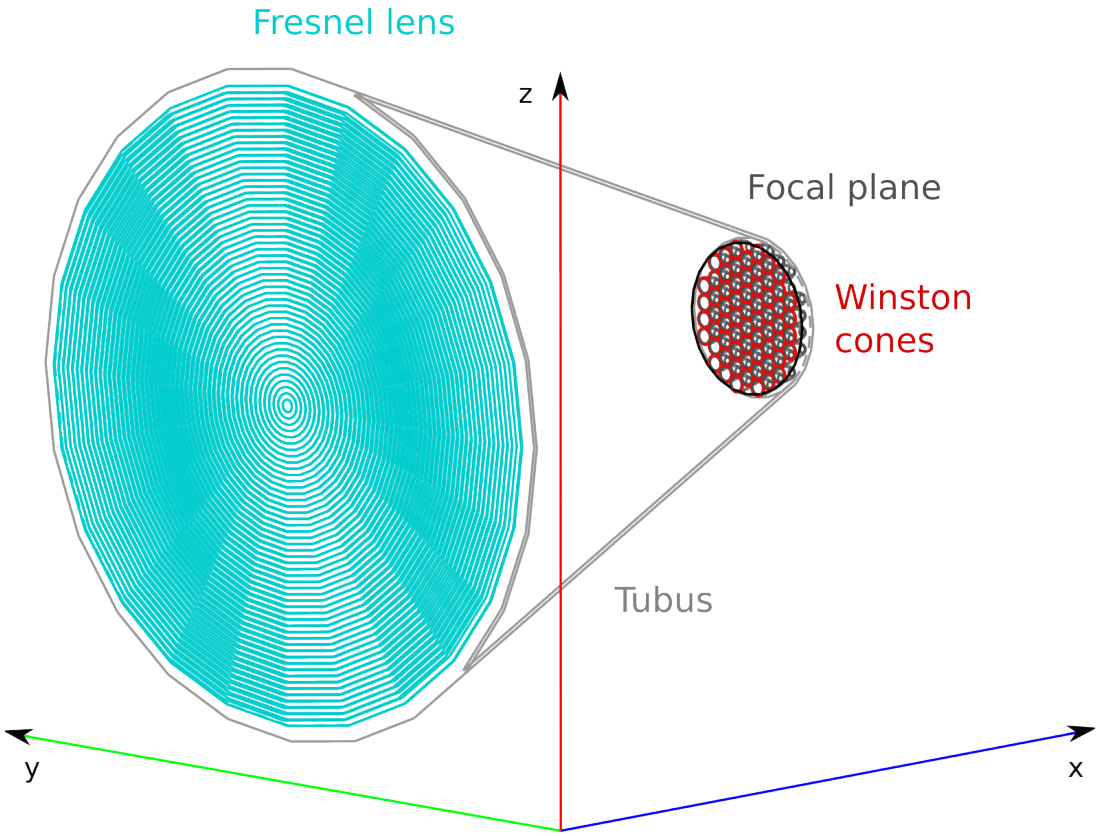

Figure 5.3.1.: The optical design of *FAMOUS*. Screen of the *Geant4* simulation visualization. The number of gratings of the Fresnel lens has been reduced in this drawing by a factor of 10 for increase of visibility.

additional light losses but also each mirror contributes to the total focal length and thus might increase the focal ratio N_f.

5.3. Refracting Design

Summarising all restrictions on the design there are three fundamental components:

1. The focal plane has to be placed outside of the path of rays which requires a reflecting telescope to have at least two mirrors and therefore has obstructions on the primary mirror.

2. The small light fluxes not only require the SiPMs to have a PDE which is at least compatible with the one of standard PMTs, but also require a big aperture of the system. In combination with the small form factor of the focal plane, it is clear that the focal ratio N_f has to be less or equal to one.

3. The size of the focal plane can be increased by using light concentrators. Although Winston cones reach out to the theoretically best achievable light concentrator beyond the potential of condenser based optics, there are strong limits on the angular acceptance.

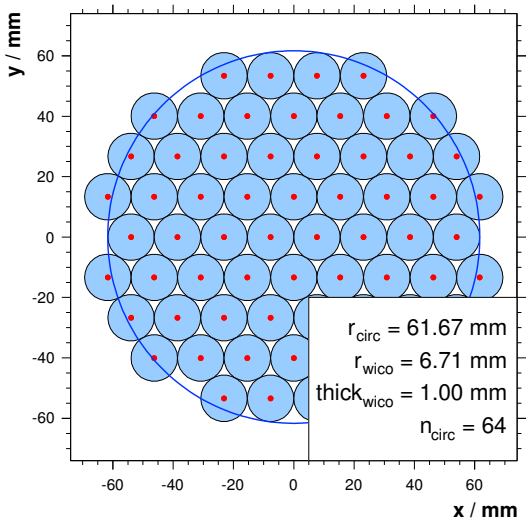

Figure 5.3.2.: Hexagonal packaging of pixels. Every black circle equates a Winston cone. The red dots mark the center.

Switching from reflective to refractive optics, it is clear that a simple refractive design involving only one big lens can fulfil all functional requirements defined in section 5.1.2. Possible aberrations of lenses with high refraction power are spherical and chromatic aberration [29]. The first can be overcome by designing an aspheric lens profile. The latter is of minor importance since the wavelength range of the fluorescence light signal is very narrow. On the other hand, high transparency in the ultraviolet light regime is not widely implemented and has to be ensured by careful choice of the lens material.

The concept of a Fresnel lens promises to have a high refraction power paired with small thickness and less absorption compared to a conventional lens. This also makes $N_\mathrm{f} \leq 1$ feasible. The next chapter will present all features and drawbacks of this kind of lenses.

The optical design of *FAMOUS* is pictured in figure 5.3.1 as it has been implemented in a fully capable *Geant4* simulation. The aperture is spanned by the big Fresnel lens in the front. A hexagonal arrangement of $n_\mathrm{px} = 64$ Winston cones defines the focal plane of the telescope and ensures a fill factor of approximately 91 %. A frontal view onto the focal plane is given in figure 5.3.2. Because of manufacturing concerns, the Winston cones need to have a wall thickness of at least 1 mm. This introduces 2 mm thick dead space encircling each pixel which could be compensated by a "Mercedes-star" like structure as used in the telescopes of the fluorescence detector of the Pierre Auger Observatory [13].

Chapter 6.

Fresnel Lens

The concept of a Fresnel lens has been developed by the French physicist Augustin Jean Fesnel in 1822. Originally, the Fresnel lens has been intended for usage in light houses as a cost efficient and effective replacement for mirrors [35].

Applying the Fresnel lens concept, the amount of bulk material is reduced by dividing the lens into concentric annular sections, also called "grooves" (see figure 6.0.1). The thickness of each section is decreased to a minimum while accepting discontinuities between the single sections. A further simplification is achieved by the approximation of the curvature of a groove by a linear slope. Due to the simplification and the discontinuities of the lens surface, Fresnel lenses can not be used in precise imaging applications e.g. photography. It has to be proven whether the imaging quality will be sufficient for the application in the refractive optical design of the fluorescence light telescope.

6.1. Construction

The lens surface of a bulky lens is parametrised according to the sagitta function $f(s)$ for an aspheric even surface

$$f(s) = \frac{c \cdot s^2}{1 + \sqrt{1 - (k+1) \cdot c^2 s^2}} + \sum_{i=1}^{O} A_{2i} s^{2i} \tag{6.1.1}$$

with a given distance s to the center of the lens [36]. The first term is a circle for a conic constant of $k = 0$, a parabola for $k = -1$ or a hyperbola $k < -1$. The curvature c is the inverse of the bending radius R of the lens surface. Some example cases can be found in figure 6.1.1.

Aspheric surfaces can be realised by setting the constants $A_i \neq 0$ up to the order O. This adds a polynomial to the first term in equation 6.1.1 which introduces deviations to the ideal circular, parabolic or hyperbolic surface. Therefore, the collection of abaxial rays may be improved. Although the A_i might be very small (in the order of 10^{-4} –

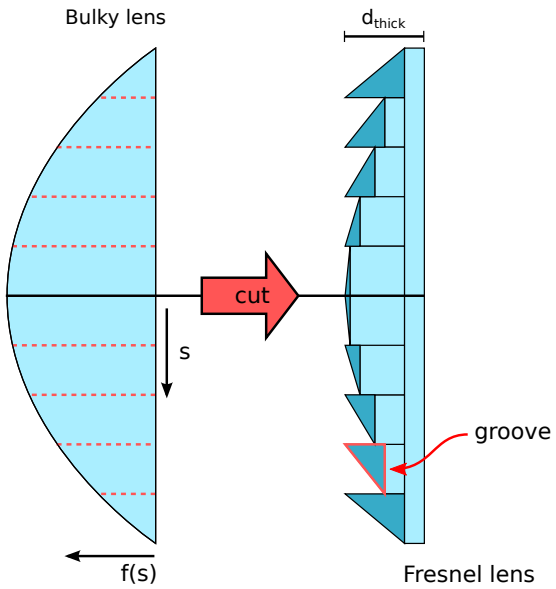

Figure 6.0.1.: Fresnel lens construction principle. The bulky lens is divided into annular concentric sections (also named "grooves") whose thicknesses are reduced to a minimum.

10^{-10}), their influence on the slope of the surface is not negligible since the constants are multiplied by the distance to the lens center s to some high power. The unit is $[A_i] = \mathrm{m}^{1-i}$.

The next step is the division of the lens into concentric annular grooves of equal width as depicted in figure 6.0.1. The slope of each groove still follows equation 6.1.1. All grooves may be situated onto a common base plate. The height of the highest groove plus the thickness of the base define the thickness d_{thick} of the Fresnel lens.

In general, the more grooves per millimeter are situated on a lens, the better the image quality should get because of the improved approximation of the original curved surface. However, the increased amount of discontinuities on the lens surface reduces the overall light transmission efficiency as presented in figure 6.1.2. A small incident angle dependency of the transmission efficiency of the Fresnel lens is apparent.

In the following sections results of a ray-tracing simulation with *Geant4* will be presented which have been obtained for a lens with diameter $D = 511\,\mathrm{mm}$, focal length $f = D$, conic constant $k = -1$ and thickness $d_{\mathrm{thick}} = 2.5\,\mathrm{mm}$. The material has been simulated to be UV-transparent acrylic. A plot of the transmission curve dependent on the wavelength can be found in the appendix and has been taken into account for respecting the bulk absorption. The simulation is based upon the example "air_shower" delivered with *Geant4* which features a static implementation of a Fresnel lens and has been programmed by B. Tomé [37].

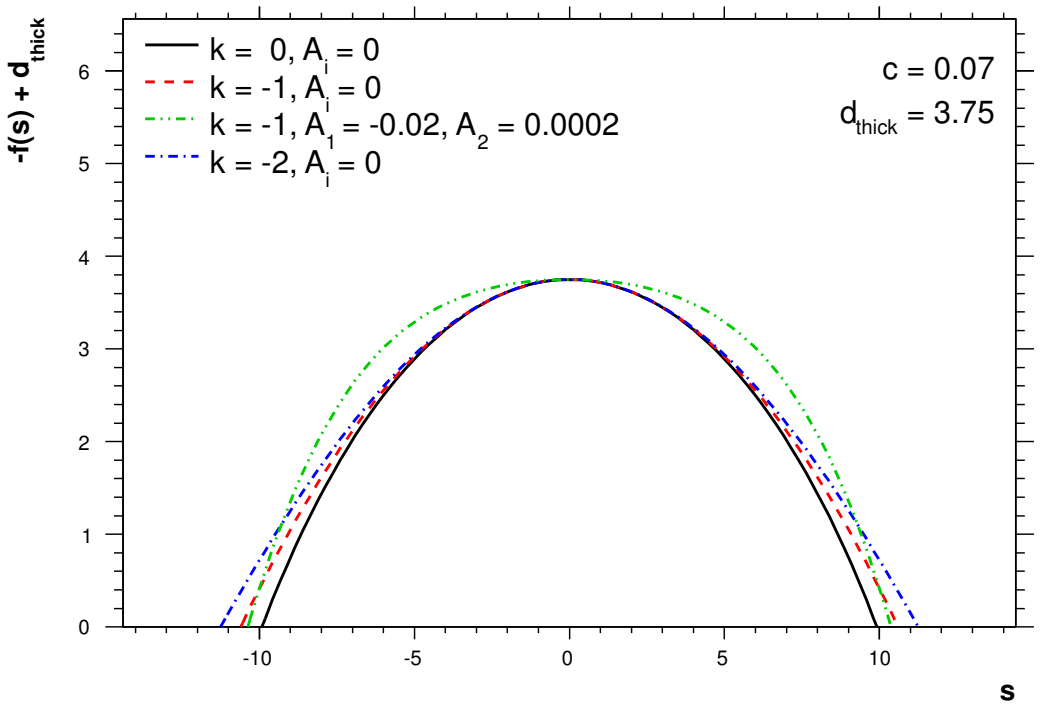

Figure 6.1.1.: Example cases of the Fresnel lens surface parametrisation. The x-axis denotes the radial distance s from the lens center in arbitrary units. The different curves state the surface paramterization $f(s)$ (see equation 6.1.1) for different conic constants k and aspheric constants A_i. Note the different scales of the abscissa and the ordinate.

6.2. Point Spread Function

A convenient quantity for the evaluation of the performance of an imaging optical system is the point spread function. It describes the depiction of an infinite distant point-like source object on the image plane. All variations in the optimal transmission through the system are revealed.

6.2.1. The Airy Pattern

The optimal shape can be obtained from the Airy pattern named after the British astronomer George Biddell Airy [38]. The pattern occurs on the image plane if a light beam of an infinitely distant point source gets directed through a circular aperture. The intensity distribution on the image plane can be expressed by the Fraunhofer diffraction

$$I(x) = I_0 \left(2\frac{J_1(x)}{x} \right)^2 \tag{6.2.1}$$

whereas $J_1(x)$ is the first kind Bessel function of the order of 1 and x a dimensionless parameter given by

$$x = \frac{\pi D}{\lambda} \sin\theta \tag{6.2.2}$$

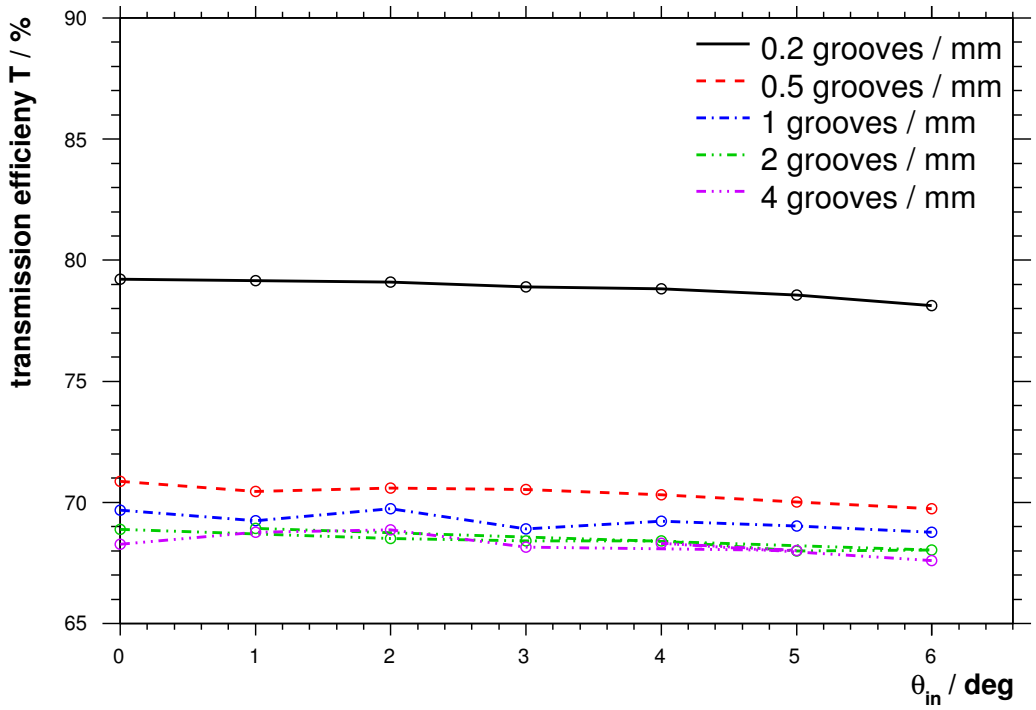

Figure 6.1.2.: Transmission efficiency of the Fresnel lens as a function of the incident angle. Bulk absorption has been respected. The differently coloured curves denote different number of grooves.

with the aperture diameter D, the wavelength of the light λ and the incident angle of the rays on the image plane θ. The limit $x \to 0$ results in $I(0) = I_0$ which is the maximum intensity. Though the usage of x appears to be inconvenient, it allows the calculation of some parameters independently from the actual geometry of the system. The first zeros of $I(x)$ are at $x_0 = \{1.22\pi, 2.23\pi, 3.24\pi, ...\}$. For small θ , x can be expressed by the radial distance r to the center of the focal plane

$$x \approx \frac{\pi D}{\lambda} \cdot \frac{r}{f} = \frac{\pi}{\lambda N_\mathrm{f}} r \tag{6.2.3}$$

with the focal ratio N_f. The integral of the intensity is equal to the in x encircled energy

$$P(x) = P_0 \left(1 - J_0^2(x) - J_1^2(x)\right) \tag{6.2.4}$$

where $J_0(x)$ is the first kind Bessel function of the order of 0 and the normalisation constant

$$P_0 = \frac{f^2 \lambda^2}{A} I_0 \tag{6.2.5}$$

with the aperture area A and the focal length $f = N_\mathrm{f} \cdot D$.

The purpose of this exercise is to demonstrate the extents of a flawless point spread function. In case of the beforehand presented telescope design with $D = 511\,\mathrm{mm}$, $N_\mathrm{f} = 1$ and a mean wavelength of the fluorescence light spectrum of $\lambda = 350\,\mathrm{nm}$, the first zero of the intensity distribution can be found at a radial distance $r \approx 1.22\lambda N_\mathrm{f} = 0.43\,\mu\mathrm{m}$ to the center of the picture. In figure 6.2.1 both, the intensity distribution and

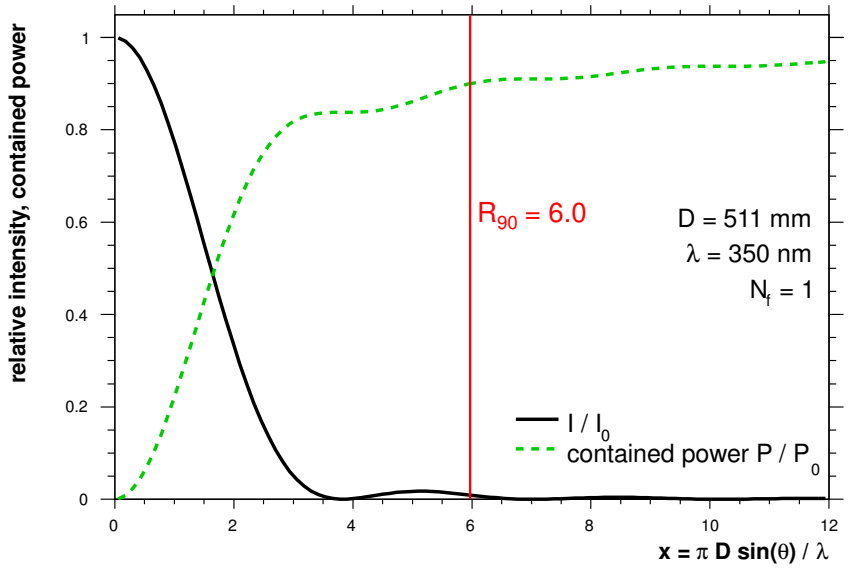

(a) Intensity on the image plane as function of $x = \frac{\pi D}{\lambda} \sin\theta$. The integrated encircled energy is plotted as a dashed line.

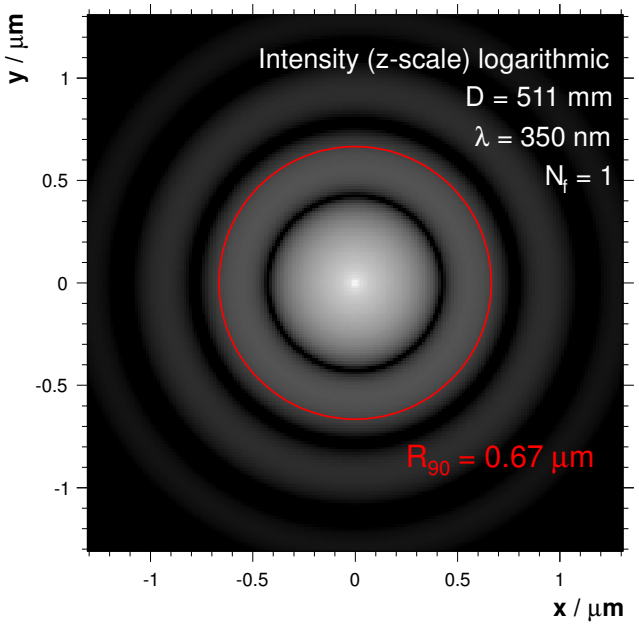

(b) Diffraction pattern on the image plane. The color code denotes the intensity which is plotted logarithmically.

Figure 6.2.1.: Airy pattern on the image plane for a circular aperture with diameter D, focal ratio N_f and wavelength of the light λ. The red line resp. circle marks the aberration radius R_{90} of 90 % encircled energy.

the encircled energy within a certain x are shown for this example case. At a radial distance $x = 6$ to the center of the image, 90 % of the total energy is encircled. This radius is referred to as R_{90} and is a sensitive measure to the image quality.

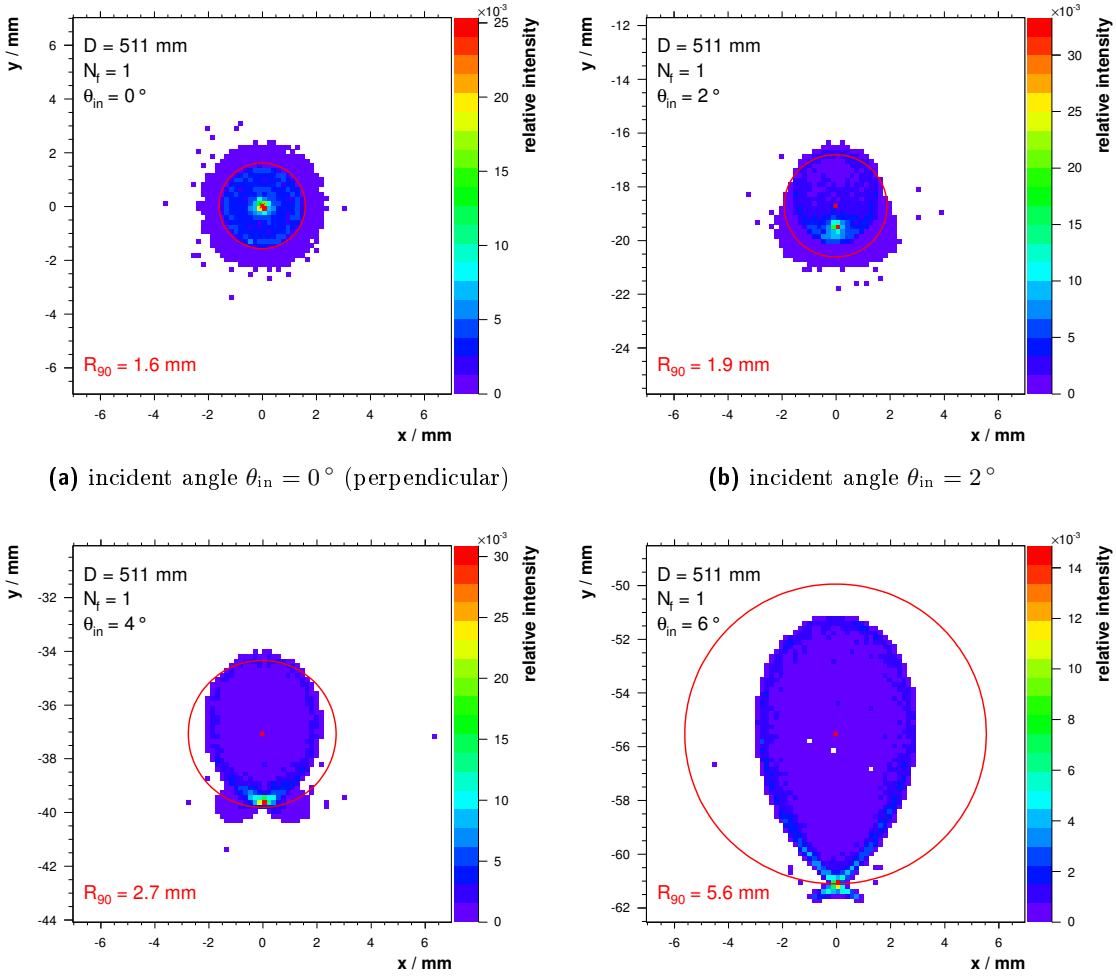

(a) incident angle $\theta_{\text{in}} = 0\,^\circ$ (perpendicular)

(b) incident angle $\theta_{\text{in}} = 2\,^\circ$

(c) incident angle $\theta_{\text{in}} = 4\,^\circ$

(d) incident angle $\theta_{\text{in}} = 6\,^\circ$

Figure 6.2.2.: Sampled point spread functions for different angles of incidence. The lens-to-image-plane-distance has been fixed to $z = 518.6\,\text{mm}$. The red circle denotes the aberration radius R_{90} of 90 % encircled energy.

6.2.2. Sampling the Point Spread Function

For more complex optical components such as the Fresnel lens, the analytical calculation of the point spread function is no longer trivial. With the help of the *Geant4* ray-tracing simulation, the image of an infinitely distant light source can be reproduced at the image plane. By sampling each point of the image plane, the point spread function can be obtained and investigated for the occurrence of optical aberrations.

The sampled point spread function derived from the *Geant4* simulation is shown in figure 6.2.2 for different incident angles θ_{in} on the lens surface. The distance between lens and image plane was set to $z = 518.6\,\text{mm}$ which corresponds to the minimal R_{90} for $\theta_{\text{in}} = 0\,^\circ$. Thus, the lens-to-image-plane-distance z has to be slightly greater than the analytical focal length f because of the imperfections of the lens.

For perpendicular incident light, the point spread is symmetric around the center. In

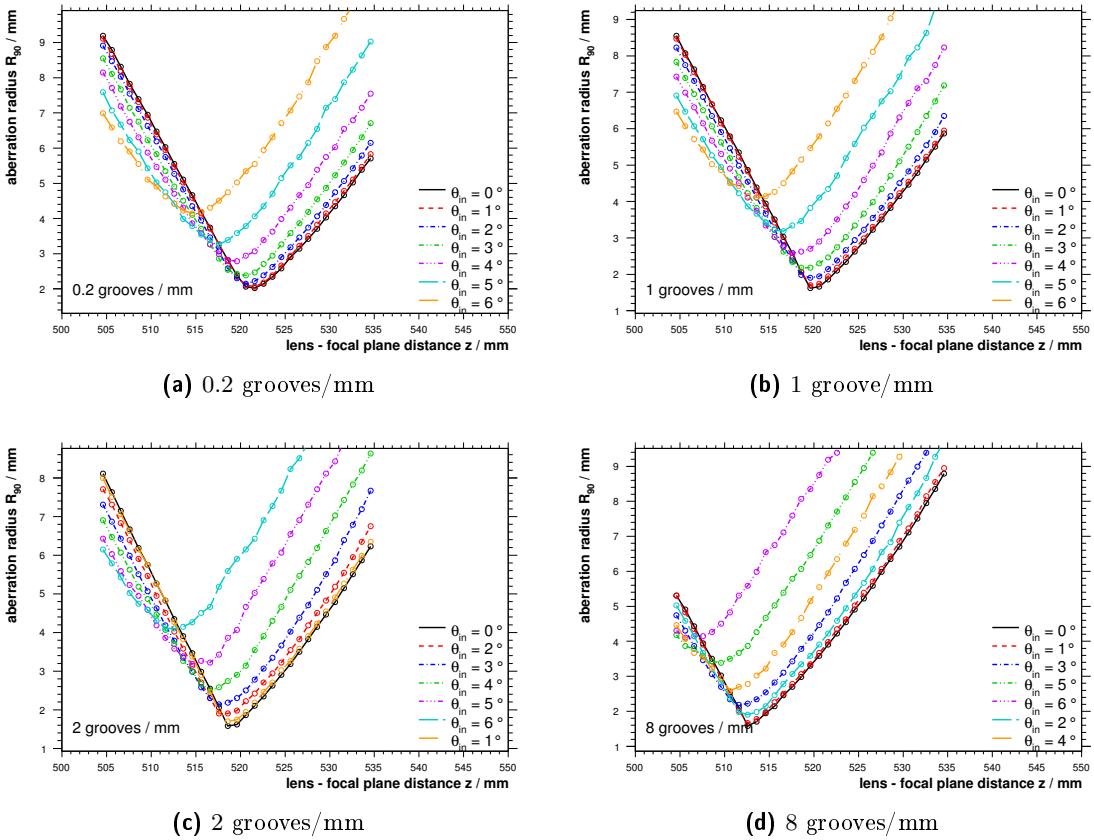

(a) 0.2 grooves/mm

(b) 1 groove/mm

(c) 2 grooves/mm

(d) 8 grooves/mm

Figure 6.3.1.: Aberration radius R_{90} for various number of grooves. Plotted as function of the lens-to-focal-plane-distance z. The different line styles denote different field angles.

comparison to the theoretical optimum $R_{90} = 0.67\,\mu\text{m}$ given by the Airy pattern, the simulated aberration radius $R_{90} = 1.6\,\text{mm}$ is very large. To produce a sharp image, the pixels[1] of the camera used in combination with this lens do not have to be smaller than R_{90}.

As discussed in chapter 5, the Winston cone, which defines the aperture of one camera pixel, has an entrance radius of $r_1 = 6.71\,\text{mm}$. This is also wide enough for more inclined light beams, e.g. for $\theta_{\text{in}} = 6\,^\circ$ resulting in $R_{90} = 5.6\,\text{mm}$. These inclined light beams introduce abnormalities to the point spread function due to spherical aberration.

6.3. Optimizations using the Aberration Radius R_{90}

As discussed in the previous section, the measure of R_{90} is a sensitive quality criterion since it is proportional to the size of the image of a point source. Besides the diameter D and the focal length f, which usually are fixed by the optical system, the only free parameter of the Fresnel lens is the amount of grooves per millimeter. Optimisations

[1] A pixel of *FAMOUS* is the combination of a Winston cone and an SiPM.

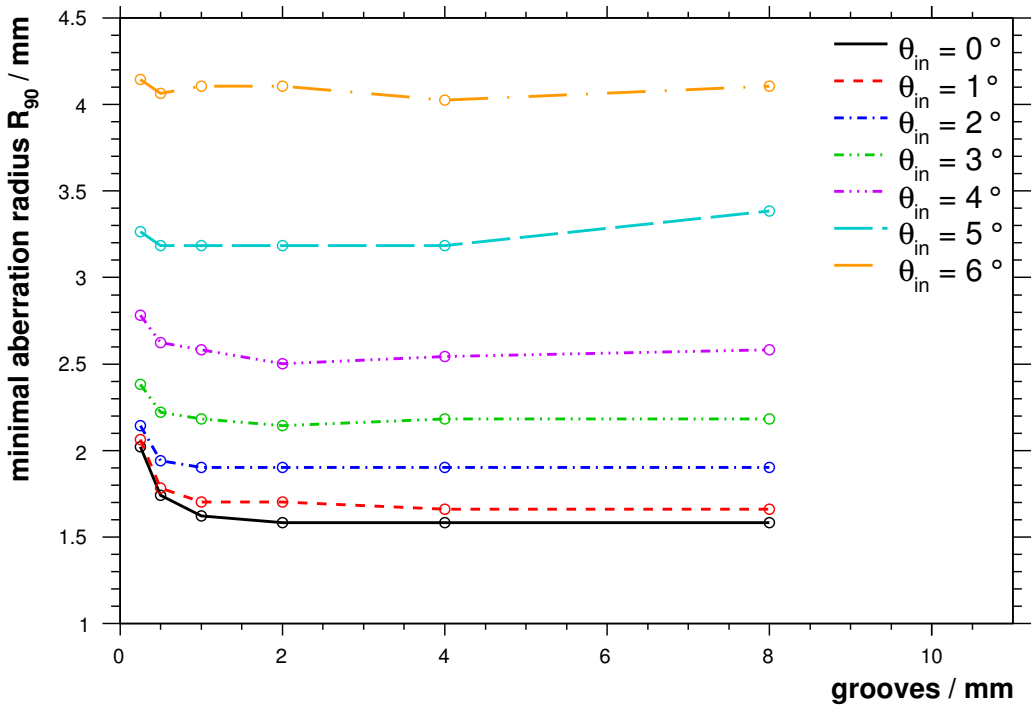

Figure 6.3.2.: Minimal aberration radius R_{90} as a function of the number of grooves per millimeter. The various curves denote different field angles.

of the asphericity of the lens surface can not be addressed in the *Geant4* simulation since there is no built in mechanism to automatically let the parameters be fitted.

With increasing number of grooves per millimeter, the lens-to-focal-plane-distance z with the minimal R_{90} decreases and gets more equivalent to the conventional focal length f as it is plotted in figure 6.3.1. For increasing incident angles θ_{in}, the optimal distance z corresponding to a minimal R_{90} is slightly smaller. This effect is called field of curvature. In figure 6.3.2 the minimal R_{90} is plotted against the number of grooves per millimeter for varying field angles θ_{in}. Since the effects of field of curvature are automatically compensated by this depiction, it attests no significant improvement of R_{90} by an increase in the number of grooves per millimeter to values greater than 2. Therefore, a reasonable choice of $2\,\text{grooves}\,\text{mm}^{-1}$ can is made (see also figure 6.1.2).

Further improvements of the image quality require the lens surface to be aspheric. The aspheric constants A_i can be fitted using a commercial software as presented in the next section.

6.4. Optimisation with Zemax

Zemax is a commercial optics design software which is commonly used in industry by optical engineers and can simulate e.g. lens optics, aspherical systems and the passage of laser beams. A strength of this tool is the autonomous optimisation of free parameters by the minimisation of a user definable “merit-function”.

Property	Value	Equivalent
Type	Fresnel 2	-
Radial height	255.5 mm	$D/2$
Thickness	2.5 mm	d_{thick}
Curvature	$263.7\,\text{mm}^{-1}$	c
Conic constant	-1	k

(a) Parameters of the Fresnel lens representation. The formula equivalents used in this thesis are stated in the last column.

Constant	Value
A_2	$1.18 \cdot 10^{-4}\,\text{m}^{-1}$
A_4	$1.34 \cdot 10^{-9}\,\text{m}^{-4}$
A_6	$9.52 \cdot 10^{-15}\,\text{m}^{-5}$
A_8	$-2.04 \cdot 10^{-19}\,\text{m}^{-7}$

(b) Fitted aspheric constants

Table 6.4.1.: *Zemax* parameters of the Fresnel lens. The type "Fresnel 2" ensures faster computing compared to "Fresnel 1".

The constituents of the merit-function are "operands". An operand might be the spot size on the image plane or the total focal length of the system. Each operand is defined with a "target" and a "weight". The first implicates the desired value, the latter the importance to the total value of the merit-function. The differences between each target and current value are combined to a root-mean-square. The optimisation process is stopped if the merit function could not be reduced significantly compared to the value of the previous step.

The lens parameters of *Zemax* are stated in table 6.4.1a. *Zemax* features two different implementations of Fresnel lenses: "Fresnel 1" and "Fresnel 2". Whereas, in case of "Fresnel 1", the individual grooves of the lens have actual solid representations, for the "Fresnel 2" object, the refraction powers of the grooves are parametrised depending on the position on the lens surface. Thus, "Fresnel 2" has been chosen to speed up the calculation.

It is crucial to carefully set the operands of the merit-function. Otherwise, the automatic optimisation will not lead to an optimal set of parameters. Two predefined operands have been used:

GENC Calculates the radius of the circle which contains a defined fraction of the total energy on the image plane. It has been used to calculate R_{80} for a specific incident angle θ_{in}. Instead of R_{90}, R_{80} requires only 80 % energy

#	Type	Angle θ_{in}	Energy	Target	Weight	Value	Contribution
1	*GENC*	0 °	80 %	0	$1 \cdot 10^3$	1.30 mm	42.5
2	*GENC*	2.5 °	80 %	0	$1 \cdot 10^3$	1.13 mm	57.5
3	*GENC*	5 °	80 %	0	0	1.19 mm	0
4	*GENC*	0 °	90 %	0	0	1.64 mm	0
5	*GENC*	2.5 °	90 %	0	0	1.48 mm	0
6	*GENC*	5 °	90 %	0	0	1.67 mm	0

(a) List of GENC operands. The value is a measure of the aberration radius R_{80} of 80 % encircled energy.

#	Type	Angle θ_{in}	Target	Weight	Value	Contribution
3	*CNPX*	0 °	0 mm	1	0 mm	0
4	*CNPX*	1.5 °	13.4 mm	1	13.1 mm	$3 \cdot 10^{-9}$
5	*CNPX*	3 °	26.8 mm	$1 \cdot 10^5$	26.1 mm	$1 \cdot 10^{-4}$
6	*CNPX*	4.5 °	40.2 mm	1	39.3 mm	$2 \cdot 10^{-8}$
7	*CNPX*	6 °	53.7 mm	$1 \cdot 10^3$	52.5 mm	$3 \cdot 10^{-5}$

(b) List of CNPX operands. The value is a measure of the radial distance of the produced spot to the optical axis.

Table 6.4.2.: Operands of the merit function of *Zemax*. Each row represents a specific operand of the merit function assigned with a target value and a weight. The contribution to the value of the merit function is displayed in the last column.

to be encircled. The results of R_{90} calculated by Zemax heavily fluctuates depending on the number of rays in the simulation and the current geometry of the lens, thus R_{80} had to be chosen. Once the fitting process is complete, R_{90} can be calculated for comparison to the results of *Geant4*.

CNPX Returns the radial distance of the vertex of the refracted light beam on the focal plane to the optical axis. Demanding equal distances of light spots of different incident angles θ_{in}, a distortion free image can be insured.

The exact settings and results of the fit are enlisted in table 6.4.2. The choice on the actual value of the weight is arbitrary. An acceptable compromise between the minimization R_{80} and the position of the spots on the focal plane has to be made. With a weight of 10^3, the contribution of R_{80} to the merit function is not overemphasised compared to the position of the spots for $\theta_{\text{in}} = 3\,^\circ$ and $\theta_{\text{in}} = 6\,^\circ$ with a weight of 10^5. The remainder of the operands are listed for completeness.

For an incident angle of $\theta_{\text{in}} = 5\,^\circ$, the aberration radius R_{90} could be decreased from 3.18 mm to 1.61 mm (compare to figure 6.3.2 and table 6.4.2). Setting only $A_2 \neq 0$,

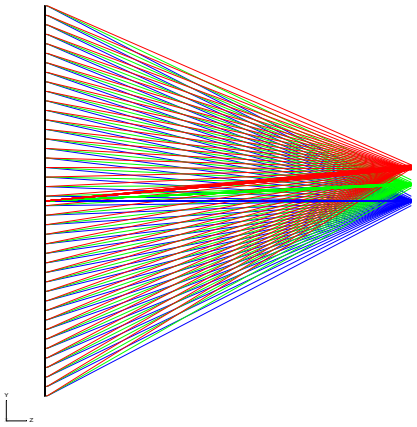

Figure 6.4.1.: Screen-shot of the 3d-layout screen of *Zemax*. The differently coloured rays denote different field angles: blue $\alpha = 0\,^\circ$, green $\alpha = 2.5\,^\circ$ and red $\alpha = 5\,^\circ$.

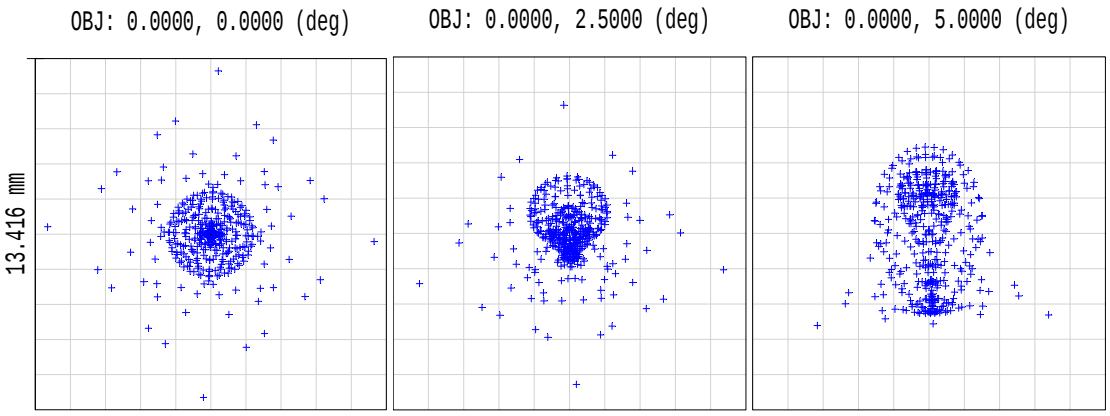

Figure 6.4.2.: Spot diagrams as produced by *Zemax*. On the left hand side the spot for $\theta_{\text{in}} = 0\,^\circ$ is presented, in the middle for $\theta_{\text{in}} = 2.5\,^\circ$ and on the right hand side for $\theta_{\text{in}} = 5\,^\circ$.

the best fit results in $R_{90} = 1.92\,\text{mm}$ for an incidence of $\theta_{in} = 5\,^\circ$. In figures 6.4.1 and 6.4.2 some impressions of the results of the ray-tracing simulation of *Zemax* are shown. The 3-dimensional layout screen shows the path of the rays and the physical representation of the optical components. Zemax also produces spot-diagrams which are scatter diagrams of the data used to create a sampled point spread function. The variant of *Zemax* reproduces all features of the point spread function as shown before in figure 6.2.2.

The results obtained with *Zemax* show the potential of a carefully designed Fresnel lens. For the future, it is planned to incorporate the results into the *Geant4* ray-tracing simulation to get a cross-check on the results and improve the imaging properties of *FAMOUS*.

Chapter 7.

Detector Response Simulation for FAMOUS

The purpose of a detailed ray-tracing simulation of the telescope design is the study of the response if the optics gets exposed to fluorescence light. A quantitative statement will be compiled from the analysis of the signal-to-noise-ratio of the camera pixels of the telescope. The two major contributions to the noise in the detector are the SiPM noise and the brightness of the night-sky. For future refined simulations, it will be essential to fully respect the dynamic behavior of the SiPM as discussed in chapter 3. The schematic presented in figure 7.0.1 summarizes all executed simulation steps as they will be described in the following sections.

7.1. Simulation of Fluorescence Light

The simulation of fluorescence light involves two software packages, namely *CONEX* [30] and *Offline [31]*. Whereas *CONEX* can only be used to simulate the density of the charged particles of an extensive air shower along the shower axis, the *Offline* software package of the Pierre Auger Collaboration is capable of calculating the correct amount of fluorescence light as well as photons from other sources, such as Cherenkov radiation or Rayleigh and Mie scattering, based on the energy deposit of the secondary particles in the atmosphere of the Earth.

7.1.1. Simulation of Extensive Air Showers

CONEX is a hybrid Monte Carlo code to both simulate the particle density and the energy deposit of an extensive air shower with respect to the atmospheric depth [39]. The first hadronic interaction of the primary particle and the interactions of a few secondary particles down to a certain energy threshold are computed by a Monte Carlo code. All interactions below this threshold are parametrised. This approach ensures the reproduction of shower-to-shower fluctuations as well as a short computing time. The time consumption of the code only increases with $\log_{10}(E)$.

The program has been used to create a custom library of proton induced, vertical extensive air showers for discrete, logarithmic energy bins $\log(\Delta E/\mathrm{eV}) = 0.25$ in the energy regime $E = \left[10^{15}, 10^{21}\right]$ eV with azimuth and zenith angle $\phi = \theta = 0\,^{\circ}$. Each energy bin contains 100 extensive air showers. *EPOS* [32] has been chosen as hadronic interaction model.

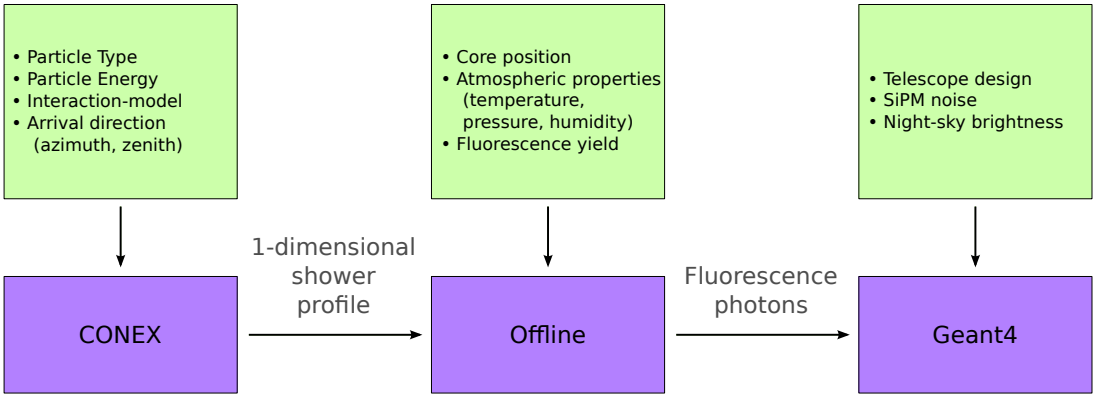

Figure 7.0.1.: Schematic of the detector response simulation. The upper boxes enlist the components of the simulation packages stated below.

#	**Module name**	**Parameters**
1	EventFileReaderOG	
2	MCShowerCheckerOG	
3	EventGeneratorOG	eye=1, telescopeId=4, maxdist=mindist
4	FdSimEventCheckerOG	
5	ShowerLightSimulatorKG	
6	LightAtDiaphragmSimulatorKG	
7	ShowerPhotonGeneratorKG	maxNRaytracePerBin=1024
8	FdLightInfoWriter	eye=1, telescopeId=4

Table 7.1.1.: Chain of *Offline* modules used for the simulation of the fluorescence light. If not stated otherwise, the parameters of the module are arbitrary or equal to the default setting. The minimum and maximum distance to the shower are equal in order to have well defined bins in distance. To have sufficient single bunches of photons, the maximum number of photon bunches per bin on the shower axis had to be increased to 1024.

7.1.2. Fluorescence Light Generation

An adapted version of the standard chain for the simulation of the fluorescence detector of the Pierre Auger Observatory has been used to calculate the fluorescence light produced by the energy deposit of each air shower. A list of the used modules can be found in table 7.1.1.

The purpose of the most important modules is described as follows

EventGeneratorOG It randomizes the core position of the extensive air shower within the field of view of a fluorescence telescope. The minimum and maximum allowed value of R_p have been set equal to force discrete bins in R_p.

ShowerLightSimulatorKG The axis of the extensive air shower is divided into equal spatial bins. According to the total energy deposit within each single axis bin, a model of the fluorescence yield is used to calculate the amount of fluorescence photons emitted from this point.

LightAtDiaphragmSimulatorKG To respect the lateral distribution of the shower profile, a parametrisation of the lateral shower profile is used to smear the point of origin of the photons.

ShowerPhotonGeneratorKG This module is responsible for the ray-tracing of the generated photons through the atmosphere up to the aperture of the telescope while considering Rayleigh and Mie scattering. To save computing time, photons of the same axis bin are grouped to bunches. The maximum number of bunches per axis bin has been set to 1024 which is an arbitrary value but ensures enough statistics in the arrival positions on the aperture. This is important for the simulation of the significantly smaller aperture of *FAMOUS* compared to the fluorescence telescopes of the Pierre Auger Observatory.

FdLightInfoWriter Since there is no module which is capable of exporting information on the photons at this stage in the simulation, a custom module has been developed and inserted at the end of the module chain of *Auger Offline*. The position, direction, wavelength and time of each single photon is exported to a file.

The exported file can be imported into the *Geant4* ray-tracing simulation of *FAMOUS*. Photons are generated according to the saved information in front of the aperture area.

7.2. Night-Sky Background

The intrinsic brightness of the night-sky (NSB) caused by light pollution and stray light of stars, will create a constant noise level in the detector. The commercial Newton reflector Meade Bresser PN203 has been equipped with one pixel consisting of a Winston cone[1] and an SiPM[2] and used to measure the photon flux in a for the human eye apparently dark region at the sky around Arcturus[3] [19]. The measurement has been performed near Aachen in Eynatten, Belgium[4]. Finally, the absolute diffuse radiance of the night-sky for $\lambda \in [200, 1000]\,\mathrm{nm}$ has been determined to be in a range of

$$L_{\mathrm{NSB}} = \left(1.4 \pm 0.2\,(\mathrm{stat}) \; {}^{+1.2}_{-0.8} \; (\mathrm{sys})\right) \cdot 10^{14}\,\mathrm{m^{-2}s^{-1}sr^{-1}} \quad . \tag{7.2.1}$$

[1] $r_1 = 6.71\,\mathrm{mm}$ and $r_2 = 3\,\mathrm{mm}$ with a maximum allowed incident angle of $\theta_{\max} = 26.6\,^\circ$.
[2] Hamamatsu S10362-33-100C, $3 \times 3\,\mathrm{mm}^2$, $100\,\mu\mathrm{m}$ pitch.
[3] Right ascension $\alpha = 14\,\mathrm{h}\,15\,\mathrm{m}\,39.7\,\mathrm{s}$, declination $\delta = 19\,^\circ\,10\,'\,57\,''$, apparent brightness $m = -0.04\,\mathrm{mag}$ [40]
[4] June 1st, 2011, 01:14 h for a duration of 120 s.

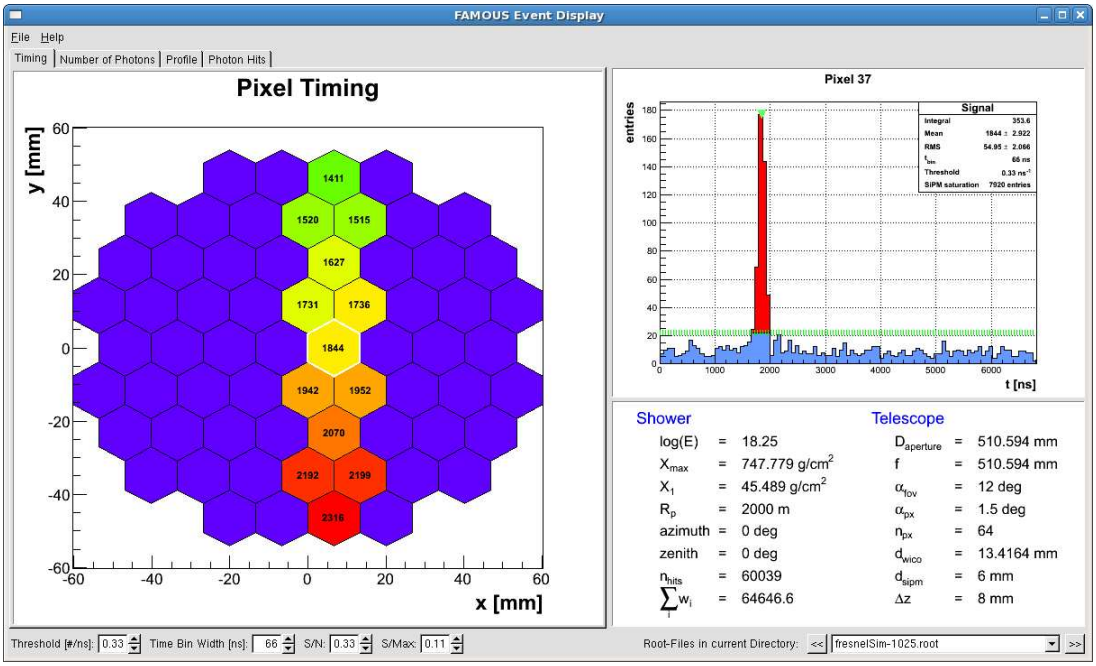

Figure 7.3.1.: *FAMOUS* event display. In the honeycomb plot on the left hand side, each hexagon represents one pixel whereas the number is the mean arrival time of the signal in nanoseconds. The green colors represents early arrival times, red late arrival times. The time distribution of all photon hits within the selected, white framed pixel is depicted in the upper right plot. A simple threshold (green line) has been applied to cut off all noise which is created by the night-sky brightness and the SiPM. The simulated shower has an energy of $E = 10^{18.25}$ eV and an azimuth and zenith angle of $\phi = \theta = 0\,^{\circ}$.

Since the exact wavelength spectrum of the diffuse flux is not known, an upper limit for the night-sky radiance in the fluorescence light regime $\lambda \in [300, 400]\,\mathrm{nm}$ has been set to [19]:

$$L_{\mathrm{NSB,UV}}^{(\mathrm{max})} = 1.9 \cdot 10^{12}\,\mathrm{m^{-2}s^{-1}sr^{-1}} \quad . \tag{7.2.2}$$

Considering the measurement, the *Geant4* ray-tracing simulation generates photons evenly distributed on the aperture during the whole duration of the fluorescence light event. This introduces a realistic noise component although it has to be considered to parametrise the signal of the night-sky in the future to save computation time.

7.3. Event Display

The event display of the *Offline* software package of the Pierre Auger Collaboration has been the archetype for an event display which can be used to visualise the results of the *Geant4* ray-tracing simulation in a familiar way. A screen is presented in figure 7.3.1.

The distribution of the detection time of the hits of one pixel (see right hand side plot in figure 7.3.1) features a clear peak at points in time when the fluorescence light arrives.

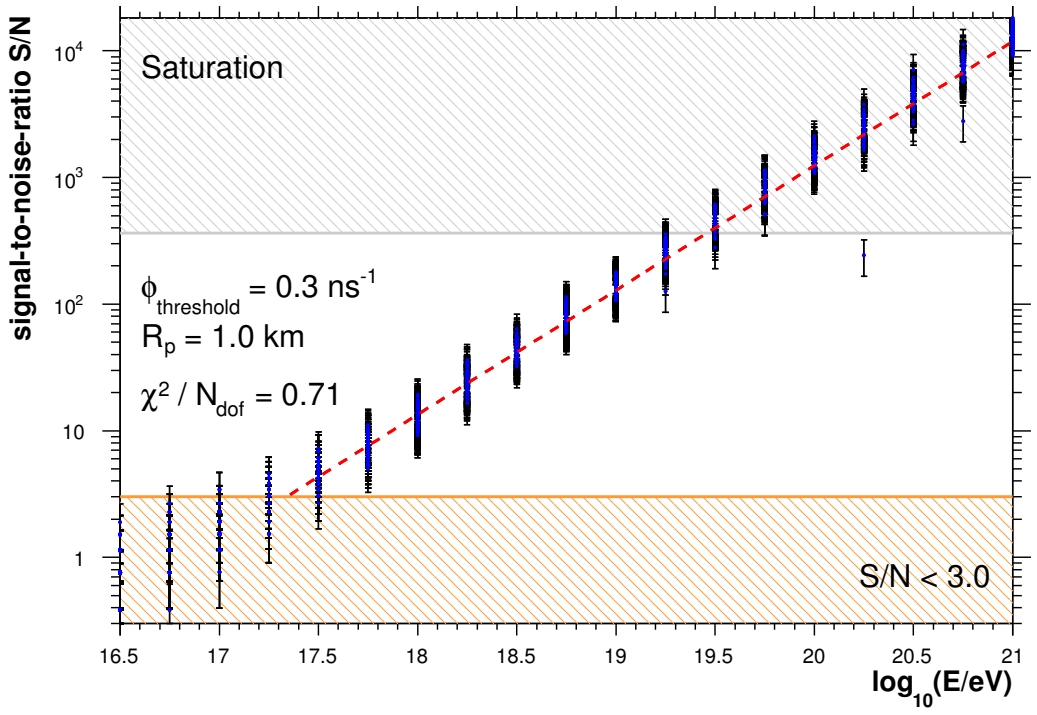

Figure 7.4.1.: Signal-to-noise-ratio (S/N) of *FAMOUS* with respect to the energy of the primary particle. The shower to telescope distance is fixed to $R_p = 1\,\text{km}$. The lower, orange shaded area denotes a $S/N < 3$, the upper, gray shaded the range in which the SiPM would be saturated. The data of the detector response simulation are plotted as blue dots, whereas the dashed red line represents the fit to it. The fit can be used to parametrise the signal-to-noise-ratio between the distance bins.

Since the night-sky light and the noise of SiPMs give a rather constant distribution to the signal, a constant threshold of $\mu_{\text{noise}} = 0.3\,\text{photons ns}^{-1}$ for an integration window of $t_{\text{bin}} = 33\,\text{ns}$ can be applied. The integration window is the bin width used in the distribution of the detection time. The brightness of the night-sky contributes 90 % of the noise signal. After the application of the threshold, the mean of the leftover signal distribution gives the mean arrival time of the fluorescence light. The pixels are colourised according to the arrival time with blue for early and red for late. Thus, the original shower development becomes apparent.

The threshold method makes it also possible to quantify the signal-to-noise-ratio of one pixel.

7.4. Signal-to-Noise-Ratio

With the use of the event display, the signal-to-noise-ratio (S/N) of every single pixel of the camera of the telescope can be calculated. For every shower within the generated shower library, the highest signal-to-noise-ratio entry of all triggered pixels will be kept.

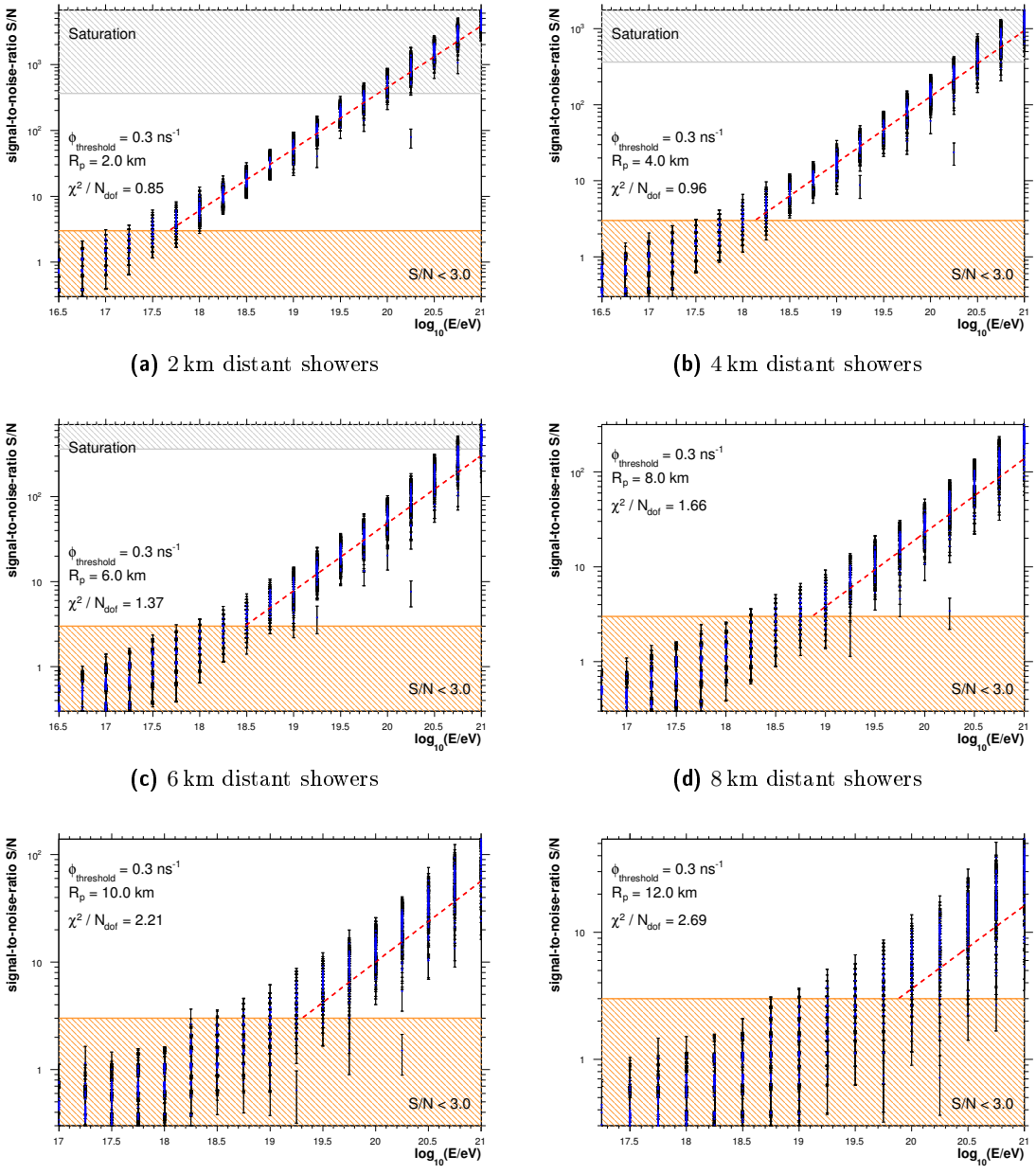

(a) 2 km distant showers

(b) 4 km distant showers

(c) 6 km distant showers

(d) 8 km distant showers

(e) 10 km distant showers

(f) 12 km distant showers

Figure 7.4.2.: Pixel signal-to-noise-ratio of distant showers. See also caption of figure 7.4.1 for more details.

The result of this examination is displayed in figure 7.4.1 with respect to the energy of the extensive air shower. In the regime above a certain signal-to-noise value up to an energy at which saturation starts to occur, the distribution of the data is linear in the double logarithmic presentation. Thus, a fit of

$$\ln(S/N) = a \cdot \log_{10}(E/\mathrm{eV}) + b \tag{7.4.1}$$

gives a good parametrisation in the allowed range. This can be repeated for several distances R_p as shown in figure 7.4.2. The signal-to-noise-ratio decreases with increas-

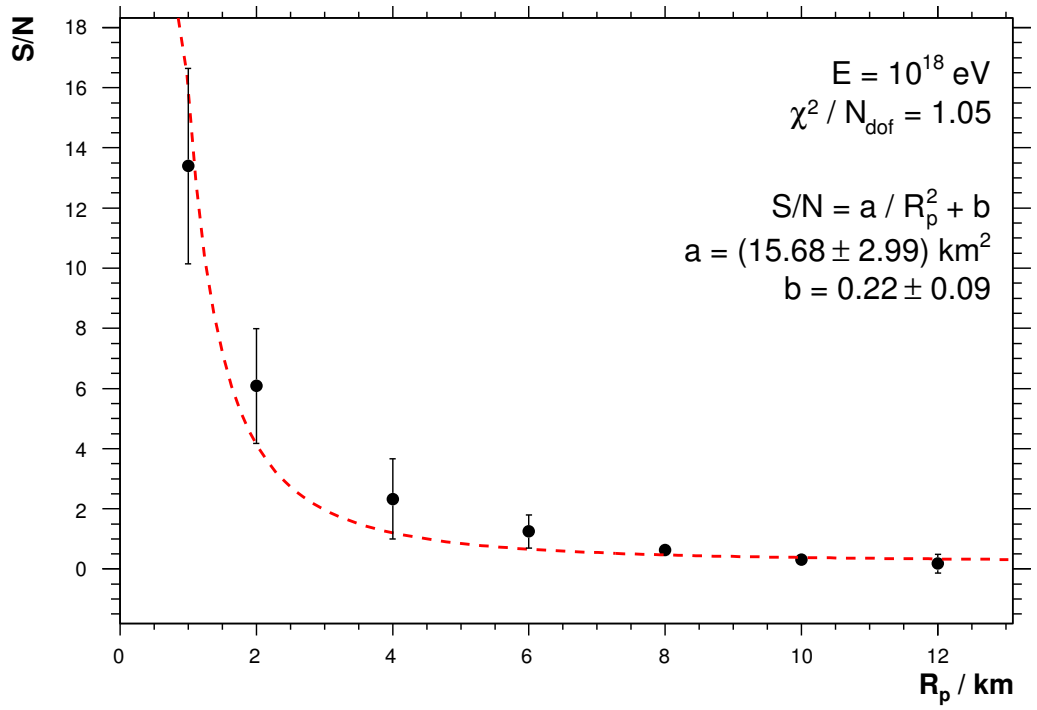

Figure 7.4.3.: Signal-to-noise-ratio with respect to shower distance R_p. The data have been obtained by the fits as shown in figures 7.4.1 and 7.4.2. The red, dashed line denotes a fit of $S/N = a/R_\mathrm{p}^2 + b$ to the data. The result can be used to parametrise the signal-to-noise-ratio between the distance bins. This procedure is repeated for all energy bins.

ing shower-to-telescope-distance R_p. Since the emitted fluorescence light is distributed evenly on a sphere with the surface area $A_\mathrm{O} = 4\pi R_\mathrm{p}^2$, it should apply that

$$S/N \propto \frac{1}{A_O} \propto \frac{1}{R_\mathrm{p}^2} \tag{7.4.2}$$

This function is fitted to the signal-to-noise-ratio of showers of a typical energy bin for varying R_p. The uncertainties are calculated from the mean and variance of the distribution of the data within each bin. In figure 7.4.3 the result of the fit is plotted. Due to the large uncertainties on the simulated data, the $\chi^2/N_\mathrm{dof} \approx 1$ is remarkably good. Attenuation effects of the atmosphere such as Rayleigh and Mie scattering have not been taken into account at this stage.

According to the parametrisation of the signal-to-noise-ratio, the signal-to-noise-ratio can be calculated for intermediate energy and distance bins. A map is shown in figure 7.4.4. The granular simulation of the SiPM as presented in chapter 3 as well as dedicated electronics for data-taking have not yet been considered for this simulation.

For a small expected number of events μ, the Poisson distribution

$$P(N) = \frac{e^{-\mu}\mu^N}{\Pi(N)} \tag{7.4.3}$$

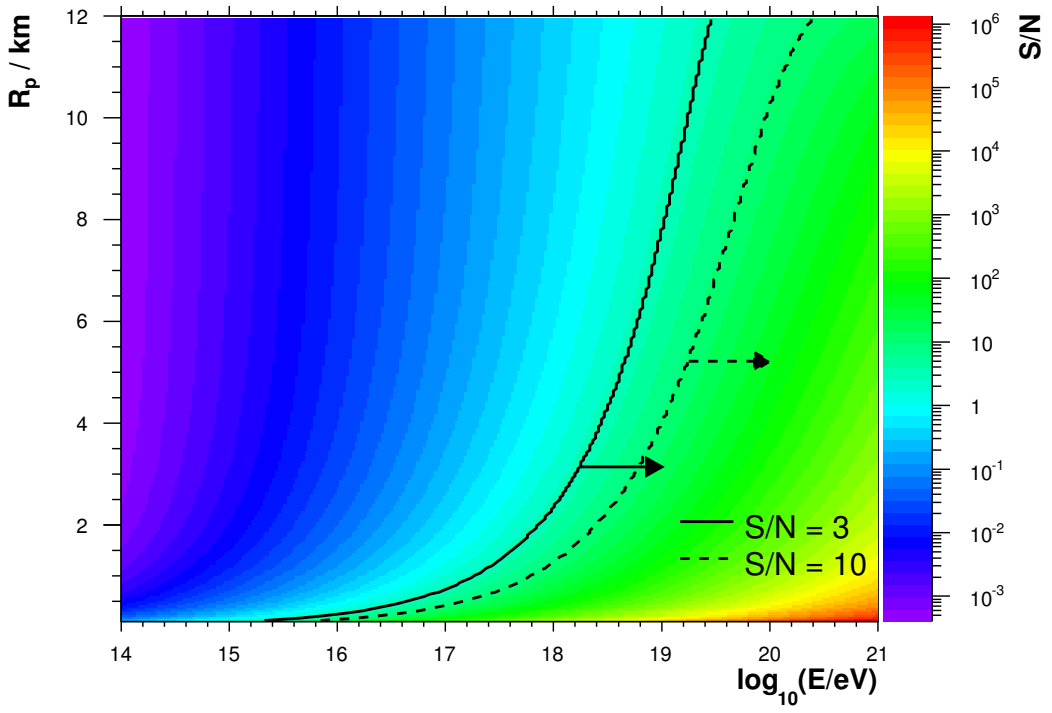

Figure 7.4.4.: Signal-to-noise-ratio S/N with respect to shower distance R_p and energy E. The parametrisations as shown in figures 7.4.1, 7.4.2 and 7.4.3 have been used to interpolate between the distance and energy bins. Two visual guides for $S/N = 3$ and $S/N = 10$ are plotted as black resp. dashed lines.

expresses the probability for the occurrence of N events [41]. The Pi function $\Pi(N)$ returns the factorial of a non-integer number N. In the previous section, a noise threshold of $\mu_\mathrm{noise} = 0.3\,\mathrm{photons\,ns^{-1}}$ for an integration window of $t_\mathrm{bin} = 33\,\mathrm{ns}$ has been chosen for *FAMOUS*. The distribution for a mean of $\mu = \mu_\mathrm{noise} t_\mathrm{bin} = 9.9\,\mathrm{photons}$ is presented in figure 7.4.5. The probability to find a noise event with $N > 3\mu$, which corresponds to a signal-to-noise-ratio of $S/N > 3$, is smaller than 10^{-9}. Therefore, extensive air showers should be well distinguishable from the background with almost 100 % efficiency. Lower energy showers with $E < 10^{17}\,\mathrm{eV}$ may be detectable up to $R_\mathrm{p} \approx 1\,\mathrm{km}$. This is a good result considering the small aperture of the telescope.

The conservative signal-to-noise cut of $S/N > 3$ has to be evaluated again if the granular simulation of the SiPM is applied to the simulation of *FAMOUS*.

7.5. Event Rate

Interesting for the first time operation of the telescope is the question on the expected number of extensive air showers recorded per night. A further look into the measured cosmic ray spectrum is presented in figure 7.5.1. At an energy of $E_1 = 4 \cdot 10^{15}\,\mathrm{eV}$ the spectral index of the power law changes from $\gamma_0 = 2.7$ to $\gamma_1 = 3.0$, at $E_2 = 4 \cdot 10^{18}\,\mathrm{eV}$

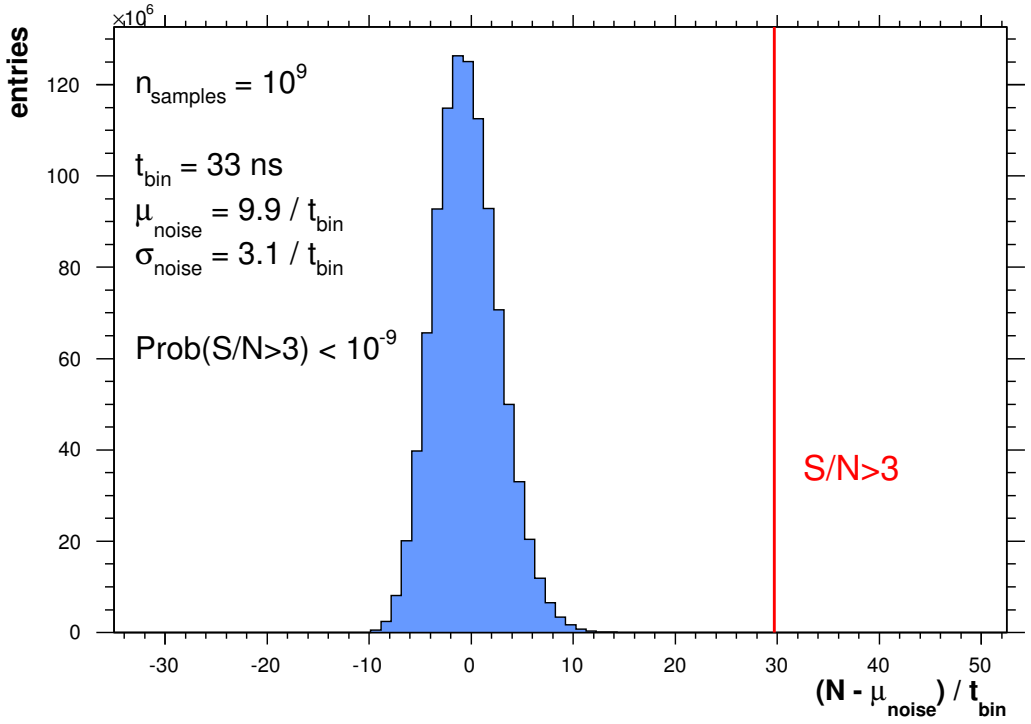

Figure 7.4.5.: Poisson distribution of noise events for an expectation of $\mu_{\text{noise}} = 9.9/t_{\text{bin}}$ and a integration window of $t_{\text{bin}} = 33\,\text{ns}$. The red line refers to a signal to noise greater than three. The probability to find a noise event above this threshold is smaller than 10^{-9}.

to $\gamma_2 = 2.6$. The spectrum cuts off at $E_3 = 3 \cdot 10^{20}\,\text{eV}$. Thus, the differential flux of the cosmic rays can be defined stepwise as

$$\frac{\mathrm{d}n}{\mathrm{d}E\,\mathrm{d}t\,\mathrm{d}\Omega\,\mathrm{d}A} = n_0 \cdot E^{-\gamma} \tag{7.5.1}$$

with the normalisation constants

$$n_0^{(0)} = 1.8 \cdot 10^4\,\mathrm{m}^{-2}\mathrm{sr}^{-1}\mathrm{s}^{-1}\mathrm{GeV}^{\gamma_0-1} \qquad E \leq E_1 \tag{7.5.2}$$

$$n_0^{(1)} = 1.6 \cdot 10^6\,\mathrm{m}^{-2}\mathrm{sr}^{-1}\mathrm{s}^{-1}\mathrm{GeV}^{\gamma_1-1} \qquad E_1 < E \leq E_2 \tag{7.5.3}$$

$$n_0^{(2)} = 2.54 \cdot 10^2\,\mathrm{m}^{-2}\mathrm{sr}^{-1}\mathrm{s}^{-1}\mathrm{GeV}^{\gamma_2-1} \qquad E_2 < E \quad . \tag{7.5.4}$$

The spectral indices and energy boundaries are taken from [1]. The integration of the differential flux over the energy gives the number of cosmic rays above an energy E per time t, solid angle Ω and area A:

$$\tilde{n}(E) = \int_E^{E_3} \frac{\mathrm{d}n}{\mathrm{d}E\mathrm{d}t\,\mathrm{d}\Omega\,\mathrm{d}A}\mathrm{d}E = \int_E^{E_3} n_0 \cdot E'^{-\gamma}\mathrm{d}E' \quad . \tag{7.5.5}$$

Due to the stepwise definition of the differential flux of the cosmic rays, the integral is

$$\tilde{n}(E) = \int_E^{E_1} n_0^{(0)} E'^{-\gamma_0}\mathrm{d}E' + \int_{E_1}^{E_2} n_0^{(1)} E'^{-\gamma_1}\mathrm{d}E' + \int_{E_2}^{E_3} n_0^{(2)} E'^{-\gamma_2}\mathrm{d}E' \tag{7.5.6}$$

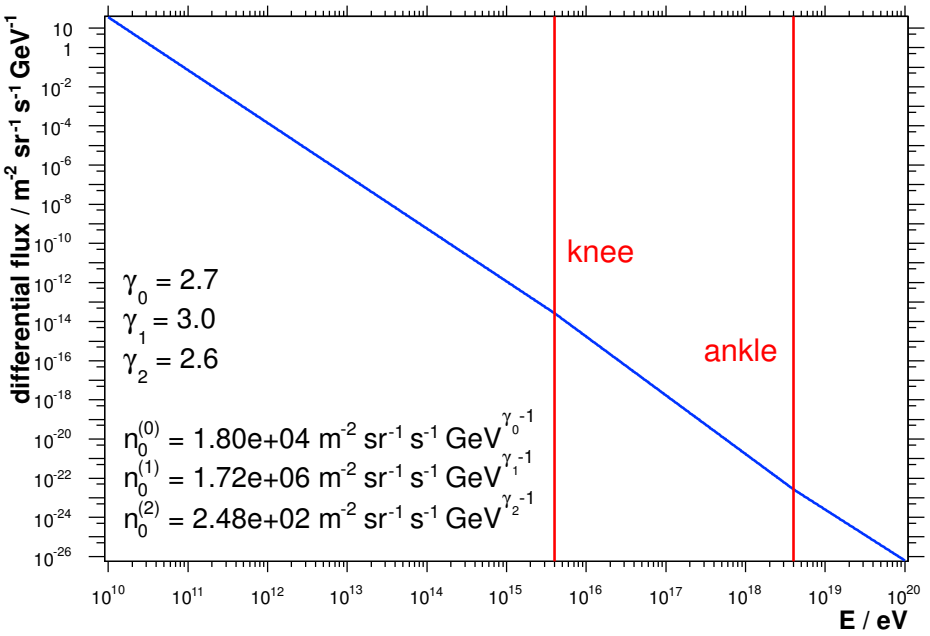

(a) Differential flux of cosmic rays with respect to the primary particles energy. The red lines indicate the different ranges 0, 1 and 2 with the parameters stated at the left lower corner.

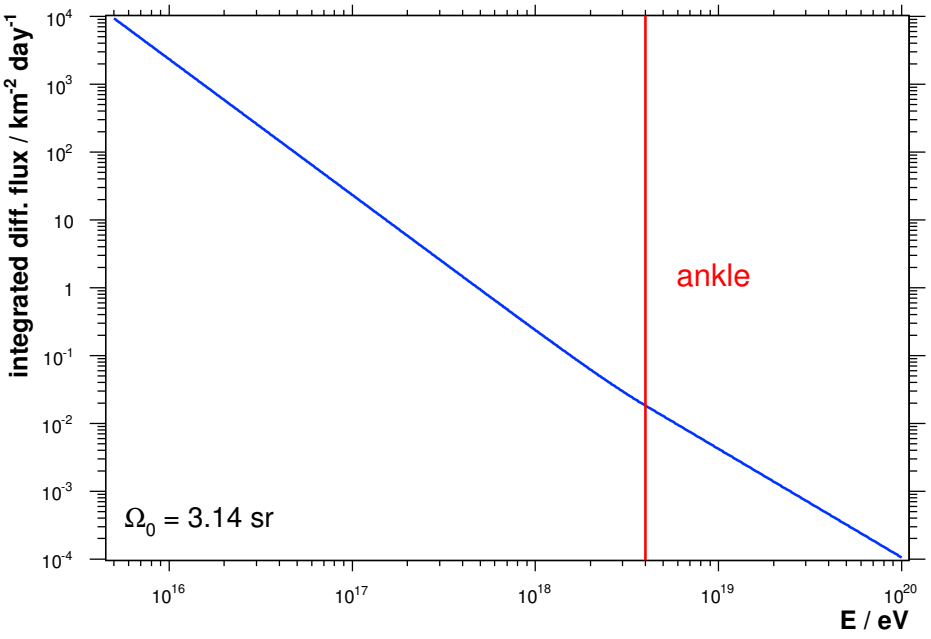

(b) The integrated flux $\tilde{n}$ multiplied by Ω_0 in units of events per km^2 and day with respect to the energy.

Figure 7.5.1.: Cosmic ray spectrum.

for $E \leq E_1$,

$$\tilde{n}(E) = \int_E^{E_2} n_0^{(1)} E'^{-\gamma_1} \mathrm{d}E' + \int_{E_2}^{E_3} n_0^{(2)} E'^{-\gamma_2} \mathrm{d}E' \tag{7.5.7}$$

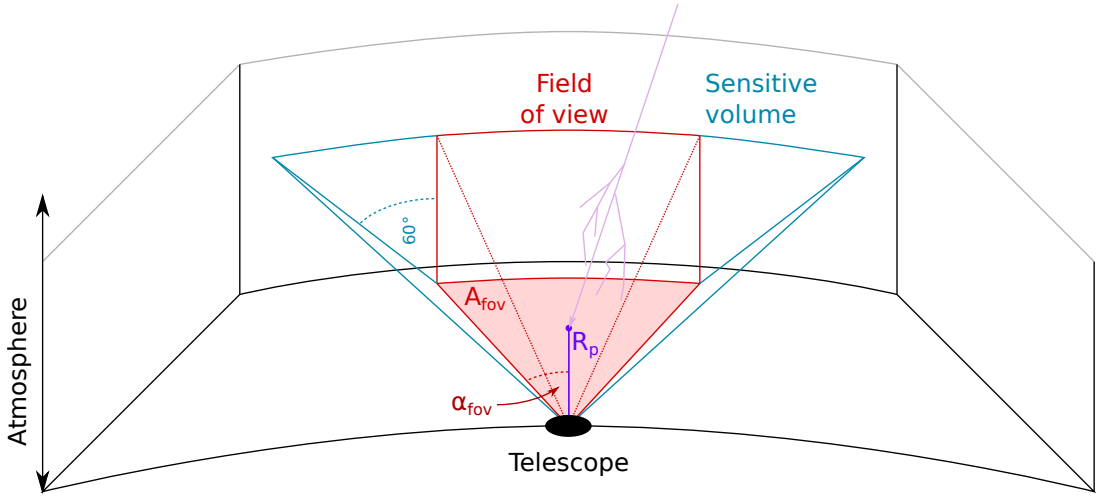

Figure 7.5.2.: Schematic of the field of view of a telescope. The rectangular viewing cone (red) approximates the round viewing cone of *FAMOUS*. Every extensive air shower intersecting the plane A_{fov} with a zenith angle $\theta < 60\,^{\circ}$ can be observed by the telescope. Therefore, the total sensitive volume (blue) is extended.

for $E_1 < E \leq E_2$ and

$$\tilde{n}(E) = \int_{E}^{E_3} n_0^{(2)} E'^{-\gamma_2} \mathrm{d}E' \tag{7.5.8}$$

for $E_2 < E$.

A schematic of the field of view of a telescope is presented in figure 7.5.2. Detecting all cosmic rays having zenith angles $\theta < 60\,^{\circ}$, the solid angle is

$$\Omega_0 = 2\pi \left(1 - cos\left(60^{\circ}\right)\right) \quad . \tag{7.5.9}$$

As depicted in figure 7.5.2, an extensive air shower will be observed in a distance R_p to the telescope and within a triangle with the area

$$A_{\text{fov}}(R_p) = R_p^2 \tan \alpha_{\text{fov}} \quad . \tag{7.5.10}$$

The fluorescence detector of the Pierre Auger Observatory has a duty cycle of roughly $\epsilon = 13\,\%$ [42]. Thus, a conservative value of $\epsilon = 10\,\%$ has been used. The product of $\tilde{n}(E)$, the area A_{fov}, the solid angle Ω_0 and the duty cycle ϵ gives the number of cosmic ray events per time passing the field of view of *FAMOUS*

$$f(E, R_p) = \tilde{n}(E)\Omega_0 A_{\text{fov}}(R_p)\epsilon \quad . \tag{7.5.11}$$

In figure 7.5.3 $f(E, R_p)$ is shown in a two dimensional presentation for the field of view of the fluorescence light telescope with $\alpha_{\text{fov}} = 12\,^{\circ}$. To observe at least one $E = 10^{17}\,\text{eV}$ shower per day, the performance of the telescope should allow the measurement of at least up to 1 km distant showers with this energy. Furthermore, $f(E, R_{\text{p}})$ can be filtered by the signal-to-noise-ratio map applying the signal-to-noise-threshold $S/N > 3$. The result is plotted in figure 7.5.4. Due to the integration in equation 7.5.5, it is sufficient

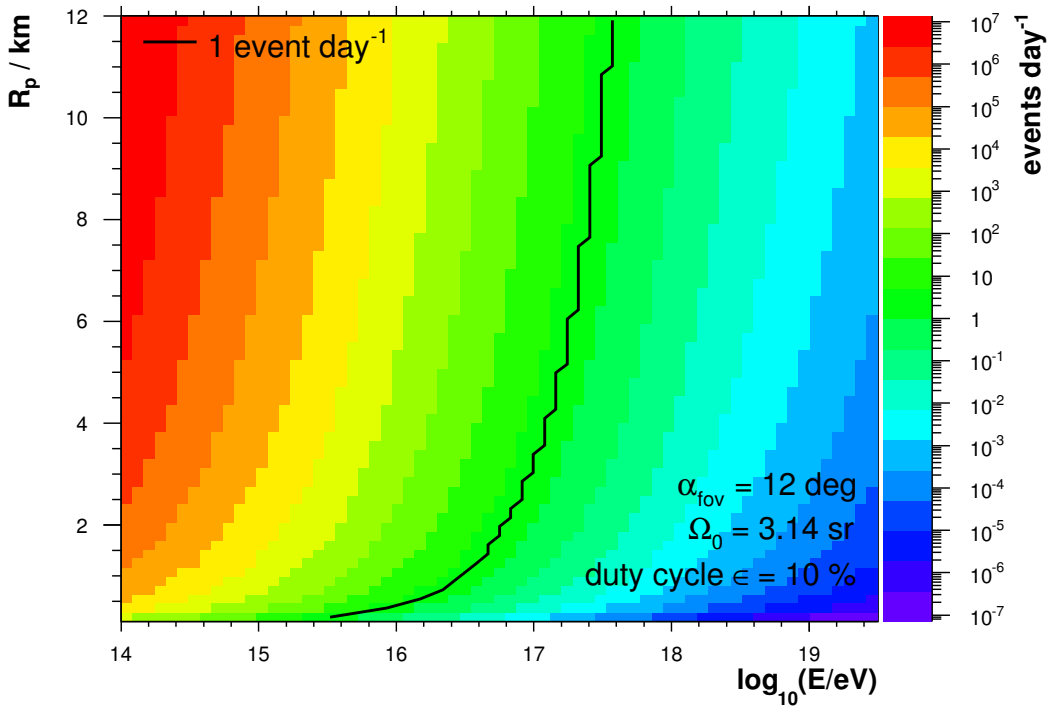

Figure 7.5.3.: Number of events per day with respect to the shower energy E and distance R_p. The data have been calculated for a specific field of view α_fov, solid angle Ω for zenith angles $\theta < 60\,^\circ$ and duty cycle ϵ.

to sum up the bins along the left edge of the histogram in figure 7.5.4 to get the total number of events. The number of cosmic ray events per day is determined to

$$F = 16\,\text{events day}^{-1} \quad . \tag{7.5.12}$$

The X_max of lower energy showers is higher in the atmosphere. In consequence, to detect these showers, the telescope might have to be elevated if the observation of X_max is mandatory. Due to the small field of view, *FAMOUS* can not observe the complete shower development if R_p is small. The lower light deposit in the camera is included in the simulations.

The results have to be handled with care since the granular simulation of the SiPMs as presented in chapter 3 has not yet been integrated. Furthermore, the influence of the electronics has not yet been studied. Therefore, the conservative signal-to-noise cut of $S/N \geq 3$ has been chosen.

The simulation of the SiPMs down to the cellular level requires the fluorescence light simulation to run with as less thinning as possible. If not, a bunch of $\gg 1$ photons may hit one SiPM cell, which is still recovering, and thus gets rejected. The reduction of the signal-to-noise-ratio due to the dynamics of the SiPM will be overestimated. Subsequently, the disabling of thinning requires a great amount of computation time and disk space. It has to be considered whether an integration of the detector simulation of *FAMOUS* into *Auger Offline* as individual module is a feasible solution.

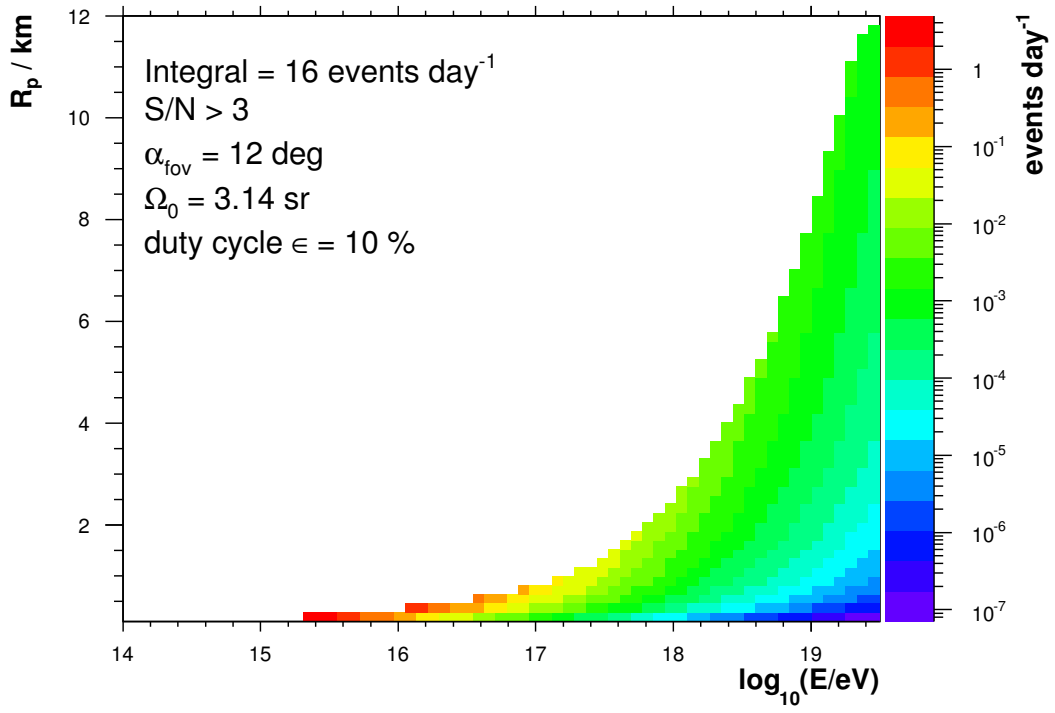

Figure 7.5.4.: Number of events per day filtered by the signal-to-noise-ratio with respect to the shower energy E and distance R_p. Areas in figure 7.5.3 where $S/N < 3$ have been masked white. The sum of all bins along the left edge in the histogram results in a total event count per day of 16.

In fact, 90 % of the noise is contributed by night-sky brightness in Aachen. Operating the telescope in a darker environment e.g. the site of the Pierre Auger Observatory would help to significantly reduce the noise and therefore may enable the observation of lower fluorescence light signals.

Altogether, the *FAMOUS* telescope is a promising approach for the detection of extensive air showers. Due to its compactness, it will be easy to operate and modify.

Chapter 8.

Summary and Outlook

The optics of the fluorescence telescope *FAMOUS* consist of a refractive design of which the main component is a big Fresnel lens with a diameter of $D = 511\,\mathrm{mm}$ equal to the focal length f. To increase the size of the focal plane equipped with 8×8 hexagonally arranged pixels, a Winston cone with an entrance radius of $r_1 = 6.71\,\mathrm{mm}$ is placed in front of each $6 \times 6\,\mathrm{mm}^2$ silicon photomultiplier (SiPM). The combination of one SiPM and one Winston cone forms an individual camera pixel.

SiPMs show a very dynamic behaviour due to their cellular substructure, recovery time and several noise phenomena. A custom *Geant4* simulation of the devices has been used to fully characterise the dynamic range. If the light flux exceeds $\phi = 1\,\mathrm{photon}\,t_{rec}^{-1}\,\mathrm{cell}^{-1}$, the SiPM is able to detect approximately 65% of the photons.

The reflective Winston cone has a high transmission efficiency of approximately 90 % if made out of polished aluminium. The transmission is constant for inclined light up to a maximum allowed incident angle $\theta_{\max}$ and quickly drops to zero afterwards. This prevents stray light from lowering the signal-to-noise-ratio. Due to the light concentration, photons leave the cone under skew angles. Even though the SiPM is coated with additional layers to smooth the optical transition, there is a drop in the photon detection efficiency which sets in for incident angles $> 60\,^\circ$. The combination of a Winston cone and an SiPM detects approximately 22 % of the incoming light. This equals a further decrease of the photon detection efficiency by 30 % also considering the drop by the transmission efficiency of the Winston cone.

The commercial optics software *ZEMAX* has been used to optimise the asphericity of the surface of the Fresnel lens. Therefore, it is possible to overcome spherical aberrations for lenses with a small focal number $N_\mathrm{f} = 1$. A granularity of 2 grooves per millimeter is sufficient for the focusing of over 90 % of the refracted light onto a single camera pixel.

Simulations of extensive air showers have been performed with the program *CONEX* and simulations of the emitted fluorescence light with the software package *Offline* of the Pierre Auger Collaboration. The simulation of *FAMOUS* is based on the framework *Geant4* and able to compile a complete detector response. The signal-to-noise-ratio of the pixels of the focal plane has been determined for a discrete set of bins in shower energy E and shower-to-telescope distance R_p. As a first result, air showers with an energy of $E < 10^{17}\,\mathrm{eV}$ are likely to be detectable up to $R_\mathrm{p} = 1\,\mathrm{km}$. A total count of $16\,\mathrm{events\ day}^{-1}$ is to be expected when operated with a duty cycle of 10 %.

The presented design promises a great performance considering its small aperture size and field of view. If the fluorescence light detection with *FAMOUS* succeeds, the next step is to decrease the field of view of a single pixel. By this, the shower development will be resolved fine grained. At the same time, the signal-to-noise-ratio of a single pixel can be increased which renders the detection of even lower energy or more distant showers possible.

The detailed response pattern simulations of the SiPMs as well as the optimisations of the Fresnel lens should be included in the detector simulation of *FAMOUS* to improve the prediction quality. Additionally, the fluorescence light simulation is required to run without any thinning because of the large granularity of the SiPMs which will require a considerable amount of computing resources. It should be evaluated whether it is feasible to integrate the simulation of *FAMOUS* as an individual module into the *Offline* software.

At the time of the completion of this thesis, the mechanical workshop of the RWTH Aachen has already started the mechanical design of the presented telescope and *FAMOUS* will measure the first light within the next year.

Bibliography

[1] J. Blümer, R. Engel, and J. Hörandel, "Cosmic rays from the knee to the highest energies," *Progress in Particle and Nuclear Physics*, vol. 63, no. 2, pp. 293–338, 2009. arXiv:0904.0725v1.

[2] Particle Data Group, *Review of particle physics.* Journal of physics, Inst. of Physics Publ., 2011.

[3] J. Hoerandel, "On the knee in the energy spectrum of cosmic rays," *Astroparticle Physics*, vol. 19, no. 2, pp. 193–220, 2003.

[4] K. Greisen, "End to the Cosmic-Ray Spectrum?," *Phys. Rev. Lett.*, vol. 16, pp. 748–750, Apr 1966.

[5] A. Hillas, "The origin of ultra-high-energy cosmic rays," *Annual Review of Astronomy and Astrophysics*, vol. 22, pp. 425–444, 1984.

[6] W. Baade and F. Zwicky, "Remarks on Super-Novae and Cosmic Rays," *Phys. Rev.*, vol. 46, pp. 76–77, Jul 1934.

[7] E. Fermi, "On the Origin of the Cosmic Radiation," *Phys. Rev.*, vol. 75, pp. 1169–1174, Apr 1949.

[8] C. Grupen, *Astroparticle physics.* Springer Verlag, 2005.

[9] F. Arqueros, J. Hörandel, and B. Keilhauer, "Air fluorescence relevant for cosmic-ray detection - Summary of the 5th fluorescence workshop, El Escorial 2007," *Nuclear Instruments and Methods in Physics Research Section A: Accelerators, Spectrometers, Detectors and Associated Equipment*, vol. 597, no. 1, pp. 1–22, 2008. arXiv:0807.3760v1.

[10] M. Ave, M. Bohacova, B. Buonomo, L. Cazon, S. Chemerisov, M. Conde, R. Crowell, P. Di Carlo, C. Di Giulio, *et al.*, "Measurement of the pressure dependence of air fluorescence emission induced by electrons," *Astroparticle Physics*, vol. 28, no. 1, pp. 41–57, 2007. arXiv:astro-ph/0703132v1.

[11] F. Kakimoto, E. Loh, M. Nagano, H. Okuno, M. Teshima, and S. Ueno, "A measurement of the air fluorescence yield," *Nuclear Instruments and Methods in Physics Research Section A: Accelerators, Spectrometers, Detectors and Associated Equipment*, vol. 372, no. 3, pp. 527–533, 1996.

[12] M. Nagano, K. Kobayakawa, N. Sakaki, and K. Ando, "New measurement on photon yields from air and the application to the energy estimation of primary cosmic rays," *Astroparticle Physics*, vol. 22, no. 3-4, pp. 235–248, 2004. arXiv:astro-ph/0406474v2.

[13] J. Abraham, P. Abreu, M. Aglietta, C. Aguirre, E. Ahn, D. Allard, I. Allekotte, J. Allen, P. Allison, J. Alvarez-Muñiz, *et al.*, "The fluorescence detector of the Pierre Auger Observatory," *Nuclear Instruments and Methods in Physics Research Section A: Accelerators, Spectrometers, Detectors and Associated Equipment*, vol. 620, no. 2-3, pp. 227–251, 2010.

[14] J. Abraham, P. Abreu, M. Aglietta, C. Aguirre, E. Ahn, D. Allard, I. Allekotte, J. Allen, J. Alvarez-Muñiz, M. Ambrosio, *et al.*, "Operations of and future plans for the Pierre Auger Observatory," *arXiv:0906.2354*, 2009.

[15] N. Scharf, *The Spectrum of Cosmic Rays detected with the HEAT extension at the Pierre Auger Observatory.* PhD thesis, RWTH Aachen University, 2011.

[16] I. Allekotte, A. Barbosa, P. Bauleo, C. Bonifazi, B. Civit, C. Escobar, B. García, G. Guedes, M. Gómez Berisso, J. Harton, *et al.*, "The surface detector system of the Pierre Auger Observatory," *Nuclear Instruments and Methods in Physics Research Section A: Accelerators, Spectrometers, Detectors and Associated Equipment*, vol. 586, no. 3, pp. 409–420, 2008. arXiv:0712.2832v1.

[17] J. Rennefeld and A. Stahl, "Studien zur Eignung von Silizium Photomultipliern für den Einsatz im erweiterten CMS Detektor am SLHC," Master's thesis, 2010.

[18] D. Renker and E. Lorenz, "Advances in solid state photon detectors," *Journal of Instrumentation*, vol. 4, p. P04004, 2009.

[19] M. Stephan, T. Hebbeker, M. Lauscher, C. Meurer, T. Niggemann, and J. Schumacher, "Future use of silicon photomultipliers for the fluorescence detection of ultra-high-energy cosmic rays," *SPIE*, vol. 8155 81551B-1, 2011.

[20] P. Hallen, "Determination of the Recovery Time of Silicon Photomultipliers," Master's thesis, Phys. Inst. III A, RWTH Aachen University, Aachen, Germany, 2011.

[21] M. Polyanskiy, "Refractive index database," 12 2011. http://refractiveindex.info.

[22] P. Eckert, H. Schultz-Coulon, W. Shen, R. Stamen, and A. Tadday, "Characterisation studies of silicon photomultipliers," *Nuclear Instruments and Methods in Physics Research Section A: Accelerators, Spectrometers, Detectors and Associated Equipment*, vol. 620, no. 2-3, pp. 217–226, 2010.

[23] Hamamatsu, "http://jp.hamamatsu.com/resources/products/ssd/pdf/s10362-11_series_kapd1022e05.pdf," Nov. 2009.

[24] A. N. Otte, *Observation of VHE γ-Rays from the Vicinity of magnetized Neutron Stars and Development of new Photon-Detectors for Future Ground based γ-Ray Detectors.* PhD thesis, Technische Universität München, 2007.

[25] M. Lauscher, "Characterization Studies of Silicon Photomultipliers for the Detection of Fluorescence Light from Extensive Showers," Master's thesis, Phys. Inst. III A, RWTH Aachen University, Aachen, Germany, 2011.

[26] S. Agostinelli, J. Allison, K. Amako, J. Apostolakis, H. Araujo, P. Arce, M. Asai, D. Axen, S. Banerjee, G. Barrand, *et al.*, "Geant4 - a Simulation Toolkit," *Nuclear Instruments and Methods*, vol. 506, no. 3, pp. 250–303, 2003.

[27] B. Wardle, *Principles and applications of photochemistry*. Wiley, 2009.

[28] R. Winston, J. Miñano, W. Welford, and P. Benítez, *Nonimaging optics*. Academic Press, 2005.

[29] G. Schröder and H. Treiber, *Technische Optik*. 2007.

[30] T. Pierog, M. Alekseeva, T. Bergmann, V. Chernatkin, R. Engel, D. Heck, N. Kalmykov, J. Moyon, S. Ostapchenko, T. Thouw, *et al.*, "First results of fast one-dimensional hybrid simulation of EAS using CONEX," *Nuclear Physics B-Proceedings Supplements*, vol. 151, no. 1, pp. 159–162, 2006. arXiv:astro-ph/0411260v1.

[31] S. Argirŋ, S. Barroso, J. Gonzalez, L. Nellen, T. Paul, T. Porter, L. Prado Jr, M. Roth, R. Ulrich, and D. Veberic, "The offline software framework of the Pierre Auger Observatory," *Nuclear Instruments and Methods in Physics Research Section A: Accelerators, Spectrometers, Detectors and Associated Equipment*, vol. 580, no. 3, pp. 1485–1496, 2007. arXiv:0707.1652v1.

[32] K. Werner, "The hadronic interaction model EPOS," *Nuclear Physics B-Proceedings Supplements*, vol. 175, pp. 81–87, 2008.

[33] A. Bucholtz, "Rayleigh-scattering calculations for the terrestrial atmosphere," *Applied Optics*, vol. 34, no. 15, pp. 2765–2773, 1995.

[34] R. Wilson, *Reflecting telescope optics I*, vol. 1. 2007.

[35] B. A. Anicin, V. M. Babovic, and D. M. Davidovic, "Fresnel lenses," *American Journal of Physics*, vol. 57, pp. 312–316, 1989.

[36] J. Costa, M. Pimenta, and B. Tomé, "A Geant4 based engineering tool for Fresnel lenses," *Nuclear Science, IEEE Transactions on*, vol. 54, no. 2, pp. 313–319, 2007.

[37] The Geant4 "Advanced examples" Working Group, "Examples list," 12 2011. http://geant4advancedexampleswg.wikispaces.com/ExamplesList.

[38] H. Gross, W. Singer, and M. Totzeck, *Handbook of Optical Systems: Physical image formation*. Handbook of Optical Systems, Wiley-VCH, 2005.

[39] T. Bergmann, R. Engel, D. Heck, N. Kalmykov, S. Ostapchenko, T. Pierog, T. Thouw, and K. Werner, "One-dimensional hybrid approach to extensive air shower simulation," *Astroparticle Physics*, vol. 26, no. 6, pp. 420–432, 2007.

[40] "Simbad astronimical database," 12 2011. http:/simbad.u-strasbg.fr/simbad/sim-id?Ident=Arcturus.

[41] F. James, *Statistical Methods in Experimental Physics*. World Scientific, 2006.

[42] M. Albrowd, D. Allarde, I. Allekottef, P. Allisong, J. Munizbb, M. do Amaral, M. Ambrosio, L. Anchordoqui, R. Andrews, M. Anguiano, *et al.*, "Properties and performance of the prototype instrument for the Pierre Auger Observatory," *Nuclear Instruments and Methods in Physics Research A*, vol. 523, pp. 50–95, 2004. arXiv:astro-ph/0308427.

[43] Fresnel Optics GmbH, "Private communications." 03 2011.

[44] Schott GmbH, "Private communications." 03 2011.

Acknowledgements
Danksagungen

An dieser Stelle darf ich all denjenigen danken, die mich während des letzten Jahres begleitet haben.

Außerordentlicher Dank gilt vor allem Herrn Prof. Dr. Hebbeker für die Ermöglichung dieser Arbeit, Herrn Prof. Dr. Martin Erdmann für die Bereitschaft das Zweitgutachten anzufertigen, und beiden gleichermaßen für die vielen wertvollen Diskussionen während der gemeinsamen Meetings. Sie gaben mir die nötigen Anstöße Probleme aus neuen Perspektiven zu betrachten und zu lösen.

Des weiteren sei meiner Betreuerin Dr. Christine Meurer und der gesamten Auger Arbeitsgruppe des III. Physikalischen Instituts A der RWTH Aachen für die große Unterstützung und die freundliche und produktive Arbeits-Atmosphäre gedankt.

Insbesondere erwähnt seien die Mitglieder unserer kleinen Kollaboration um *FAMOUS*, bestehend aus Markus Lauscher, Johannes Schumacher und Maurice Stephan, der ein unersetzlicher Begleiter meiner Arbeit war. Nils Scharf möchte ich für die Unterstützung bei der Bedienung des Software-Pakets *Offline* danken.

Großer Dank gilt zudem Herrn Dr. Markus Merschmeyer für die Einrichtung und Ausstattung des Undergraduate-Projektes zur Optimierung von Fresnel Linsen mit *Zemax* und den beiden Teilnehmern Daniel Schröder und Benjamin Zacher für die gute Zusammenarbeit.

Ich möchte mich bei allen Mitarbeitern der Mechanik-Werkstatt des Instituts für die gute Zusammenarbeit bei der Produktion der Lichtsammelleiter und insbesondere Herrn Barthel Phillips für die zahlreichen technischen Zeichnungen und die mechanische Konstruktion der fokalen Ebene danken.

Zu guter Letzt sei meinen Korrekturlesern für ihre Geduld und meiner Familie und meinen Freunden für den guten Rückhalt während der Arbeitsphase gedankt.

Appendix A.

Material Properties

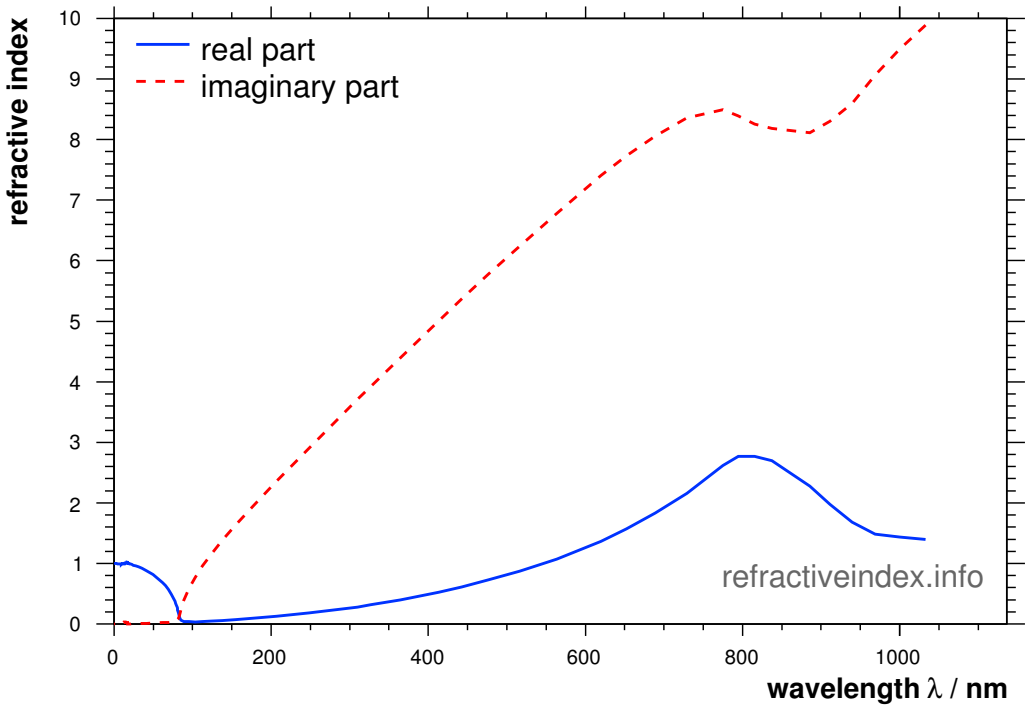

Figure A.0.1.: Refractive index of aluminium with respect to the photon wavelength λ [21]. The blue line denotes the real, the red, dashed, the imaginary part of the refractive index.

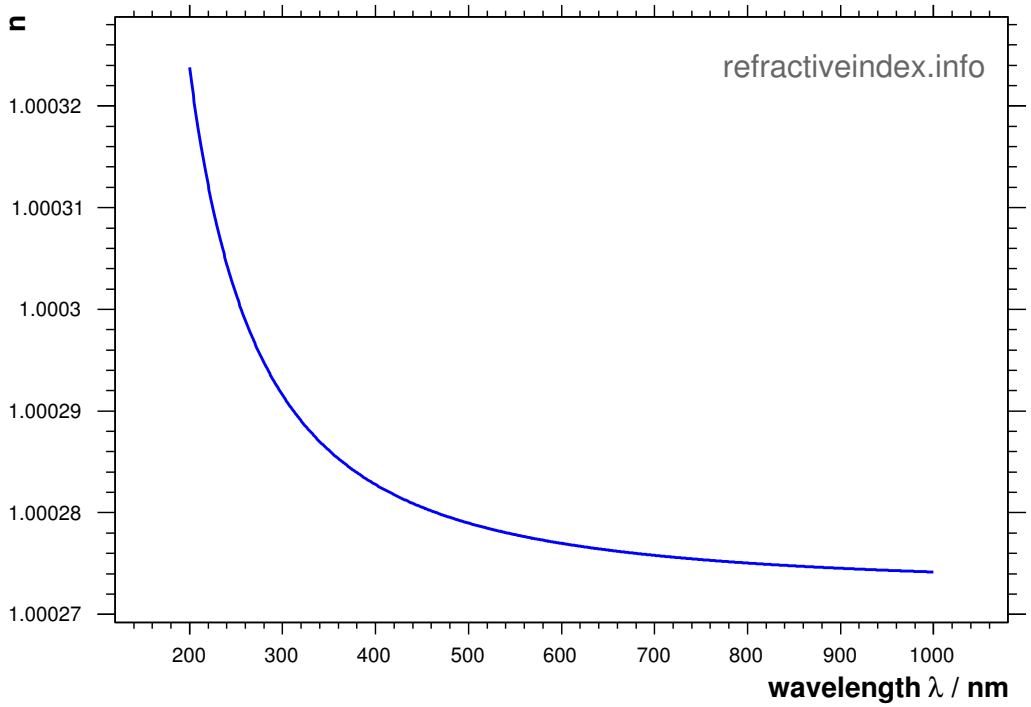

Figure A.0.2.: Refractive index of standard air with respect to the photon wavelength λ [21]. Dry air at $15\,°C$, $1013.25\,hPa$ and with $450\,ppm$ CO_2 content.

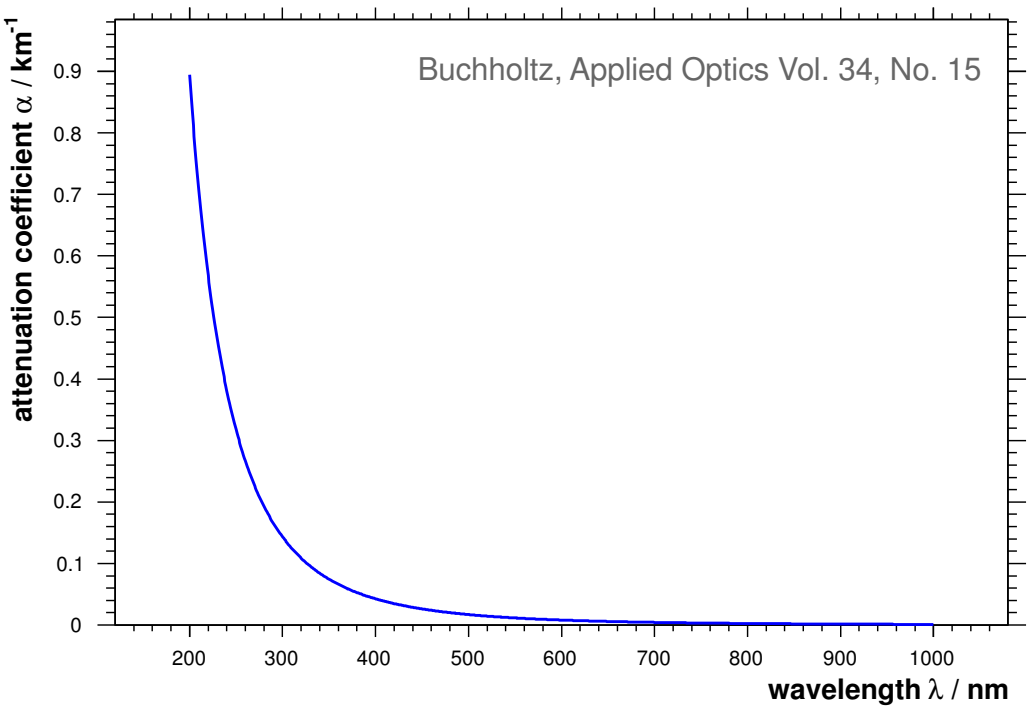

Figure A.0.3.: Rayleigh attenuation coefficient of standard air with respect to the photon wavelength λ [33]. Dry air at $15\,°C$, $1013.25\,hPa$ and with $450\,ppm$ CO_2 content.

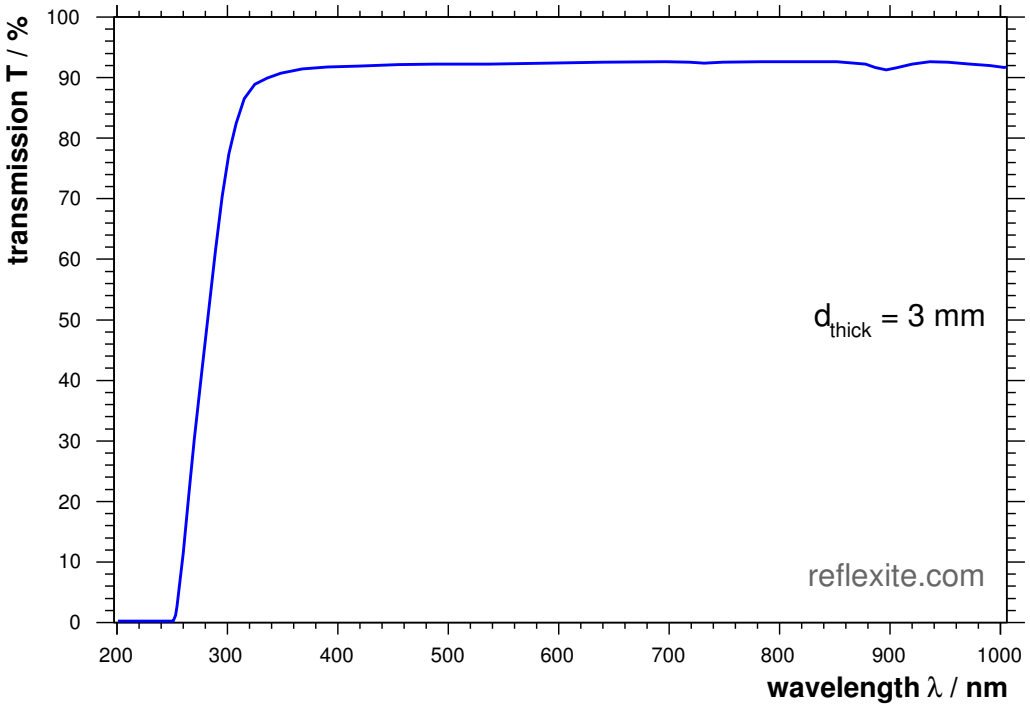

Figure A.0.4.: Transmission of PMMA versus the photon wavelength λ [43].

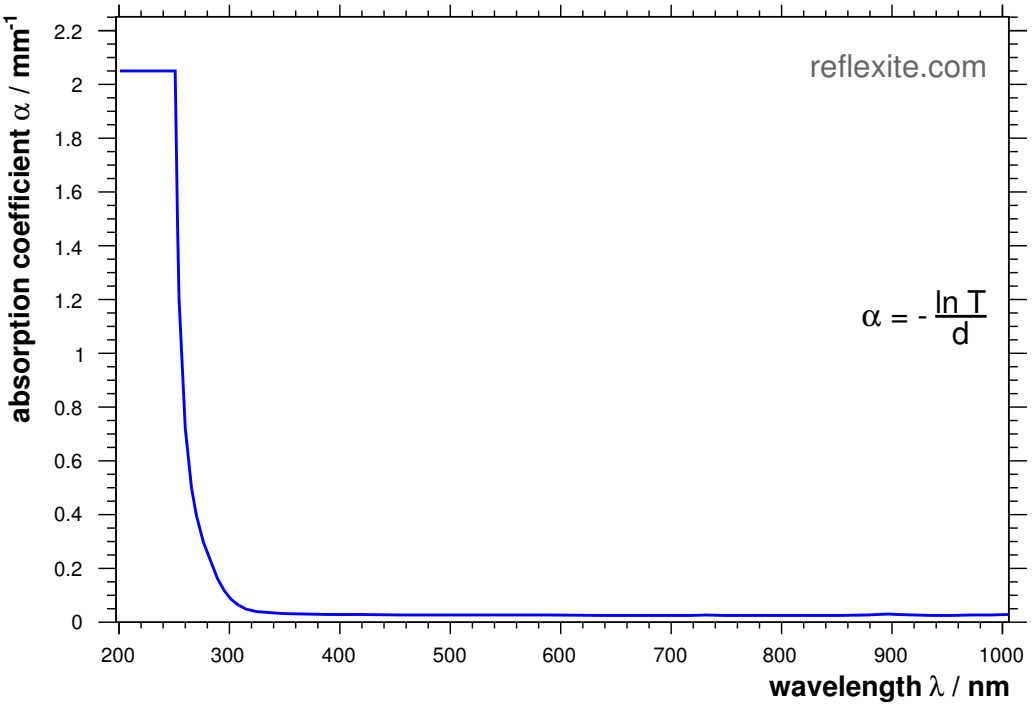

Figure A.0.5.: Absorption of PMMA versus the photon wavelength λ.

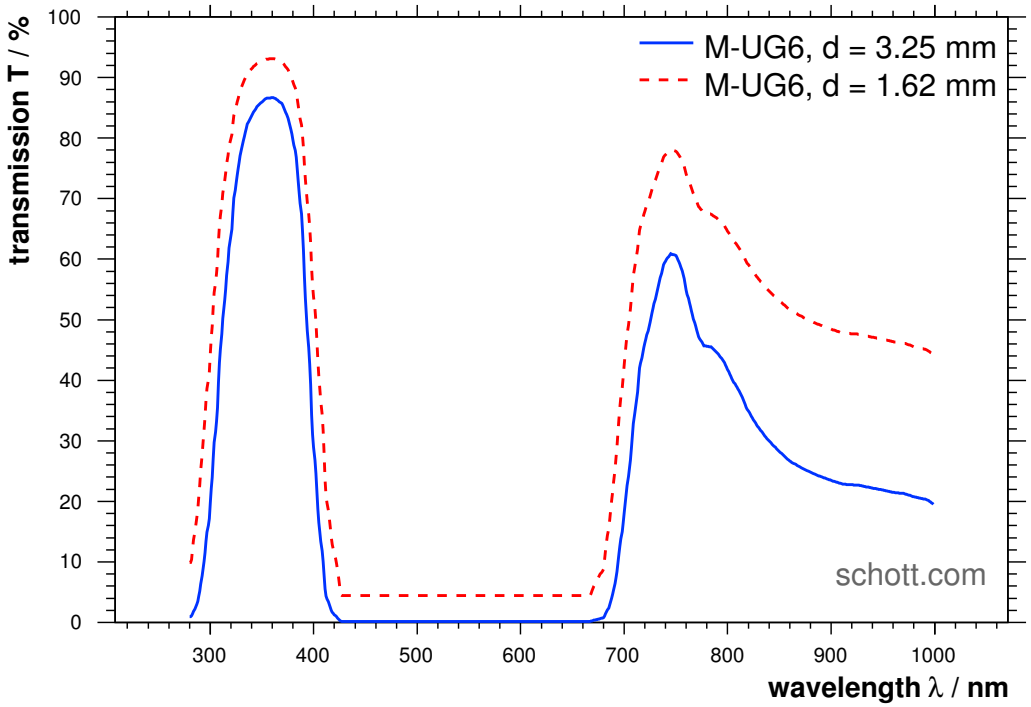

Figure A.0.6.: Transmission of M-UG6 filter glass versus the photon wavelength λ [44]. The red dashed line denotes the transmission for the half material thickness.

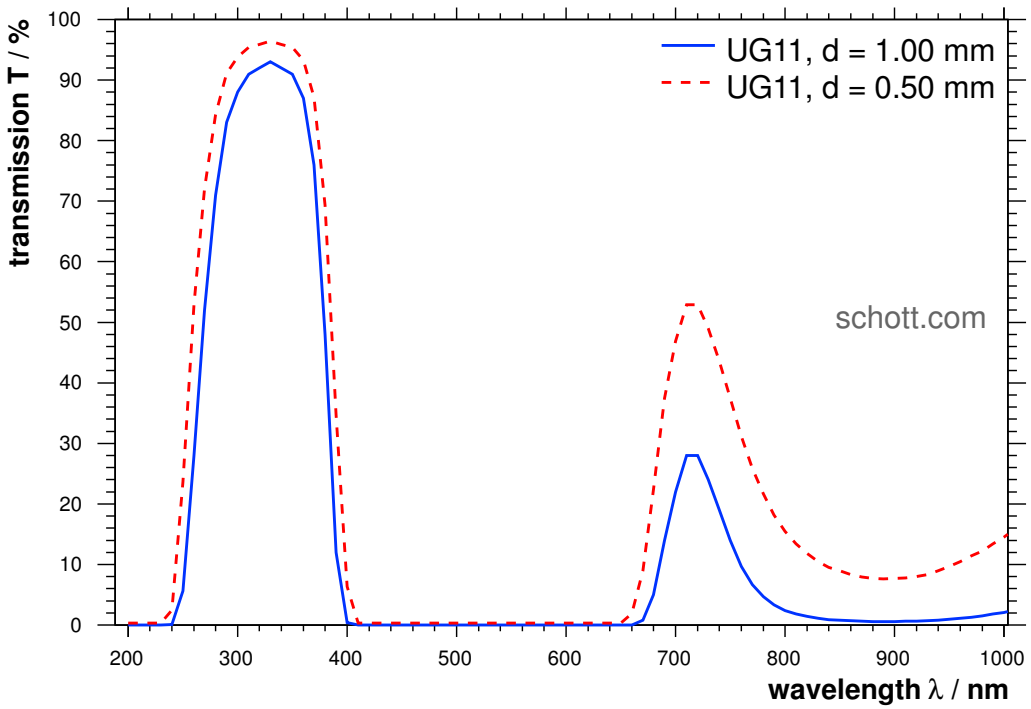

Figure A.0.7.: Transmission of UG11 filter glass versus the photon wavelength λ [44]. UG11 is a successor of M-UG6 with less transmission in the near infrared-regime $\lambda > 650\,\mathrm{nm}$.

Appendix B.

C++ Code Fragments

```
// Create some arrays.
const int nZPlanes = 128;
G4double* zPlanes = new G4double[nZPlanes];
G4double* rInner = new G4double[nZPlanes];
G4double* rOuter = new G4double[nZPlanes];
// Derive z-planes.
double theta = thetaMax;
double dTheta = (pi / 2. - thetaMax) / nZPlanes;
for (int i = 0; i < nZPlanes; i++) {
        zPlanes[i] = calculateR(theta) * cos(theta);
        rInner[i] = calculateR(theta) * sin(theta) - r2;
        rOuter[i] = rInner[i] + thickness;
        theta += dTheta;
}
// Create solid.
new G4Polycone("winstonCone", 0, 2. * pi, nZPlanes,
        zPlanes, rInner, rOuter);
```

Listing B.1: Geant4 Code sample for the creation of a Winston cone using a G4Polycone. The choice of the z-planes is arbitrary and the r can be obtained by deriving the cartesian coordinates of the shape.

```
// With logical volume:
G4LogicalVolume* lv;
// Create optical surface.
G4OpticalSurface* opticalSurface = new G4OpticalSurface(name);
opticalSurface->SetType(dielectric_metal);
opticalSurface->SetFinish(polished);
opticalSurface->SetModel(glisur);
opticalSurface->SetMaterialPropertiesTable(
        lv->GetMaterial()->GetMaterialPropertiesTable());
new G4LogicalSkinSurface(name + "Skin", lv, opticalSurface);
```

Listing B.2: Geant4 Code sample for the creation of a polished surface

Erklärung

Hiermit versichere ich, dass ich diese Arbeit einschließlich beigefügter Zeichnungen, Darstellungen und Tabellen selbstständig angefertigt und keine anderen als die angegebenen Hilfsmittel und Quellen verwendet habe. Alle Stellen, die dem Wortlaut oder dem Sinn nach anderen Werken entnommen sind, habe ich in jedem einzelnen Fall unter genauer Angabe der Quelle deutlich als Entlehnung kenntlich gemacht.

Aachen, der 11. Januar 2012

Tim Niggemann